



저작자표시-비영리-변경금지 2.0 대한민국

이용자는 아래의 조건을 따르는 경우에 한하여 자유롭게

- 이 저작물을 복제, 배포, 전송, 전시, 공연 및 방송할 수 있습니다.

다음과 같은 조건을 따라야 합니다:



저작자표시. 귀하는 원저작자를 표시하여야 합니다.



비영리. 귀하는 이 저작물을 영리 목적으로 이용할 수 없습니다.



변경금지. 귀하는 이 저작물을 개작, 변형 또는 가공할 수 없습니다.

- 귀하는, 이 저작물의 재이용이나 배포의 경우, 이 저작물에 적용된 이용허락조건을 명확하게 나타내어야 합니다.
- 저작권자로부터 별도의 허가를 받으면 이러한 조건들은 적용되지 않습니다.

저작권법에 따른 이용자의 권리는 위의 내용에 의하여 영향을 받지 않습니다.

이것은 [이용허락규약\(Legal Code\)](#)을 이해하기 쉽게 요약한 것입니다.

[Disclaimer](#)

Thesis for a Ph. D. Degree

**Assessing the Impact of Vertical Land
Motion at Tide Gauges of Abnormal Sea
Level Records Using Time-series InSAR
Technique**

시계열 InSAR 기법을 사용하여 비정상적 해수면
상승 기록을 보인 조위관측소의 수직지반변위 평가

August 2021

Graduate School of

Earth and Environmental Sciences

Seoul National University

Suresh Krishnan Palanisamy Vadivel

**Assessing the Impact of Vertical Land Motion at
Tide Gauges of Abnormal Sea Level Records Using
Time-series InSAR Technique**

시계열 InSAR 기법을 사용하여 비정상적인 해수면 상승 기록을
보인 조위관측소의 수직지반변위 평가

지도 교수 김 덕 진

이 논문을 이학박사 학위논문으로 제출함

2021 년 8 월

서울대학교 대학원

자연과학대학 지구환경과학부

Suresh Krishnan Palanisamy Vadivel

Suresh Krishnan Palanisamy Vadivel 의 이학박사 학위논문을
인준함

2021 년 8 월

위 원 장 _____ 조 양 기 _____

부위원장 _____ 김 덕 진 _____

위 원 _____ 이 준 기 _____

위 원 _____ 박 상 은 _____

위 원 _____ 정 정 교 _____

ABSTRACT

Suresh Krishnan Palanisamy Vadivel

자연과학대학 지구환경과학부

Graduate School of Earth and Environmental Sciences

Seoul National University

Global sea level rise has been a serious threat to the low-lying coasts and islands around the world. It is important to understand the global and regional sea level changes for preventing the coastal zones. Tide gauges are installed around the world, which directly measures the change in sea level relative to the local datum. Sea level in the past three decades has risen to 1.8 mm/year compared to the sea level rise in the 20th century (3.35 mm/year), estimated by the Intergovernmental Panel on Climate Change (IPCC). However, along with the contributors of sea level rise, vertical land motion (VLM) is indeed an essential component for understanding the regional sea level change; however, its contribution remains still unclear. The VLM is referred to as change in elevation of land at tide gauge due to the regional and local processes by both natural and anthropogenic activities can deteriorate the sea level records and lead to spurious sea level acceleration. Assessing the vertical land motion at tide gauges with the accuracy of sub-millimeters is essential to reconstruct the global and regional sea level rise. Previous studies attempt to observe the vertical land movements at sparse locations through Global Positioning System (GPS). However, the VLM observed from the sparse GPS network makes the estimation uncertain. In this study, an alternative approach is proposed in this study to directly measure the relative vertical land motion including spatial and temporal variations through Synthetic Aperture Radar (SAR) data by using

time-series SAR interferometric (InSAR) techniques. This work presents a contribution enhancing the estimation of VLM rates with high spatial resolution over large area using time-series InSAR analysis.

First, the C-band Interferometric Wide-swath (IW) mode SAR data from the Sentinel-1 A/B satellite was used in this study to estimate the VLM rates of tide gauges. The Sentinel-1 A/B SAR data were obtained during the period between 2014/10 and 2020/12 (~ 6 years). Stanford Method for Persistent Scatterers – Persistent Scatterer Interferometry (StaMPS-PSI) time-series InSAR algorithm was initially applied to the case study: Pohang tide gauge in the Korean peninsula for monitoring the stability of tide gauge station and its VLM rates during 2014 ~ 2017. For the Pohang tide gauge site, SAR data acquired in both ascending and descending passes and derived the ground movement rates at tide gauge along the line-of-sight direction. The vertical movements from the collocated POHA GPS station were compared with the InSAR derived VLM rates for determining the correlation between the two methods. The VLM rates at the Pohang tide gauge site were -25.5 mm/year during 2014 ~ 2017. This VLM rate at Pohang tide gauge derived by StaMPS-PSI estimates were from the strong dominant scatterers along the coastal regions.

Second, for the terrains, with few dominant scatterers and more distributed scatters, a short temporal InSAR pair selection approach was introduced, referred as Sequential StaMPS-Small baselines subset (StaMPS-SBAS) was proposed in this study. Sequential StaMPS-SBAS forms the interferograms of short temporal sequential order ($n = 5$) to increase the initial pixel candidates on the natural terrains in the vicinity of tide gauges. Sentinel-1 A/B SAR data over ten tide gauges in the Korean peninsula having different

terrain conditions were acquired during 2014 ~ 2020; and employed with sequential StaMPS-SBAS to estimate the VLM rates and time-series displacements. The initial pixel density has been doubled and ~ 1.25 times the final coherent pixels identified over the conventional StaMPS-SBAS analysis.

Third, the potential for the fully automatic estimation of time-series VLM rates by sequential StaMPS-SBAS analysis was investigated. A fully automatic processing module referred to as ‘Seq-TInSAR’, was developed which has three modules 1) automatically downloads Sentinel-1 Single look complex (SLC) data, precise orbit files, and Digital Elevation Model (DEM); 2) SLC pre-processor: extract bursts, fine Coregistration and stacking and, 3) Sequential StaMPS-SBAS processor: estimates the VLM rates and VLM time-series.

Finally, the Seq-TInSAR module is applied to the 100 tide gauges that exhibit abnormal sea level trend with par global mean sea level average. For each tide gauge site, 60 ~ 70 Sentinel-1 A/B SLC scenes were acquired and 300 ~ 350 sequential interferograms were processed to estimate the VLM at tide gauge stations. The final quantitative VLM rates and time-series VLM are estimated for the selected tide gauges stations. Based on the VLM rates, the tide gauges investigated in this study are categorized into different VLM ranges. The in-situ GPS observations available at 12 tide gauge stations were compared with InSAR VLM rates and found strong agreement, which suggests the proposed approach more reliable in measuring the spatial and temporal variations of VLM at tide gauges.

Keyword: Sea level rise, Tide gauge, Relative sea level, Vertical land motion, GPS,
Synthetic Aperture Radar, SAR Interferometry, Time-series InSAR, StaMPS

Student Number: 2016-30749

List of contents

Chapter 1. Introduction.....	1
1.1. Brief overview of sea-level rise.....	1
1.2. Motivations	4
1.3. Purpose of Research.....	9
1.4. Outline.....	12
Chapter 2. Sea Level variations and Estimation of Vertical land motion.....	14
2.1. Sea level variations.....	14
2.2. Sea level observations	14
2.3. Long term sea level estimation.....	19
2.4. Factors contributing tide gauge records: Vertical Land Motion.....	19
2.5. Brief overview of InSAR and Time-series SAR Interferometry	24
Chapter 3. Vertical Land Motion estimation at Tide gauge using Time-series PS-InSAR technique: A case study for Pohang tide gauge	36
3.1. Background	36
3.2. VLM estimation at Pohang tide gauge using StaMPS-PSI analysis.....	38
3.3. Development of StaMPS-SBAS InSAR using Sequential InSAR pair selection suitable for coastal environments.....	55
3.4. Discussion.....	80

Chapter 4. Application of time-series Sequential-SBAS InSAR for Vertical Land Motion estimation at selected tide gauges around the world using Sentinel-1 SAR data.....	85
4.1. Description of PSMSL tide gauge data.....	87
4.2. Sentinel-1 A/B SAR data acquisitions	92
4.3. Automatic Time-series InSAR processing module "Seq-TInSAR"	93
4.4. Results: Estimation of vertical land motions at selected tide gauges	97
4.5. Comparison of InSAR results with GNSS observations.....	112
4.6. Discussion.....	125
Chapter 5. Conclusions and Future Perspectives.....	128
Abstract in Korean.....	133
Appendix – A	136
Appendix – B	146
Bibliography.....	152

List of Figures

Figure 2.1.	Schematic diagram showing tide gauge measurement system	16
Figure 2.2.	Tide gauge stations under PSMSL network located around the world.....	17
Figure 2.3	SAR Interferometry geometry	25
Figure 2.4	Processing flow to create ground displacement maps using SAR data.....	28
Figure 2.5.	StaMPS time-series PS-InSAR processing flow.....	35
Figure 3.1	Study Area map of Pohang tide gauges station located in the Korean Peninsula.....	39
Figure 3.2.	Acquisition modes of Sentinel-1 A/B (Source: European Space Agency).....	40
Figure 3.3.	Sentinel-1 A/B acquisition time with perpendicular baseline for (a) ascending (reference: 2017/02/19) and (b) descending (reference: 2017/04/14) passes.....	42
Figure 3.4.	Line of sight velocities from the time-series interferometry results obtained from (a) Ascending track (2014/11 – 2017/12) and (b) descending track (2015/05 – 2018/05). The Negative values indicate displacement away from the	

satellite (c) Time-series InSAR displacement at Pohang tidal gauge station for ascending (blue) and descending track (green).....	46
Figure 3.5. Projection of InSAR LOS velocity decomposition into 2D velocity components along the vertical and horizontal directions.....	48
Figure 3.6. InSAR derived ground motion velocity over the period (2015/-5 – 2017/12) (a) Vertical ground motion component (b) Horizontal ground motion component.....	50
Figure 3.7. Global positioning system (GPS) displacements measured at the POHA station from 2013 to 2016 (KHOA). (a) North-South, (b) East-West, and (c) vertical displacements. Horizontal components are measured in degrees and vertical displacement is measured in meters.....	51
Figure 3.8. Temporal profiles of (a) Absolute vertical ground motion by GPS (b) Relative vertical ground motion from InSAR displacements (c) Sea level records observed at Pohang tidal gauge station since 2013.....	52
Figure 3.9. Sequential InSAR pair selection for StaMPS time-series InSAR analysis.....	57
Figure 3.10 (a) and (b) plot between Perpendicular baselines and Temporal baselines for standard StaMPS-SBAS and Sequential pair selection, respectively. (c) and (d) $D_{\Delta,A}$ estimated for standard StaMPS-SB and sequential pair selection, respectively, (e) and (f) the initial PS candidates selected based on the threshold value $D_{\Delta,A} <$	

0.6. (g) and (h) histograms of $D_{\Delta A}$ for sequential and standard SBAS pair selection.....	63
Figure 3.11. Spatial distribution of SDFP pixels obtained from SBAS pair selection and sequential pairs selection.....	64
Figure 3.12. Comparison of mean LOS velocity map (descending) between (a) StaMPS-SBAS and (b) Sequential pair selection, respectively. Time-series displacements between two approaches (c) at pixel A and (d) at pixel B.....	65
Figure 3.13 Sentinel-1 Synthetic Aperture Radar (SAR) image acquired over the tide gauges located in the Korean Peninsula.....	68
Figure 3.14. Tide gauge stations used in this interferometric analysis.....	69
Figure 3.15. Pohang tide gauge station: (a-h) Mean InSAR velocity maps and (i) time-series displacements (grey triangle denotes ascending and grey circle denotes descending track).....	73
Figure 3.16. KHOA's sea-level changes observed from Pohang tide gauge for the period (a) 1989 – 2018, (b) 1999 – 2018, and (c) 2009 – 2018. (d) Vertical displacement observed at Pohang GNSS station co-located with Pohang tide gauge. (e) Leveling data obtained at TBM No. 5.....	75
Figure 3.17. Yeosu tide gauge station: (a–d) Mean InSAR velocity maps for ascending, descending, vertical, and horizontal geometry, respectively. (e–h) time-series InSAR displacements for ascending, descending, vertical, and horizontal geometry, respectively.....	76

Figure 3.18. Incheon tide gauge station: (a–d) Mean InSAR velocity maps for ascending, descending, vertical, and horizontal geometry, respectively. (e–h) time-series InSAR displacements for ascending, descending, vertical, and horizontal geometry, respectively.....	77
Figure 3.19. (a,b) Mean InSAR velocity maps at Jeju along descending and vertical geometry, respectively, and (c,d) time-series InSAR displacements along descending and vertical geometry, respectively.....	78
Figure 3.20. (a,b) Mean InSAR velocity maps at Seogwipo along descending and vertical geometry, respectively, and (c,d) time-series InSAR displacements along descending and vertical geometry, respectively.....	79
Figure 3.21. Comparison of mean LOS velocity maps between the StaMPS-SBAS and sequential-SBAS.....	82
Figure 4.1. Distribution of tide gauge stations (Source: SONEL).....	88
Figure 4.2. 100 tide gauge stations selected for estimating VLM in this study.....	90
Figure 4.3. Selected tide gauges stations categorized into five regions.....	91
Figure 4.4. Seq-TInSAR architecture downloading Sentinel-1 data and their timer-series interferometric processing.....	94
Figure 4.5. The workflow of the proposed Seq-TInSAR module used in this study.....	97
Figure 4.6. Mean VLM rate at tide gauges in the North America region.....	99

Figure 4.7.	Mean VLM rate (mm/year) for tide gauges in the Europe region.....	103
Figure 4.8.	Mean VLM rate (mm/year) at tide gauges in the Korea region.....	105
Figure 4.9.	Mean VLM rate (mm/year) at tide gauges in the Japan region.....	106
Figure 4.10.	Mean VLM rate (mm/year) at tide gauges in the South Asia region...	110
Figure 4.11.	Mean VLM rate (mm/year) at tide gauges in the Australia & New Zealand region.....	112
Figure 4.12.	Comparison of InSAR VLM trend and GPS derived VLM trend.....	113
Figure 4.13.	Vertical Land Motion velocities at tide gauges around the world estimated from Seq-TInSAR.....	118
Figure 4.14.	Vertical Land Motion velocities at tide gauges in North America region estimated from Seq-TInSAR.....	119
Figure 4.15.	Vertical Land Motion velocities at tide gauges in the Europe region estimated from Seq-TInSAR.....	119
Figure 4.16.	Vertical Land Motion velocities at tide gauges in East Asia region estimated from Seq-TInSAR.....	120
Figure 4.17.	Vertical Land Motion velocities at tide gauges in South Asia region estimated from Seq-TInSAR.....	120
Figure 4.18.	Vertical Land Motion velocities at tide gauges in the Australia & New Zealand region estimated from Seq-TInSAR.....	121

Figure 4.19. (a) Mean LOS velocity from Seq-TInSAR over the Legaspi, Albay bay; Relationship between the relative sea level trend and InSAR derived VLM.....	123
Figure 4.20 (a) Mean LOS velocity from Seq-TInSAR over the Singapore coast; Relationship between the relative sea level and InSAR derived VLM (b) West tuas tide gauge (c) Bukom island tide gauge.....	124
Figure 4.21. Schematic representation of Seq-TInSAR VLM product generation.....	127

List of Tables

Table 2.1.	Total sea level estimates observed from tide gauges and satellite altimetry.....	19
Table 2.2.	Literature review on the estimation of individual components influencing the sea level change.....	20
Table 3.1.	Detailed description of Sentinel-1 A/B SAR scenes used in this Chapter 3.2 for StaMPS-PSI analysis.....	42
Table 3.2.	Comparison of SDFP pixels statistics between StaMPS-SBAS and sequential pair selection approach.....	62
Table 3.3.	Tide gauge stations used in the interferometric analysis.....	66
Table 3.4.	Processing workflow of StaMPS-SBAS for vertical land motion at each tide gauge.....	70
Table 4.2.	Input arguments for Seq-InSAR and their usage.....	95
Table 4.3	Categorization of tide gauges based on the rate of VLM at tide gauges.....	122

Chapter 1.

Introduction

1.1.Brief overview of sea-level rise

Global sea level rise has been a serious threat to the low-lying coastal region around the world and the global sea level has increased over the 21st century than the last century (Nicholls and Cazenave 2010). Global mean sea level (GMSL) reconstructed using tide gauge records from 1993 to 2018 has been rising about 3.35 mm/year which was estimated as 1.5 mm/year over the 20th century (1900 ~ 2018) (Frederikse et al. 2020). The rate for the past two decades was nearly twice the average of the 20th century (Nerem et al. 2018).

The global sea levels are rising as a direct result of a changing climate such as global warming. The long-term changes in the global mean sea level were primarily driven by three ocean processes: Ice melts, Thermal expansion, and Land water storage (Frederikse et al. 2020, Church et al. 2013). A large portion of the Earth's freshwater is frozen and stored in glaciers, due to global warming; the ice sheets melt and increase the flow of freshwater into oceans and sea levels rise (Church and White 2011). As the additional heat generated by global warming is absorbed by the ocean and when the water warms, the expansion of water molecules increases the volume of the ocean (Widlansky, Long, and Schloesser 2020). When the water is impounded on land or removed from the land by groundwater pumping can cause a change in land water storage, which led to a change in the total volume of the ocean (Ngo-Duc et al. 2005, Milly et al. 2010). In addition to

these contributions, other regional factors such as ocean and atmospheric circulation along with the coast cause rising sea levels (Hamlington et al. 2020).

Global mean sea level estimate is an averaged trend that is reconstructed using the regional sea level change records measured by tide gauges and satellite altimetry (Frederikse et al. 2020). Since the early 1990s, the satellite record has provided a relatively direct measurement of global sea level (Nerem et al. 2018). However, the satellite altimetry records are short, compared with the sea level measurements by tide gauge. Since the early 20th century, tide gauge records provide sea level changes relative to the land surface along the coasts.

Sea level changes are not uniform around the world, the oceanic circulation and ice melting contribute regionally varying sea levels (Pörtner et al. 2019). The changes in the regional relative sea level measured by tide gauges are the cumulative result of many individual geodetic processes that vary both in space and in time such as land subsidence caused by human activities in the coastal areas including groundwater extraction (Pörtner et al. 2019). Therefore, the relative sea level records from tide gauges represent the combination of the change in land surface elevation (land motion) and the regional sea level change. The coastal subsidence referred to the sinking of land surface and uplifting of the land surface normally occurs at rates of mm/year. Even though this VLM rate appears small, it can affect the relative sea level change at a substantial amount. The impact of VLM on tide gauges has different impacts from place to place based on the natural and anthropogenic processes on the coastal areas. The VLM phenomenon on the coasts can be both steady that are ongoing for long-term and transient that occurred in the

last few years. It is essential to understand the spatial and temporal characteristics of VLM at tide gauge station.

VLM patterns that persist over the large spatial scales are influenced by the response of the Earth's crust displacement from the mass redistribution due to changes in the ice mass and total water storage (TWS) (Peltier 2004, Hamlington et al. 2020). Glacial isostatic adjustment (GIA) is the process of Earth's response to the retreat of mass ice sheets exhibiting changes to relative sea level (Peltier 2004). In addition, the other type of VLM that occurs rapidly and locally are mainly driven by tectonics and groundwater withdrawal (Frederikse et al. 2020). The tectonic plates that collide and accumulating the energy resulting earthquakes and volcanoes can cause rapid VLM. In addition, groundwater withdrawal on the delta and coasts will cause the compaction of sub-surface aquifers that leads to ground motion.

For the understanding of VLM and its influence on the coastal sea level change records, traditionally, the repeated measurements at different times and measure the change in land elevation between the tide gauge and known land surface (benchmark). Alternatively, Global Positioning System (GPS) satellites allow us to measure the position of tide gauge on the Earth's surface within the millimeter level accuracy. A considerable network of permanent GNSS stations have been being operated worldwide to continuously measure the vertical land motion. Among those stations, some of them are installed along with tide gauges (co-located) to provide a more accurate VLM measurement observed in tide gauge stations. Currently, the larger ground movement components such as GIA can be calculated from the VLM in the network of GNSS stations, since the GIA has a relatively slow and steady nature. The validity of their

measurements is limited in space, and therefore the extrapolation of GNSS measurements to the VLM at tide gauge stations becomes unreasonable due to the very local characteristics of land motions (Raucoules et al. 2013).

While this is still a prominent technique, in recent decades, space-borne sensor capabilities have been revolutionized in understanding the Earth's surface movements. Interferometric synthetic aperture radar (InSAR) is a widely accepted observation technique to fill this information gap. Synthetic Aperture Radar (SAR) provides all-weather, high-resolution images of the Earth's surface. By combining two or more SAR images of the same area at different periods, it is possible to generate land surface change maps with unprecedented resolution and precision. With the advent of space-borne radars, SAR interferometry has been applied to the study of both natural and anthropogenic processes such as earthquakes, volcanoes, ground subsidence, and landslides. SAR interferometric technique utilizes the phase differences between two or more signals of the same location received SAR sensor at different periods, using that the VLM between two SAR scenes can be calculated. In addition, after the launch of several space-borne SAR satellites, the SAR image records have been increased enormously, and thus, InSAR has the capability to have wide coverage on land and map the millimeter scale of VLM changes through the time.

1.2.Motivations

Several researches have reported that the land surface motions have been observed in the coastal environment around the world. Since the tide gauge records the sea level change relative to the solid earth, the tide gauge measurements can be considered either a relative sea level change or vertical land motions. For tide gauges dominated by VLM,

the tide gauge measurements show a rising trend when the land is moving down, whereas the tide gauge measurements show decreasing trend when the land moves upward. It is crucial to estimate the precise VLM at tide gauges to derive a more reliable estimate of relative sea level changes.

Existing geophysical models only provide the vertical land motion at a global scale (Peltier and Tushingham 1991, Peltier 2004). These models can only predict the vertical land motion due to the postglacial rebound of the solid earth surface at the global scale. An alternative approach was developed later by installing the continuous Global Positioning Systems (GPS) at the tidal gauge site to measure reliable absolute ground motion in the geocentric reference frame (Meyssignac et al., 2011; Wöppelmann, Martin Miguez, Bouin, & Altamimi, 2007). Although this approach is widely accepted, very few tidal gauges are deployed with permanent GPS stations. In the past decades, the in-situ GNSS observations are widely applied technique for the estimation of VLM caused by other processes associated with plate tectonics, sediment compaction, or with anthropogenic causes such as the settlement of reclaimed land, groundwater extraction in coastal cities (Wöppelmann et al. 2007, Bouin and Wöppelmann 2010, Santamaría-Gómez et al. 2012, Wöppelmann and Marcos 2016). The VLM from in-situ measurements have relatively short spatial and temporal scales, and oftentimes, the GNSS observations are away from the tide gauges. Since the GNSS stations are still limited by the number of receiving stations and a small number of GNSS stations are paired with tide gauges. The co-located GNSS stations and tide gauges are critical and without them, it would be quite difficult to apply the VLM correction at tide gauges in general and consequently, those VLM affected tide gauges were discarded from the study

(Church et al. 2013, Douglas 1997). Other research proposed the geodetic methods to combine satellite altimetry and tide gauge data for VLM estimation (Cazenave et al. 1999, Kuo et al. 2004). Despite the implementation of this strategy, the accuracy is usually excess of 1 mm/year (Wöppelmann and Marcos 2012, Ray and Douglas 2011, Santamaría-Gómez, Gravelle, and Wöppelmann 2014, Kuo et al. 2004, Kuo et al. 2008). Despite that, the determination of reliable vertical land motion using several geodetic methods remains a challenging issue. With the knowledge of the recent researches in the monitoring of the stability of tide gauges using above mentioned geodetic methods, the importance of VLM in the tide gauge measurements were shown and the limitations of currently available methods for measuring the spatial and temporal variations of VLM were highlighted. (Wöppelmann and Marcos 2016).

Recent approaches have been presented to estimate the vertical land motion using short-term satellite altimetry data and long-term sea level change patterns recorded by tidal gauges (Kuo et al., 2004; Wöppelmann & Marcos, 2012). Consequently, the discussion on employing space-borne SAR interferometric techniques has gained much importance in recent years to estimate the vertical ground motion (Wöppelmann & Marcos, 2016). The vertical ground motion estimates obtained by various approaches have been reported for various sites Alexandria, Egypt (Wöppelmann et al., 2013) and Manilla, Philippines (Raucoules et al., 2013). However, no effort has been made to estimate vertical ground motions at tidal gauge station by above said approaches.

SAR Interferometric (InSAR) techniques are widely accepted to estimate the earth's surface displacements (Massonnet et al., 1993). Spaceborne remote sensing techniques such as Interferometric Synthetic Aperture Radar (InSAR) have revolutionized geodesy

by making it possible to detect the relative land elevation changes including subsidence and uplift on a regional scale (Bamler and Hartl 1998, Bürgmann, Rosen, and Fielding 2000, Hooper et al. 2004). While GNSS observations provide geocentric VLM at sparse locations, InSAR can make precise relative land changes consistently over the larger areas with hundreds of thousands of VLM data points (Blackwell et al. 2020).

In recent years, the time-series InSAR analysis estimates the relative displacements at millimeter level accuracies such as Persistent Scatter Interferometry (PSI) (Ferretti, Prati, & Rocca, 2001; Hooper, Zebker, Segall, & Kampes, 2004) and Small Baseline Subset (SBAS) (Berardino, Fornaro, Lanari, & Sansosti, 2002). With the development of time-series InSAR techniques, the application of InSAR techniques for geodetic information has stepped into a new era (Ferretti, Prati, and Rocca 2001, Berardino et al. 2002, Hooper et al. 2004, Hooper, Segall, and Zebker 2007, Hooper 2008). The capability of repeat-pass SAR interferometry for ground deformation mapping has accelerated after the launch of ERS-1 in 1991, since then a huge amount of SAR data available for repeat-pass SAR interferometry. The ability of the Differential-InSAR (D-InSAR) technique was demonstrated by detecting the displacement field of the 1992 Landers earthquake (Massonnet et al. 1993). It has also been proved that InSAR can detect the deformation with sub-centimeter accuracy. Since then, InSAR is widely utilized in measuring the Earth's surface elevation changes due to natural disasters and human activities such as earthquakes (Massonnet et al. 1993, Massonnet and Feigl 1998, Yen et al. 2006, Wright, Parsons, and Lu 2004), volcanic eruptions (Amelung et al. 2000, Massonnet, Briole, and Arnaud 1995) and land subsidence/uplift (Fielding, Blom, and Goldstein 1998, Amelung et al. 1999, Galloway et al. 1998).

However, the repeat-pass D-InSAR technique is limited by different decorrelation sources including atmospheric heterogeneities, thermal noise of SAR systems (Zebker and Villasenor 1992). To maximize the potential of D-InSAR, time-series algorithms were developed, for instance, persistent scatterers InSAR (Ferretti, Prati, and Rocca 2001, Hooper, Segall, and Zebker 2007), Small Baseline subset InSAR (Berardino et al. 2002, Hooper 2008), and SqueeSAR (Ferretti et al. 2011) to minimize the interferometric decorrelation and atmospheric noise of conventional InSAR. However, until now the implementations of these multi-temporal InSAR techniques are limited to applications that are comprised of bright scatterers, for instance, man-made structures.

Stanford Method for Persistent scatterers (StaMPS) is a persistent scatter analysis method that identifies and extracts the deformation signal even in the lack of bright scatterers (Hooper et al. 2004, Hooper, Segall, and Zebker 2007). StaMPS multi-temporal InSAR technique comprised of PS-InSAR and SBAS methods (Hooper, Segall, and Zebker 2007, Hooper 2008). StaMPS PS-InSAR relies on the analysis of interferograms with reference to one reference image, which identifies permanent scatterers to address the decorrelation problem (Hooper, Segall, and Zebker 2007). StaMPS SBAS algorithms use possible interferograms with a small spatial baseline and temporal baseline to minimize the spatial and temporal decorrelation (Hooper 2008). StaMPS PS and SBAS techniques has showed its ability to measure the temporal displacements at coherent scatterers in the urban areas with high spatial resolution. However, it is still a challenge for StaMPS to identify sufficient coherent pixel density in the natural environments such as coastal regions. Despite the merits of StaMPS PS and SBAS methods, it is crucial to efficiently improve these algorithms on coastal regions having sparse coherent scatterers. Also,

recently several SAR satellite missions are orbiting to provide SAR data frequently than previous missions and freely available for science applications. European Space Agency's Sentinel-1 mission has been imaging Earth's surface every 12 days or less. Together, these spaceborne observations enable unprecedented VLM monitoring capabilities for sea level change related studies. Unlike GPS station, that measures the precise vertical displacements at specific locations in the geocentric frame, time-series InSAR estimates relative displacements with high spatial resolution. The predominance of the line of sight land motion on sea level change in the coastal areas were explored using PS-InSAR technique (Wöppelmann et al., 2013). However, there is still need to estimate the precise vertical and horizontal ground motion at the tidal gauges to apply the correction to the sea level change.

1.3.Purpose of Research

Sea level rise is an important issue over the past century. The long-term sea level changes are recorded by the tide gauges installed on the coasts around the world (Douglas 2001). On one hand, the local ground motion at tide gauges can accelerate/decelerate the sea level signals associated with the climate change (Douglas 2008). On the other hand, the local ground motion in the coastal areas can increase the risk of coastal inundation (Nicholls and Cazenave 2010).

Until the introduction of advanced geodetic methods, there was no attention given to the Vertical land motion. Since, the launch of spaceborne SAR satellite, there were several researches detects the land subsidence / uplift due to natural and

anthropogenic causes (Bamler and Hartl 1998, Bürgmann, Rosen, and Fielding 2000, Hooper et al. 2004, Chaussard et al. 2013).

However, before the launch of SAR satellites there was no knowledge of vertical land motion at tide gauges without in-situ geodetic methods. After the launch of SAR satellites, the ground motion signals at tide gauges and surrounding coastal areas has been detected which was not detected earlier (Raucoules et al. 2013, Palanisamy Vadivel et al. 2019, Poitevin et al. 2019).

Therefore, when the researches detects the abnormal change of sea level trend in the tide gauge records, can now verify the influence of the vertical land motion at tide gauges using the spaceborne InSAR datasets. In addition to the VLM at tide gauges, the coastal subsidence and/or uplift can also be detected at both temporal and spatial scale.

In the previous section, the possible reasons for constraints in the estimation of vertical land motion (VLM) at tide gauges using in-situ observations were highlighted. Despite the fact, that GNSS is useful for estimating VLM at tide gauges, however, the limited number of tide gauges are paired with GNSS stations, makes the corrections of relative sea level changes challenging. To overcome the problem and obtain reliable GMSL estimates depends on how precise the VLM at tide gauge is estimated and the correction method applied to relative sea level change records. It is therefore necessary to extend the knowledge with high spatial resolution on vertical land movements at vulnerable tide gauges along the coasts. The major aspect of this study is measurement and monitoring

of the stability of tide gauges, and the contribution of precise VLM estimates from multi-temporal InSAR data. Time-series interferometric SAR analysis can provide the multi-temporal VLM estimates on the tide gauges at millimeter level accuracy without the in-situ measurement methods. However, the exploitation of time-series InSAR primarily depends on the number of persistent scatterers available in the vicinity of the tide gauges. The StaMPS SBAS algorithm identifies the coherent scatterers based on the amplitude dispersion difference index (ADD) and phase stability analysis. Therefore, the density of persistent scatterers in the study area should be increased to estimate the VLM trend of tide gauges. Then, the estimated VLM at tide gauges will be corrected for relative sea level changes.

This research aims to estimate the rate of vertical land motion by applying the time-series SAR interferometric technique to identify the tide gauge stations that are prone to land surface displacements. Firstly, the StaMPS PS-InSAR technique is applied to estimate the VLM at tide gauge to analyze the feasibility of the time-series technique for VLM estimation, and then compared with collocated GNSS observations. For a case study, the VLM at Pohang tide gauge located in the Korean peninsula which exhibits abnormal relative sea level changes will be estimated. Secondly, the StaMPS SBAS algorithm is improved by utilizing the sequential interferograms pair selection strategy to increase the coherent pixels density near the coastal regions, and then the VLM at the abnormal tide gauges selected around the world will be estimated. Then, the estimated VLM will be used for correcting the relative sea level changes for improved GMSL estimates.

The main research objectives of this dissertation are summarized below:

1. Development of time-series StaMPS SBAS algorithm for high PS density along the coastal areas using Sentinel-1 SAR dataset.
2. Development of a fully automatic and unsupervised processing module ‘Seq-TInSAR’ to generate VLM velocity and time-series VLM products using InSAR Scientific Computing Environment (ISCE) v2.3.3 and StaMPS v4.1b
3. Estimation and monitoring of precise VLM estimates and stability of the abnormal tide gauges exhibiting significant relative sea level changes
4. Evaluation of VLM estimates by proposed method using available GNSS observations.

1.4.Outline

Chapter 2 provides a brief overview of the principle of tide gauges, relative sea level changes, and global mean sea level projections. The factors contributing to the tide gauge records and uncertainties in the GMSL estimates are reviewed. This chapter also reviews the principle of SAR, InSAR, and multi-temporal approaches including PS and SBAS.

Chapter 3 presents the feasibility of the time-series of SAR interferometric approaches for measuring VLM at tide gauges. The StaMPS PS-InSAR technique is evaluated at the Pohang tide gauge station using Sentinel-1 SAR data and validated with collocated GNSS observations and leveling measurements.

In chapter 4, a sequential InSAR pair selection strategy for StaMPS SBAS algorithm is proposed and applied to abnormal tide gauges selected around the world to measure the VLM at mm/year-scale. An automatic processing chain called ‘Seq-TInSAR’ is

introduced to generate VLM velocity maps and time-series VLM trend automatically. A comparative analysis between InSAR VLM and permanent GPS derived VLM is presented.

In chapter 5, the impact of VLM and correction for relative sea level changes are summarized and the future perspectives on this study are discussed.

Chapter 2.

Sea Level variations and Estimation of Vertical land motion

2.1.Sea level variations

Long-term and short-term sea level variations are contributed by various factors. Short-term variations such as waves and tides occur daily. Long-term variations which is extremely important occur on different timescales from monthly to decades, include seasonal cycles, incremental trends, and recurrent anomalies. Ice sheets melting, thermal expansions of water molecules in the ocean are major factors influencing the long-term sea level variations.

2.2.Sea level observations

2.2.1. Principle of tide gauges

Tide gauge is one of the modern sea level monitoring stations that fitted with sensors to measure the rise and fall of the water level (Douglas 2001). The observations from the tide gauge are heights of sea level expressed with reference to a local datum. Therefore, the term ‘relative sea level (RSL)’ is used to refer the sea level relative to the land upon which the tide gauge is grounded (Douglas 2001).

Tide gauge measures the change in sea level along the continental coastlines and islands. The schematic representation of a typical tide gauge station is illustrated in Figure 2.1. These systematic measurements of sea level from direct measurements date back to the late 17th century and continue to provide the relative sea level changes around the world. Until mid-19th century, mechanical tide gauges were used, and then automatic tide

gauges were developed. The tide gauges are installed around the world; however, most of the tide gauges are installed in the northern hemisphere (Gehrels and Woodworth 2013). The observations of tide gauge stations span multi-decadal at several stations and continued to install new stations around the world.

The Permanent Service for Mean Sea Level (PSMSL) is the internationally recognized global sea level data bank for long-term sea level change information from tide gauges. The objective of the PSMSL is the distribution of the global databank for long-term sea level information from tide gauges. The PSMSL database contains monthly and annual mean values of sea level. The dataset and ancillary information are provided free of charge and are made available to the international scientific community through the PSMSL website (www.psmsl.org). For time-series analysis of sea level, a local datum of the tide gauge is maintained by periodical calibration and precise in-situ leveling, known as revised local reference (RLR). The major limitations of the tide gauges as listed by (Cipollini et al. 2017) are as follows: 1) It has the heterogeneous distribution of tide gauges and most of them are located in the Northern hemisphere, 2) there is no common reference frame to the tide gauge records, 3) since, the tide gauges are attached to the land surface, might undergo vertical land motion, which makes tide gauges difficult to interpret. Despite its limitations, due to the high temporal resolution of tide gauge measurements, these are vital for global sea level changes, and other applications such as observing storm waves and tsunamis.

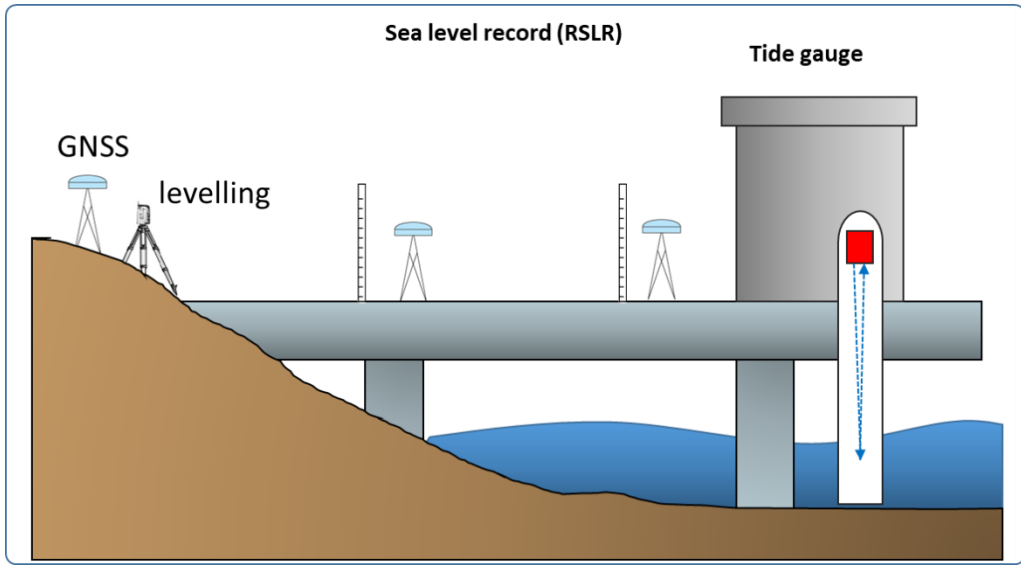


Figure 2.1. Schematic diagram showing tide gauge measurement system

Tide gauges distributed around the world

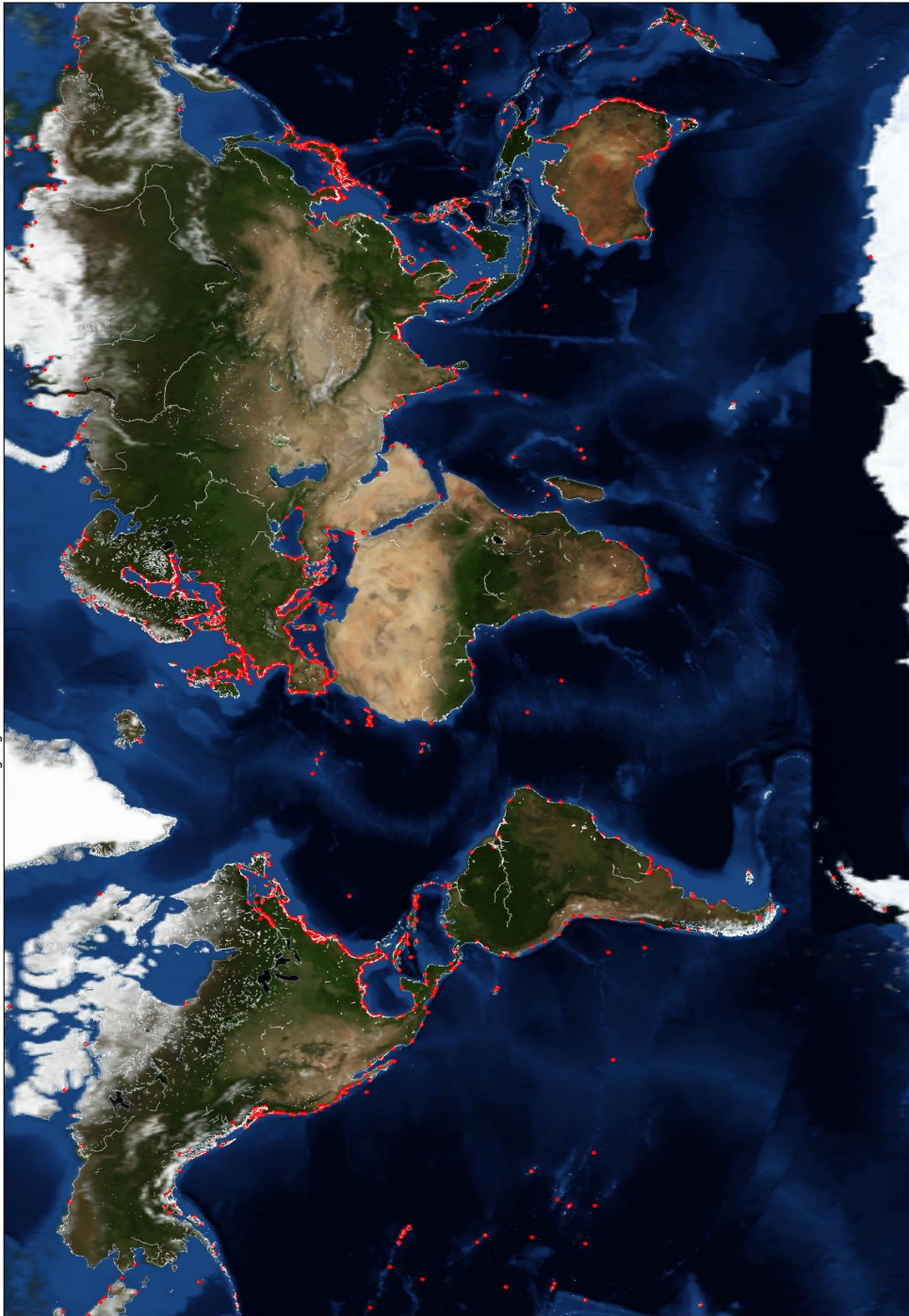


Figure 2.2. Tide gauge stations under PSMSL network located around the world

2.2.2 Satellite altimetry

Satellite altimetry on the other hand estimates the vertical range from the satellite to the Earth's surface by measuring the time taken by a short pulse of microwave radiation to travel from the satellite to the Earth's surface and back to the satellite (Santamaría-Gómez, 2010). Since the early 1990s, the constellation of altimetry, satellite measurements provides the global measurement of sea surface height (SSH) (Ablain et al. 2009). In contrast to tide gauges that measure the sea level changes reference to a local datum, the satellite altimetry measures the SSH above the geocentric reference system. The main advantage of satellite altimetry is its quasi-global coverage and homogenous temporal coverage (Cazenave, Palanisamy, and Ablain 2018). Since 1993, the global mean sea level (GMSL) rise is estimated as 3.34 ± 0.4 mm/year using the satellite altimeter data from TOPEX/Poseidon, Jason 1, Jason 2, Jason 3 (Beckley et al. 2017).

In order to derive the sea surface height, the precise satellite orbit relative to the geocentric reference frame has to be determined, and then the difference between the satellite altitude and measured range gives sea surface height. The major limitations of the satellite altimetry as listed by Adebisi et al. (2021) are as follows: 1) It has the restricted use close to the coastlines, as the satellite altimetry is originally aimed to open oceans. 2) Within the range of 10-15 km from the coast, the radar echoes returned to the satellite have distorted due to the contamination from the nearby land, 3) Precise corrections are required for range, atmospheric pressure, geoidal heights, and ocean tides.

2.3. Long term sea level estimation

Both tide gauges and altimetry are complementary techniques in spatial and temporal characteristics. The global sea level change observed from tide gauge and satellite altimetry is listed in Table 2.1 (Hamlington et al. 2020)

Table 2.1 Total sea level estimates observed from tide gauges and satellite altimetry

Period	Estimate (mm/year)	Uncertainty (\pm mm/year)	Reference	Measurement technique
1900 – 2018	1.56	0.3	(Frederikse et al. 2020)	Tide gauges
1993 – 2018	3.35	0.47	(Frederikse et al. 2020)	Tide gauges
1993 – 2020	3.34	0.4	(Beckley et al. 2017)	Satellite Altimetry

2.4. Factors contributing tide gauge records: Vertical Land Motion

The sea level variations measured by tide gauges are influenced by several factors such as melting ice sheets, glaciers melting, steric sea-level change, land water storage, and vertical land motion. The individual components of sea level estimates are dominated by different temporal scales and different magnitudes. The components of the relative sea

level changes and their estimates presented by Hamlington et al. (2020) are listed in Table 2.2.

Table 2.2 Literature review on the estimation of individual components influencing the sea level change

Component	Period	Estimate (mm/year)	Uncertainty (\pm mm/year)	Reference	Measurement technique
Steric sea level	1900 – 2018	0.52	0.18	(Frederikse et al. 2020)	In-situ observations
Steric sea level	2005 – 2019	1.10	0.20	(Roemmich and Gilson 2009)	Argo Floats
Ocean Mass	1900 – 2018	1.00	0.3	(Frederikse et al. 2020)	Synthesis of satellite and in-situ
Ocean Mass	2002 – 2020	2.10	0.3	(Watkins et al. 2015)	GRACE / GRACE-FO
Glacier Mass loss	1900 – 2018	0.7	0.18	(Frederikse et al. 2020)	Synthesis of satellite and in-situ

Glacier Mass loss	2002 – 2016	0.57	0.1	(Wouters, Gardner, and Moholdt 2019)	GRACE
Land water storage	1900 – 2018	-0.21	0.13	(Frederikse et al. 2020)	Synthesis of satellite and in-situ
Land water storage	2002 – 2014	-0.33	0.16	(Reager et al. 2016)	GRACE

In order to understand the rise of sea level and its sources, it is essential to reduce the difference in the estimates of individual components. In Table 2.2, the vertical land motion component that is not related to GIA is not discussed. Over the years, the understanding of GIA-related vertical land motion has been significantly improved with the advent of GRACE satellite system, have provided the observation of VLM related to GIA with an unprecedented precision and accuracy. The major difficulty is to estimate the non GIA-related VLM sources. The relative sea level observations along the coasts has significant local impact by the VLM. Therefore, it is essential to determine the VLM along the coastal locations. The current methods available to measure these VLM and the research gaps are discussed in the following section.

Vertical land movements at tide gauge

As shown in Table 2.1, the sea level estimation from the long-term tide gauge measurements are less than 2 mm/year, however, the sea level trend has risen globally at an average rate of 1.7 ± 0.2 mm/year in the recent years compared to the past century. In order to improve the long-term sea level estimates and understand their coastal impacts, the VLM should be determined with an acceptable uncertainty level. Unlike other components in the sea level budget, VLM at tide gauges cannot be projected using models, therefore, a direct method to measure the precise VLM is essential (Blewitt et al. 2010). For the past two decades, space geodetic methods Global Navigation Satellite System (GNSS) have become noticeable to measure the vertical movements of tide gauges, which measures the VLM more precisely. Several studies use GNSS velocities to correct the tide gauge trends, (Wöppelmann et al. 2007, Wöppelmann and Marcos 2012, Schumacher et al. 2018). An alternative approach was developed later by installing the continuous Global Positioning Systems (GPS) at the tidal gauge site to measure reliable absolute ground motion in the geocentric reference frame (Meyssignac et al., 2011; Wöppelmann, Martin Miguez, Bouin, & Altamimi, 2007). Although this approach is widely accepted, very few tidal gauges are deployed with permanent GPS stations.

One of the key assumption made when relating relative sea level rise to absolute sea level rise is that the VLM is linear over the entire time span of tide gauge records. Although this assumption is true for GIA rates, it might not necessarily be reliable for present-day time-varying processes, such as volcanic, human and tectonic processes, which contribute differently to VLM (Karegar, Dixon, and Malservisi 2015, Karegar et al. 2017). Secondly, the vertical velocity estimated with GPS is representative of the tide

gauge trend (Santamaría-Gómez et al. 2012). However, the first assumption is only valid for determining the GIA-related VLM as it can be considered constant at most sites for the 20th century. In addition, the second assumption relies on the consistency between tide gauges and GPS stations. If the local stability of tide gauges is ensured, then the VLM of GPS stations at distance from tide gauges is a minor issue. However, if the stability of the tide gauge was not ensured then the VLM at tide gauge and GPS velocity at distance would be different. Therefore, it is essential to measure the local stability of tide gauge station to address the VLM at tide gauges.

The next chapter deals with the advent of SAR Interferometric techniques to measure the vertical movements of tide gauges with SAR data.

2.5. Brief overview of InSAR and Time-series SAR Interferometry

Synthetic Aperture Radar (SAR) is a side-looking, pulsed radar system, in which a microwave pulse is transmitted through an antenna to the ground surface to illuminate the target. The backscattered signal is processed to determine the properties of the target. Based on the distance between the radar and the target, the time duration varies for receiving signals. Therefore, by measuring the time duration between the transmission and reception of the pulse t , the distance between the radar and the target is derived as,

$$R_s = \frac{ct}{2} \quad 2.1$$

Where R_s is the slant range distance, c is the speed of the light and t is the time between the transmission and reception of a pulse. The ability to detect targets from SAR images depends on its system resolution such as spatial resolution, wavelength, incidence angle, and polarization.

2.5.1. Synthetic Aperture Radar Interferometry (InSAR)

SAR image represents a precise observation of radar echo comprised of amplitude and phase. The transmitted pulse from radar reaches the target on the ground and received back to the radar to form SAR images. The scatterer at different distances from the radar introduces different delays between transmission and reception of the transmitted signal. This phase delay is equivalent to a phase change between transmitted and received signals, due to the sinusoidal nature of the transmitted signal. SAR interferometry is a technique to image the surface topography and ground displacements, using phase values

of two or more SAR images. Two complex SAR images taken over the same region, either by two antennas on the same satellite or taken during repeated overpasses are cross-multiplied to form an interferogram. The interferometric phase ϕ_{int} is given as

$$\phi_{int} = \frac{4\pi\Delta R}{\lambda}, \Delta R = R_1 - R_2 \quad 2.2$$

Where, R_1 is the line of sight distance during the first pass, R_2 is the line of sight distance during the second pass and ΔR is the difference between both R_1 and R_2 as shown in Figure 2.1. The perpendicular baseline B_{\perp} , is the distance between the two satellite tracks perpendicular to the slant range and height of the target.

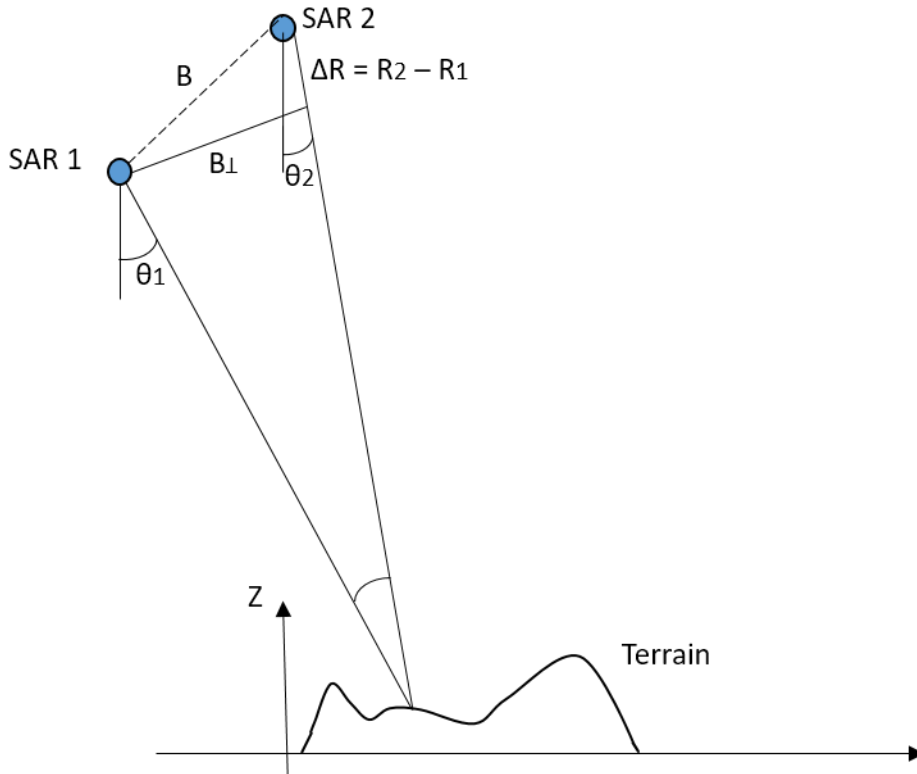


Figure 2.3. SAR Interferometry geometry

The interferometric phase ϕ_{int} , is contributed by different sources as given as,

$$\phi_{int} = \phi_{defo} + \phi_{topo} + \phi_{orb} + \phi_{ref} + \phi_{aps} + \phi_{noise} \quad (2.3)$$

The main contribution sources of this interferometric phase are the topography of the earth ϕ_{topo} , the reference surface of earth assumed by the SAR system ϕ_{ref} , the inaccurate orbital information ϕ_{orb} , the ground deformation between two acquisitions ϕ_{def} , the phase delay in the transmission and reception of this signal due to the atmosphere ϕ_{atm} , and other noise sources ϕ_{noise} . The major error sources are temporal change of scatters, defocusing, and mis-coregistration of two images.

The phase due to topography ϕ_{topo} , is derived from InSAR viewing geometry system as mentioned in (Zebker and Villasenor 1992, Massonnet et al. 1993) and defined as

$$\phi_{topo} = -\frac{4\pi B_{\perp} h}{\lambda R \sin\theta} \quad (2.4)$$

There are freely available external Digital Elevation Models (DEM) that provide a topography of the earth h such as Shuttle Radar Topography Mission (SRTM) Dem with 30m and 90m spatial resolution (Farr et al. 2007).

When the satellite orbits are not parallel to each other acquisitions, the phase difference between two points is then related to range distance difference ΔR between them. Due to this effect, high-density interferometric fringes appear even when the earth's surface is flat. This component of the phase should be removed from the total interferometric phase. This process is known as interferogram flattening and this phase difference between two points is given as (Hanssen 2001),

$$\phi_{ref} = -\frac{4\pi B_{\perp} \Delta R}{\lambda R \tan \theta} \quad (2.5)$$

The phase due to inaccurate orbital information ϕ_{orb} , is removed by using precise orbital information provided by the satellite agencies, European Space Agency (ESA) in the case of Sentinel-1 data.

The phase due to the ground displacements ϕ_{defo} , is due to the change in the target position between the two SAR acquisitions along the line the sight direction and for the displacement d , the deformation phase is given as,

$$\phi_{defo} = -\frac{4\pi d}{\lambda} \quad (2.6)$$

Differential-Interferometric SAR (D-InSAR) is a technique to estimate the ground deformation ϕ_{defo} , between two acquisitions along the line of sight by computing the parameters listed in Equation 2.1. The two-pass D-InSAR technique uses the externally available topography information to be removed from the interferometric phase (Massonnet and Feigl 1998).

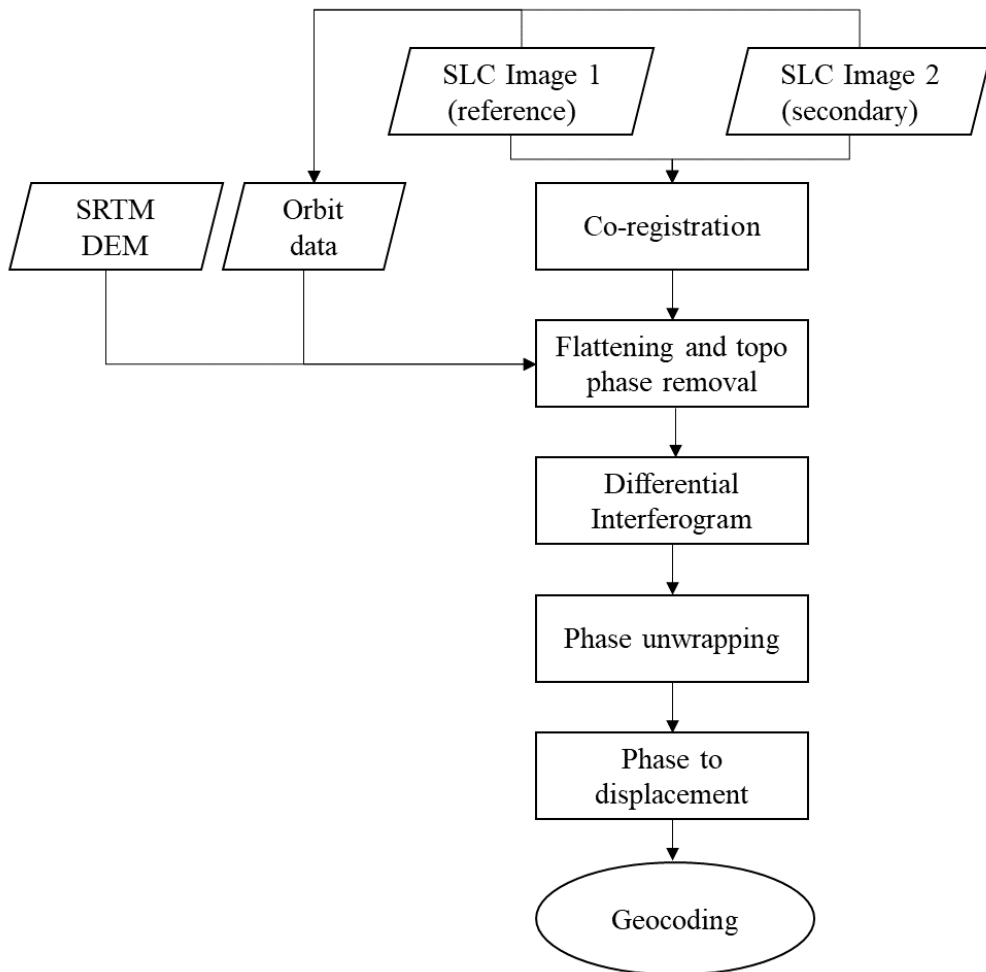


Figure 2.4 Processing flow to create ground displacement maps using SAR data

The computed parameters in Equation 2.1 are then removed from the interferometric phase and therefore, the remaining wrapped phase contains the phase contribution due to deformation and other noise sources. Figure 2.2 outlines the processing flow to obtain displacement maps from SAR images. First, the two SAR images are co-registered using DEM and orbital information. The interferogram is formed by subtracting the phase of the secondary image from the phase of the reference image. The topography contribution

is then removed using SRTM DEM to generate differential interferograms. Subsequently, the wrapped phase is then unwrapped, where the modulo of the 2π phase is converted into an absolute phase measurement. Finally, the deformation phase ϕ_{defo} is converted into the ground displacement and then geocoded to find the exact location of the deformation at each pixel. The deformation in these differential interferograms may be affected by noise sources and several other decorrelation sources. The major decorrelation sources are from spatial decorrelation sources due to large perpendicular baselines and temporal decorrelation due to the phase delay variations by the atmosphere, weather changes and, change in scattering properties of the surface with time such as seasonal vegetation changes. All these factors make the coherence too low and no measurement is possible to determine the deformation signal using conventional D-InSAR when the acquisitions are having a large perpendicular baseline B_{perp} and temporal baseline B_{temp} . For a given pixel in a differential interferogram, coherence γ , is calculated as a quality measure for the phase difference between two SAR scenes at that point and is defined as (Hanssen 2001),

$$\gamma = \frac{E\{S_1 \cdot S_2^*\}}{\sqrt{E\{S_1 \cdot S_1^*\} \cdot E\{S_2 \cdot S_2^*\}}} \quad (2.7)$$

Where E is the expected value of complex values of SAR scenes S_1 and S_2 , respectively. S_1^* and S_2^* are complex conjugates of the SAR scene 1 and SAR scene 2. The coherence value ranges from 0 to 1, where pixels close to 1 are considered as coherent or correlated and pixels close to 0 are considered as incoherent or decorrelated. According to (Zebker and Villasenor 1992), coherence is described as the product of thermal coherence, spatial coherence, and temporal coherence. Among them, temporal coherence is very important

in the case of measuring the temporal changes of the ground elevation. The temporal baseline is defined as the time between two SAR acquisitions, the longer the temporal baseline tends to decrease the temporal coherence, therefore the higher the likelihood of temporal decorrelation. Similarly, the longer the perpendicular baseline between the SAR images, the higher the likelihood of spatial decorrelation. In order to overcome these limitations to a certain extent, the stacking of D-InSAR images is formed along the time, also known as time-series SAR interferometry.

2.5.2. Time-series SAR interferometry

The development of interferometric time-series analysis due to the decorrelation sources in the conventional D-InSAR is inevitable. Time-series InSAR technique utilizes a set of SAR images to estimate the ground displacements over time. Differential interferograms are stacked following the criteria based on the different baseline configurations of the SAR images. Coherent point scatterers are identified for time-series analysis to overcome the limitations due to decorrelation. The framework of time-series Persistent Scatterers Interferometry (PSI), was proposed by (Ferretti, Prati, and Rocca 2001). Persistent scatterer interferometry technique generates the stack of single reference interferograms and identifies the coherent pixels, referred as persistent scatterer (PS). Due to the temporal characteristics, the decorrelation problem in the conventional D-InSAR approach can be minimized in the PS pixels for precise estimation of ground deformation. Following that, small baseline subset (SBAS) InSAR technique was proposed by Berardino et al. (2002) having multi-looked and unwrapped interferograms generated with the network of small perpendicular and temporal baselines. PSI and SBAS are the most well-known techniques of time-series techniques.

Numerous stack-processing approaches have been proposed, however, the PS-InSAR and SBAS are considered as broad classification for time-series InSAR techniques. PSI techniques refer to the analysis with PS pixels and single reference configurations, in other words, PSI identifies pixels in the SAR data that are dominated by a single stable scatter in a series of interferograms (Hooper et al. 2004). Several approaches were presented to identify the stable scatters, PSI was first developed by (Ferretti, Prati, and Rocca 2001), Delft PSI (DePSI) was developed by (Colesanti et al. 2003) and these approaches were successful in the urban areas than in natural terrains. To overcome these limitations and to identify the PSI method over non-urban areas, Stanford Method for Persistent Scatterers (StaMPS) was later developed by (Hooper et al. 2004). StaMPS identifies coherent scatterer candidates based on phase characteristics and finds low amplitude pixels with stable phase, which are not identified by other PSI methods.

2.5.3. Stanford Method for Persistent Scatterers (StaMPS)

StaMPS framework was initially developed for PS applications in the natural terrain (Hooper et al. 2004, Hooper, Segall, and Zebker 2007) and later extended to include small baseline analysis (Hooper 2008). For PS-InSAR analysis, a set of N co-registered single look complex (SLC) or multi look complex (MLC) scenes and $N-1$ single-reference interferograms are analyzed, and then a single reference scene has been selected to minimize the decorrelation effects (Hooper, Segall, and Zebker 2007). In this subsection, time-series StaMPS-SBAS algorithm is discussed, which was developed by (Hooper 2008).

Standard SBAS methods (Berardino et al. 2002), employ interferograms, which are multi-looked first and then unwrapped individually. This approach has the disadvantages of low spatial resolution and unwrapping the interferogram phase in the space domain only. Whereas, the StaMPS-SBAS approach has the advantage to process the SAR data at the highest possible resolution, to identify the slowly-decorrelating filtered phase (SDFP) pixels, and has the ability to unwrap the phase in both space and time (Hooper 2008). Each processing for Stanford method for Persistent Scatterer framework for SBAS algorithm is discussed as follows.

Preliminary coherent pixel candidate selection for StaMPS-SBAS

Amplitude difference dispersion Index $D_{\Delta,A}$ is defined as the ratio of the standard deviation of the difference in amplitude between reference and secondary $\sigma_{\Delta,A}$ and mean amplitude μ_A . This ADD index is similar to the amplitude dispersion index used in PSI (Ferretti, Prati, and Rocca 2001). Based on the threshold, the initial SDFP pixels candidates are selected for further processing, typically 0.6. This threshold primarily eliminates the areas covered by water and heavily decorrelated areas in densely vegetated areas.

$$D_{\Delta,A} = \frac{\sigma_{\Delta,A}}{\mu_A} \quad (2.8)$$

$$D_{\Delta,A} = \frac{\sigma_{\Delta A}}{\mu_A} = \frac{\sqrt{\frac{\sum_{i=1}^N (|M_i| - |S_i|)^2}{N}}}{\frac{1}{2N} \sum_{i=1}^N |S_i|} \quad (2.9)$$

Where, $\sigma_{\Delta A}$ is the standard deviation of the difference in amplitude between reference and secondary, and s_i is the amplitude of the pixel in the i th image, \bar{s} is the mean amplitude and N is the number of images. The simple thresholding of Amplitude Dispersion Index (ADI)

The interferometric phase of a pixel represented in Eq. 2.1 is generalized as,

$$\phi_{int,x,i} = \phi_{defo,x,i} + \Delta\phi_{topo,x,i} + \phi_{atm,x,i} + \Delta\phi_{orb,x,i} + \phi_{n,x,i} \quad (2.10)$$

The interferometric phase for a given SDFP pixel candidate (Equation 2.10) has different components, the topographic error and deformation signal correlate with each other, however, due to varying characteristics of the atmosphere between acquisitions, it is considered uncorrelated. Therefore, the spatially correlated terms in Equation 2.10 are estimated and removed from $\phi_{int,x,i}$, following that the phase due to the DEM error $\Delta\phi_{topo,x,i}$, is estimated using the baseline stack of interferograms. The residual phase are then considered as random noise of scatterer for each SDFP pixel candidate and used to compute the temporal coherence as described in (Hooper, Segall, and Zebker 2007, Hooper 2008).

Following the initial SDFP candidate selection, the phase stability of initial SDFP pixels is analyzed by using the phase contribution from random noise term and temporal coherence estimated. It is found there is a probability that the SDFP candidate with random phase noise can also have high temporal coherence γ , hence the gamma threshold γ_{thres} is defined and SDFP candidates greater than the gamma threshold are identified as SDFP pixels (Hooper 2008).

$$\gamma_x = \frac{1}{N} \left| \sum_{i=1}^N e^{j(\varphi_{x,i} - \bar{\varphi}_{x,i} - \Delta\hat{\varphi}_{x,i}^u)} \right| \quad (2.11)$$

Where N is the number of interferograms, $\varphi_{x,i}$ is the differential interferometric phase of x pixel in the i th interferogram. $\bar{\varphi}_{x,i}$ is the spatially correlated terms including deformation, atmospheric contribution, orbital error, and spatially correlated topographic phase due to DEM error which are computed iteratively using a combined low pass and adaptive phase filters. $\Delta\hat{\varphi}_{x,i}^u$ is the spatially uncorrelated part of the topographic phase that correlated with perpendicular baseline.

The wrapped phase of the selected SDFP pixels that are corrected for spatially correlated error terms and un-correlated error terms are then unwrapped using the 3D phase unwrapping method (Hooper and Zebker 2007, Hooper 2009). The unwrapped phase may still contain the spatially correlated error terms including DEM error, atmosphere, and orbit error. These error terms are estimated by high pass filtering the unwrapped phase temporally and low pass filtering spatially. The unwrapped phase of the small baseline interferograms is then inverted to derive the time-series phase change for each pixel using singular value decomposition (SVD) (Berardino et al. 2002). The phase change for each pixel due to the ground displacement estimated is relative to an arbitrary reference pixel and the selected reference image. The line of sight displacement rate is then estimated using the linear model technique. The StaMPS software developed by (Hooper et al. 2012) implements each processing of SBAS algorithms described above. In this thesis, the StaMPS software is used to apply the time-series InSAR approach on Sentinel-1 SAR data.

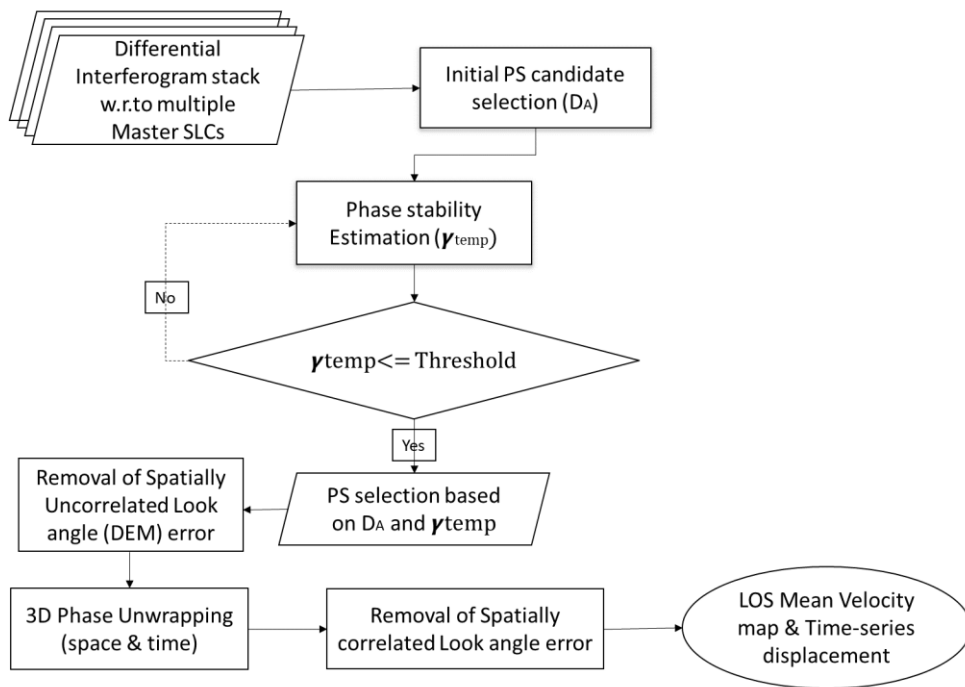


Figure 2.5. StaMPS time-series PS-InSAR processing flow

Chapter 3.

Vertical Land Motion estimation at Tide gauge using Time-series

PS-InSAR technique: A case study for Pohang tide gauge

"Sinking Tide Gauge Revealed by Space-borne InSAR: Implications for Sea Level Acceleration at Pohang, South Korea [P.V.S.Krishnan et al., 2019]"

3.1. Background

In this chapter, we tested the feasibility of employing the time-series SAR interferometric techniques to measure the VLM at tide gauges using the Sentinel-1 A/B SAR data. We chose the Pohang tide gauge in the Korean peninsula for this study.

According to Korea Hydrographic and Oceanographic Agency's report (KHOA), the mean SLR along the entire coast of Korea during 1971-2010 was 2.48 mm/year which is greater than the global mean SLR (i.e., 2 ± 0.3 mm/year) (Lim, Park, Kim, Woo, & Jeong, 2017). The South Korean peninsula is located in the southeastern part of Asia that has several tidal gauge stations along the coastal lines and continuously records the sea level changes (Figure 1). Among these stations, Pohang, Ulsan, Mokpo, Busan, Mukho are recording longer than 50 years (Kim & Cho, 2016). Recent studies have indicated that few specific tidal gauge stations on the east coasts of Korea have shown inconsistent relative SLR in recent years (Kim & Cho, 2016; Lim et al., 2017). Among them, the Pohang tidal gauge station has observed the highest relative SLR since the year 2010. The Pohang tidal gauge station is located along with the breakwater structure at Guhang, Pohang port, which constructed with one end linked to coasts and a distance away from

the coasts as shown in Figure 3.1. The hypothesis constitutes that the vicinity of the Pohang tidal gauge has considerably suffered by the earth's surface displacements, which may influence sea level records. Little research has been conducted on understanding the reason for the rapid increase in SLR and assessing the vertical ground motion over the tidal gauges installed on the eastern coast of the Korean Peninsula.

In this section, I aim to estimate the vertical land motion in the Pohang tidal gauge station by incorporating multi-track PS-InSAR time-series analysis to evaluate the driver for overestimated sea level rise. The reliability of vertical velocity is validated against the available GPS observations that collocated on the tidal gauge station. This study will corroborate that the vertical land motion at tidal gauge station and in the vicinity of the Pohang region significantly influences the sea level changes observed by Pohang tidal gauge. Subsequently, the influence of vertical ground motion on the rate of the Pohang sea level rise is discussed. Finally, the difference between the rates of vertical ground motion rate and sea level rise is taken into account to reconstruct the corrected rate of sea level rise at the Pohang tidal gauge over the period from 2013.

3.2.VLM estimation at Pohang tide gauge using StaMPS-PSI analysis

3.2.1. Description of the case study area

The Pohang tide gauge stations is located on the southeastern coast of the Korean peninsula, in the Pohang basin (Figure 3.1). The coastline borders the East Sea, a marginal sea between the Korean peninsula, Japan, and Russia. The Pohang basin has witnessed extensive land reclamation over past years, as the city is one of the economic zones of Korea. In particular, the Guhang port area, where the tide gauge is grounded, is built on the reclaimed land of the Hyongsan River. The Pohang tide gauge station has measured sea level records continuously since 1977 (KHOA). Based on the Intergovernmental Panel on Climate Change Fourth Assessment Report (IPCC AR4), Pohang has shown increasing trends of extreme precipitation; however, its relationship with a low-frequency climate such as the El Niño-Southern Oscillation (ENSO) still need to be investigated (Jung 2008). Seasonal analysis of long-term meteorological and hydrological variables suggests that the high intensity of precipitation along the East coast is mainly due to typhoons and extreme rain events (Park et al. 2011). In recent years, a permanent GPS station (POHA) has been collocated at the Pohang Tide Gauge Station; it is maintained by KHOA.

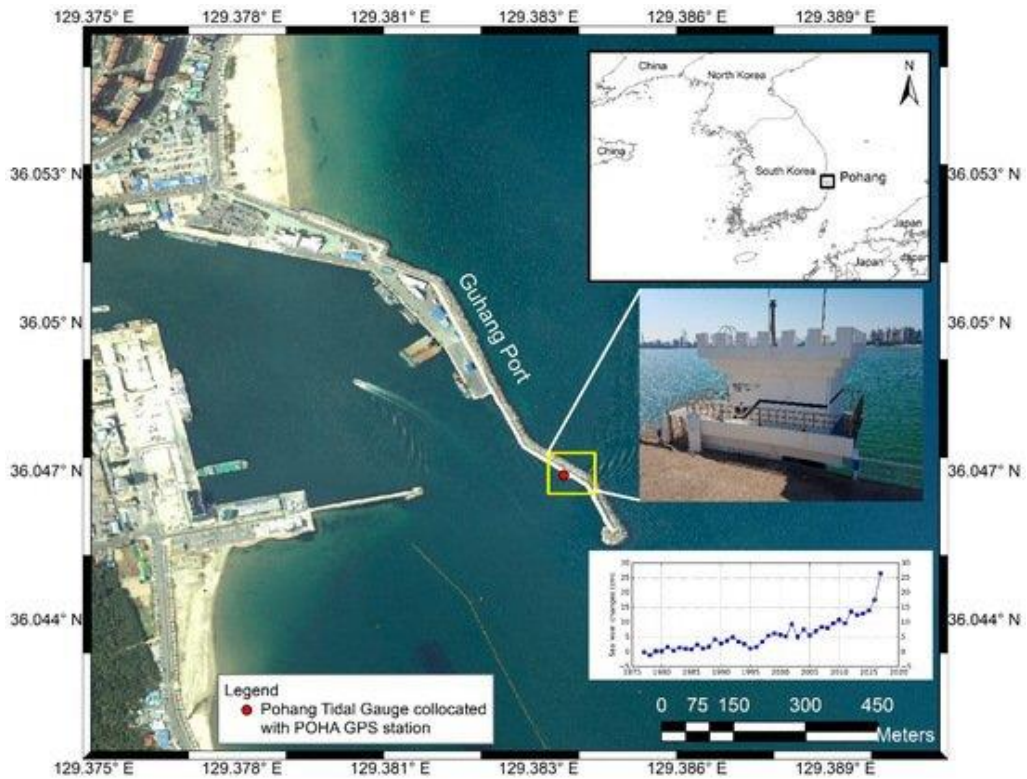


Figure 3.1 Study Area map of Pohang tide gauges station located in the Korean Peninsula

3.2.2. Data description

The sentinel-1 A & B satellite is an Earth observation mission launched in 2014 and 2016, respectively by the European Space Agency (ESA). These satellites are in a 98.6° sun-synchronous orbit at 693 km altitude, operate in four acquisition modes with a 6 and 12 days repeat cycle. Sentinel-1 carries a single C-band synthetic aperture radar instrument operating at a center frequency of 5.405 GHz. The right-looking instrument supports the operation in dual-polarization (HH +HV, VV+ VH). The acquisition modes shown in Figure 3.2 are:

- Strip map (SM)
- Interferometric Wide swath (IW)
- Extra-wide swath (EW)
- Wave mode (WV)

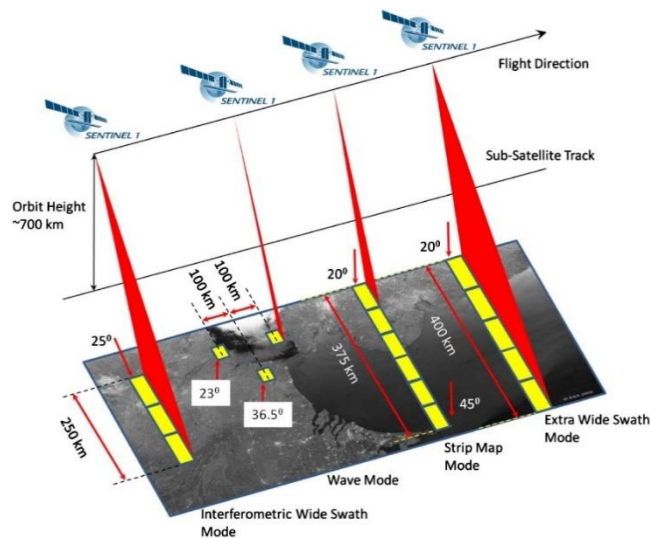


Figure 3.2. Acquisition modes of Sentinel-1 A/B (Source: European Space Agency)

In this thesis, IW mode SAR data is used, which allows combining a large swath width (250 km) with a spatial resolution of 5 m by 20 m. The incidence angle varies from 31° - 41° . The IW mode is the default acquisition mode over land that images three sub-swaths using terrain observation with progressive scans SAR (TOPSAR). IW mode data has three levels of products: Level 0: RAW, Level 1: single-look complex (SLC) and Level 2: ground range detected (GRD). Level 1 SLC products that preserve the phase information are used for interferometry analysis.

49 SAR scenes in ascending and 42 scenes in descending track acquired by C-band Sentinel-1 A/B from 2015 to 2017. Sentinel-1 SAR sensors has the ability to cover the larger ground area (i.e., 250 km swath) and have a revisit cycle of 6 days. The detailed descriptions of data acquisitions are shown in Table 3.1. The stack of multi-looked interferograms (2 range x 1 azimuth looks) resulting in spatial resolution of 10 x 20 meters were generated. In this study, Sentinel-1 TOPS InSAR processing was performed to generate interferograms with a single reference scene using ISCE software (Agram et al. 2013, Rosen et al. 2012). SRTM DEM having 30 m spatial resolution is used to remove the topographic phase effect from the interferometric phase. Time-series PSI processing was applied using the Stanford Method of Persistent Scatterer (StaMPS) to estimate the ground displacement over the study period (Hooper et al. 2004). In this method, the persistent scatterers were iteratively selected as target pixels that were found to be phase stable over a period. StaMPS PS-InSAR algorithm incorporates advanced time-series processing steps to reduce the decorrelation noise in the differential interferograms. Therefore, several components including displacement, atmospheric components, and topographic error (DEM error) can be estimated iteratively and

removed to obtain coherent pixels having minimized spatial and temporal decorrelation noise level (Hooper et al. 2004). Subsequently, the time-series surface displacement rate was estimated with respect to a reference point that was presumed as a nearly stable ground location.

Table 3.1. Detailed description of Sentinel-1 A/B SAR scenes used in this Chapter 3.2 for StaMPS-PSI analysis

Description	Ascending	Descending
Acquisition Mode	Interferometric Wide swath (IW)	
No. of scenes	49	42
Incidence angle	40°	39°
Temporal coverage	2014/11 – 2017/12	2015/05 – 2018/05
Azimuth heading angle	11°	169°

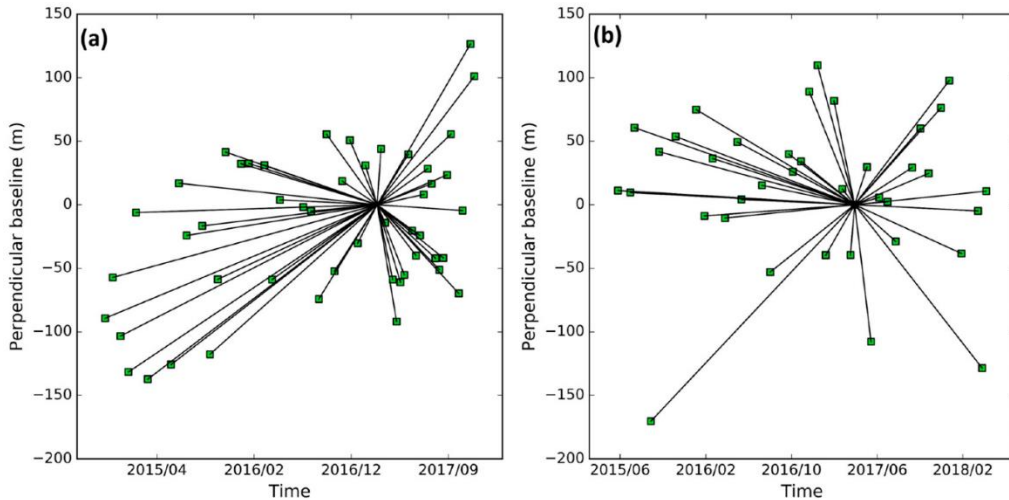


Figure 3.3 Sentinel-1 A/B acquisition time with the perpendicular baseline for (a) ascending (reference: 2017/02/19) and (b) descending (reference: 2017/04/14) passes.

In order to estimate the time-series linear trend of sea level change, since the year 2013, hourly sea level records from Pohang tidal gauge station were obtained from Korea Hydrographic Observation Agency (KHOA). The sea level records used in this study were corrected for local datum over the period. The sea-level trend analyses have been performed to decompose the trend, seasonality, and residual components from observed sea level records. The sea level records are available from the year 1977 – 2017; however, the focus is mainly on the recent year records, as the sea level changes were significant since 2013. In addition, the continuous GPS observations since 2013 from the POHA station that collocated with Pohang tidal gauge were supplemented by KHOA.

3.2.3. Results: Extraction of vertical land motions at Pohang tide gauge

Time-series StaMPS PSI processing was applied as described in Chapter 2.5 to estimate ground displacement over the study period (Hooper et al. 2004, Hooper, Segall, and Zebker 2007). In this method, initial PS candidates are selected based on the amplitude dispersion index criterion. In this step, if the ratio between the standard deviation and mean amplitude in time is smaller than a threshold value of 0.4, then such pixels are selected as initial PS candidates to form the reference network for further processing. Following that, the phase values of these PS candidates are filtered with neighboring pixels assuming that the deformation, orbital error, and atmospheric artifacts are spatially correlated by bandpass filtering. Then, persistent scatterers are iteratively selected as target pixels found to be phase stable over a period using a measure called temporal coherence. Residual PS candidates having temporal coherence of <0.3 are filtered out at this stage. The resulting PS pixels have minimized spatial and temporal decorrelation noise levels.

The StaMPS PS-InSAR algorithm incorporates advanced time-series processing steps to reduce the decorrelation of noise in the differential interferograms. Furthermore, residual topographic errors that are spatially uncorrelated but correlated with perpendicular baseline information were removed by the least square method before phase unwrapping. The wrapped phase of the PS pixels was unwrapped by 3D (phase in space and time field) unwrapping using the SNAPHU algorithm (Chen and Zebker 2001). The thresholds were carefully selected for filter grid size, and an unwrapped grid size of 5×5 was used to control phase unwrapping errors. Spatial filtering was then applied for the re-estimation of atmospheric and look-angle errors. Subsequently, the time-series surface displacement rate was estimated with respect to a reference point that presumed a nearly-stable ground location.

The mean velocity map obtained from the PSI analysis is presented in Figure 3.4. These PSI results indicate ground motion along with the satellite LOS. PS pixels were identified in the urban areas of Pohang, and especially on the Pohang tide gauge. The time-series PSI results reveal that the vicinity of the Pohang Tide Gauge Station is affected by significant relative ground motion away from the satellite. Mean LOS displacement rates of approximately -1.85 cm/year and -1.92 cm/year were observed in ascending (Figure 3.4 (a)) and descending (Figure 3.4 (b)) passes, respectively. Other than the Pohang Tide Gauge Station and its neighborhood, most of the study area appeared stable, with minimum downward ground motion and no significant uplift based on PSI results. Time-series profiles show a linear LOS displacement trend at the tide gauge location over the study period for both ascending and descending tracks (Figure 3.4 (c)).

It is worth noting that the LOS displacements at the tide gauge station for both passes showed a similar and constant linear trend.

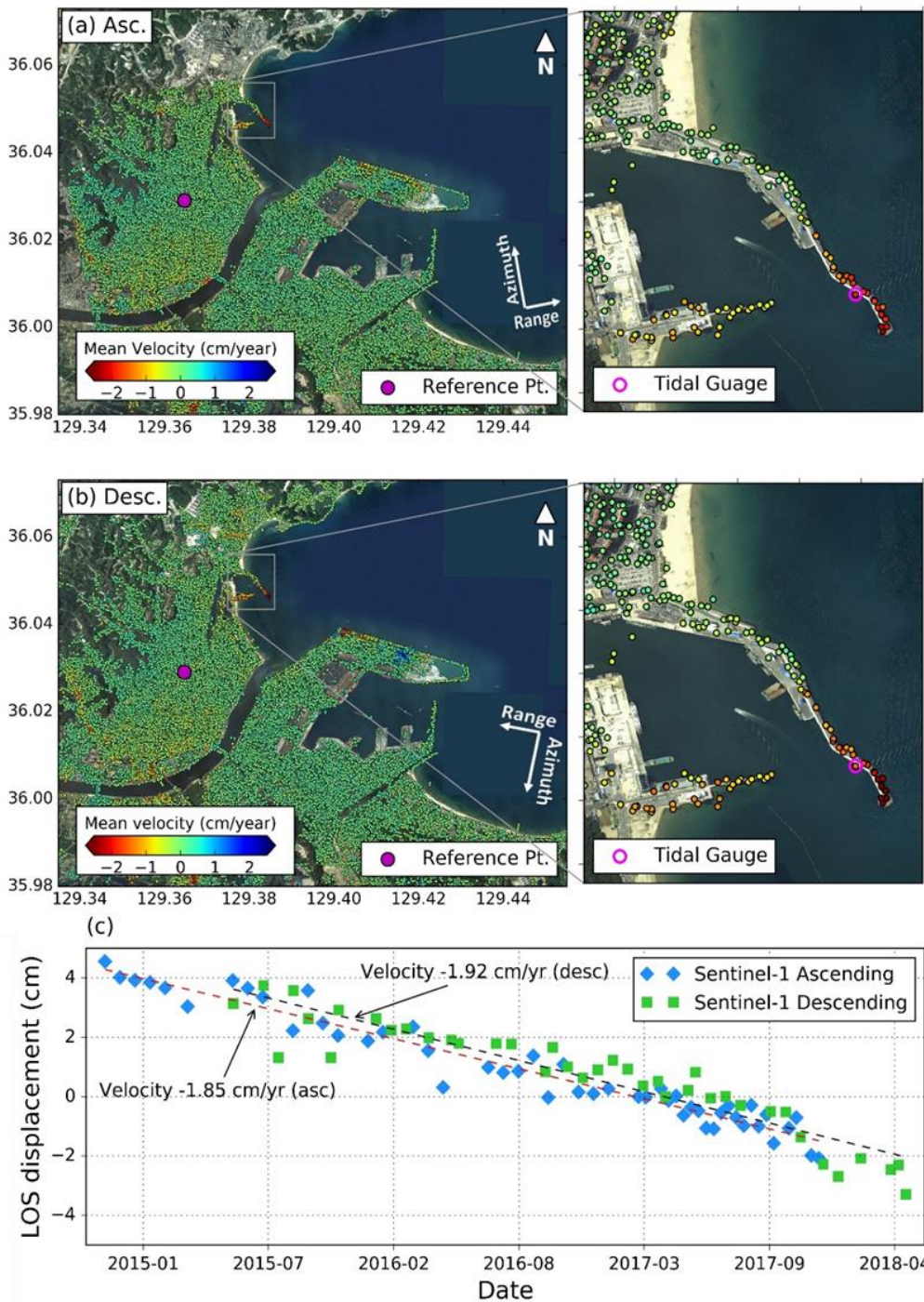


Figure 3.4. Line of sight velocities from the time-series interferometry results obtained from (a) Ascending track (2014/11 – 2017/12) and (b) descending track (2015/05 – 2018/05). The Negative values indicate displacement away from the satellite (c) Time-series InSAR displacement at Pohang tidal gauge station for ascending (blue) and descending track (green).

Using the area that overlapped in both the spatial and temporal coverage of Sentinel-1 for the ascending/descending data, PSI results with respect to a common reference point were interpolated by cubic interpolation on the uniform grid before 2D decomposition. With the availability of LOS displacement for the two different geometries, the vertical (d_{ver}) and horizontal displacement components (d_{hor}) were reconstructed, as presented in Equation 3.1 (Samieie-Esfahany et al. 2009):

$$\begin{bmatrix} d_{asc} \\ d_{dsc} \end{bmatrix} = \begin{bmatrix} \cos \theta_{asc} & -\cos \alpha_{asc} \sin \theta_{asc} \\ \cos \theta_{dsc} & -\cos \alpha_{dsc} \sin \theta_{dsc} \end{bmatrix} \begin{bmatrix} d_{ver} \\ d_{hor} \end{bmatrix} \quad (3.1)$$

where d_{asc} and d_{dsc} are displacement along LOS in ascending and descending mode, respectively; θ_{asc} and θ_{dsc} are incidence angle in ascending and descending mode, respectively; α_{asc} , α_{dsc} are the satellite heading angle for ascending and descending passes; and d_{ver} and d_{hor} are vertical displacement and horizontal displacement, respectively, along the East-West direction.

The projections of the ENU vector components of the LOS velocities are presented in Figure 3.5. The horizontal component of LOS is perpendicular to the satellite heading and comprises the combined contributions of the E-W and N-S components. In the across-track SAR imaging system, sensitivity towards N-S components is much smaller

than sensitivity towards E-W components. The decomposed vertical and horizontal displacements were obtained according to the incidence angles of ascending and descending passes. Hence, it is assumed that the derived horizontal component represents the E-W velocity component along the descending Azimuth look direction.

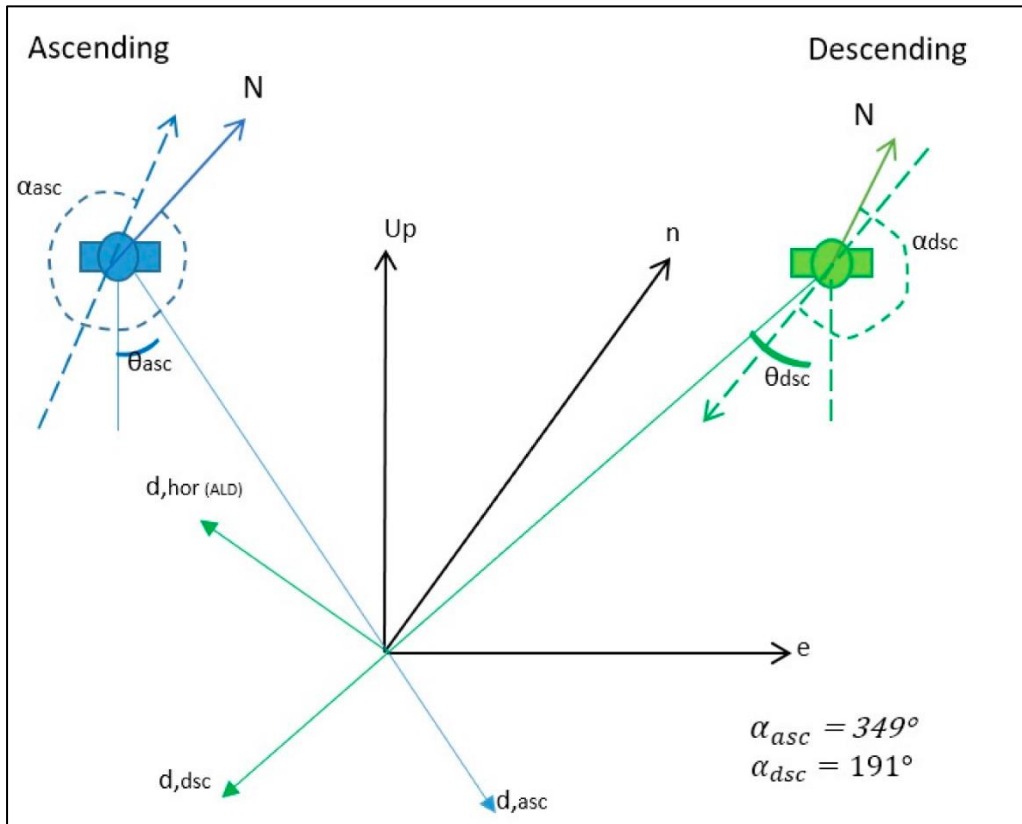


Figure 3.5 Projection of InSAR LOS velocity decomposition into 2D velocity components along the vertical and horizontal directions

The study area that overlapped for both spatial and temporal coverage of Sentinel-1 ascending/descending data was identified. With the availability of a line of sight

displacement in two different geometries, the vertical and horizontal displacement components (along azimuth look direction) have been reconstructed using Equation 3.1 as reported by (Samieie-Esfahany et al. 2009). The PSI results from ascending and descending orbit with respect to common reference points were interpolated by the cubic interpolation method on the uniform grid before 2D decomposition. The decomposed vertical and horizontal components for the overlapping period (2015/05 – 2017/12) were presented in Figure 3.6 a, b, respectively. It is very clear that the ground motions detected over the study area by PSI analysis have primarily undergone vertical movement and minimum to zero horizontal movements. Subsequently, the velocity of ground motion in the vertical and horizontal direction is about -2.53 cm/year and +0.01 cm/year, respectively.

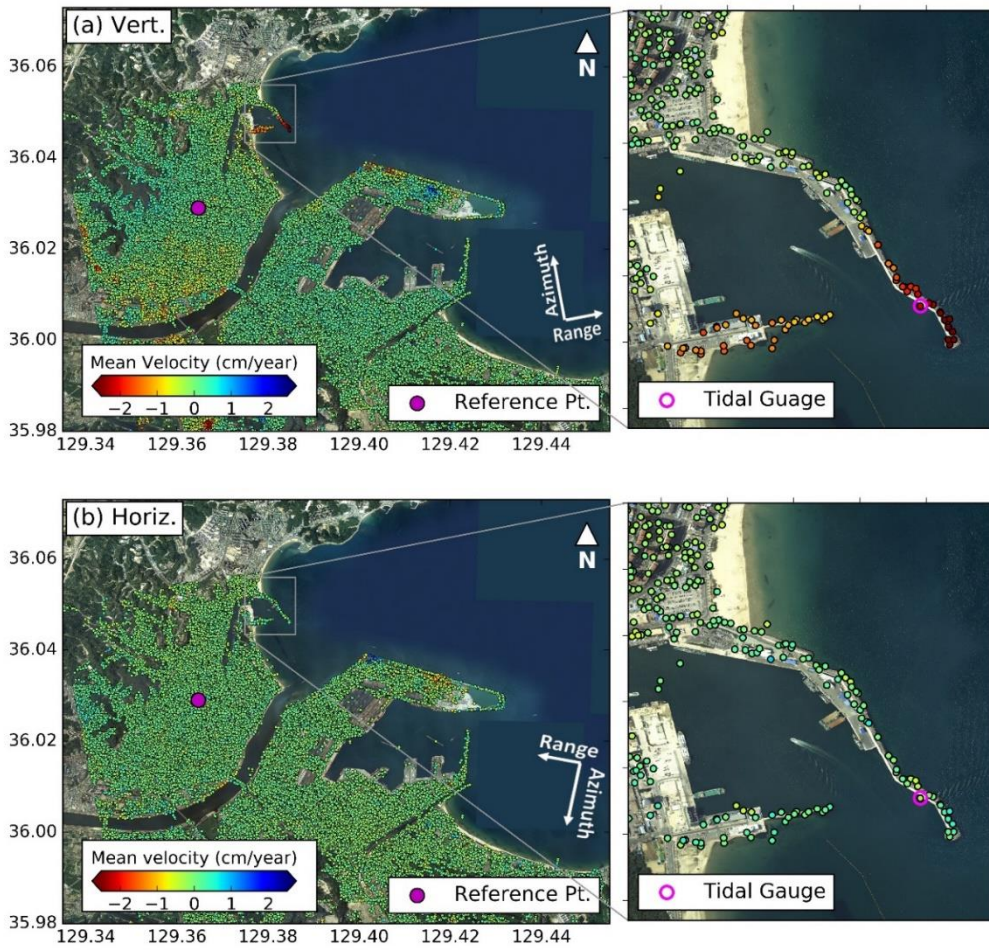


Figure 3.6. InSAR derived ground motion velocity over the period (2015/-5 – 2017/12)

(a) Vertical ground motion component (b) Horizontal ground motion component.

3.2.4. Comparison of InSAR VLM and GNSS, Levelling VLM

The vertical velocity at POHA station was found to be -2.67 cm/year during the year 2013-2017 with respect to ITRF 2008 reference coordinate system (Figure 3.7). The horizontal movement of these GPS stations shows that these stations are appeared to be stable. The temporal profiles for vertical ground motions estimated from POHA GPS and PS-InSAR analyses and non-seasonal sea level trend computed from Pohang tidal gauge were presented in Figure 3.8. The vertical and horizontal components of the continuous GPS station (POHA) that collocated with the Pohang tidal gauge station were estimated.

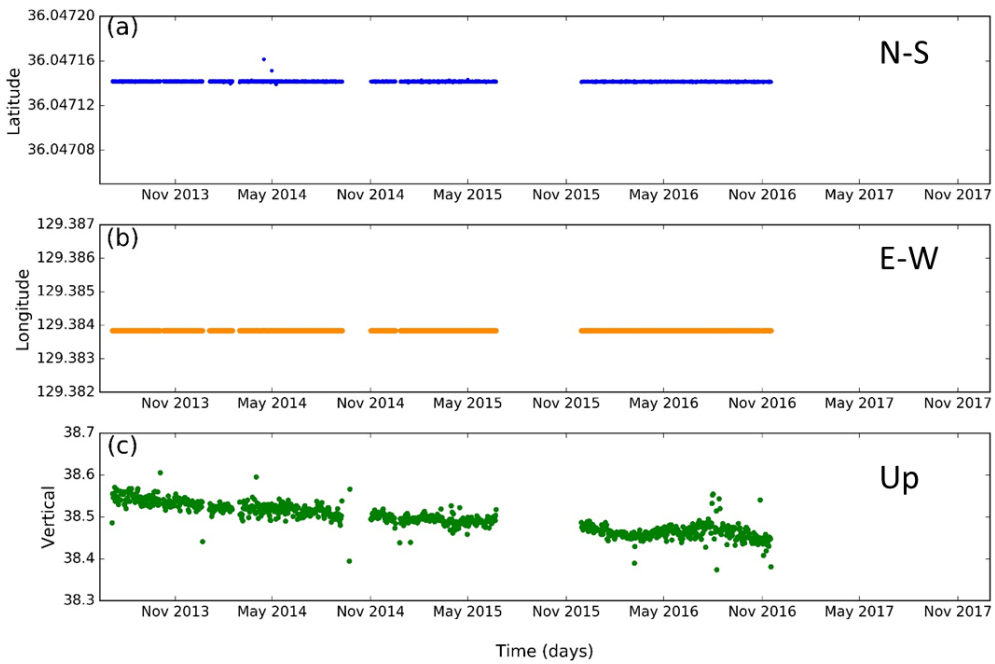


Figure 3.7. Global positioning system (GPS) displacements measured at the POHA station from 2013 to 2016 (KHOA). (a) North-South, (b) East-West, and (c) vertical displacements. Horizontal components are measured in degrees and vertical displacement is measured in meters.

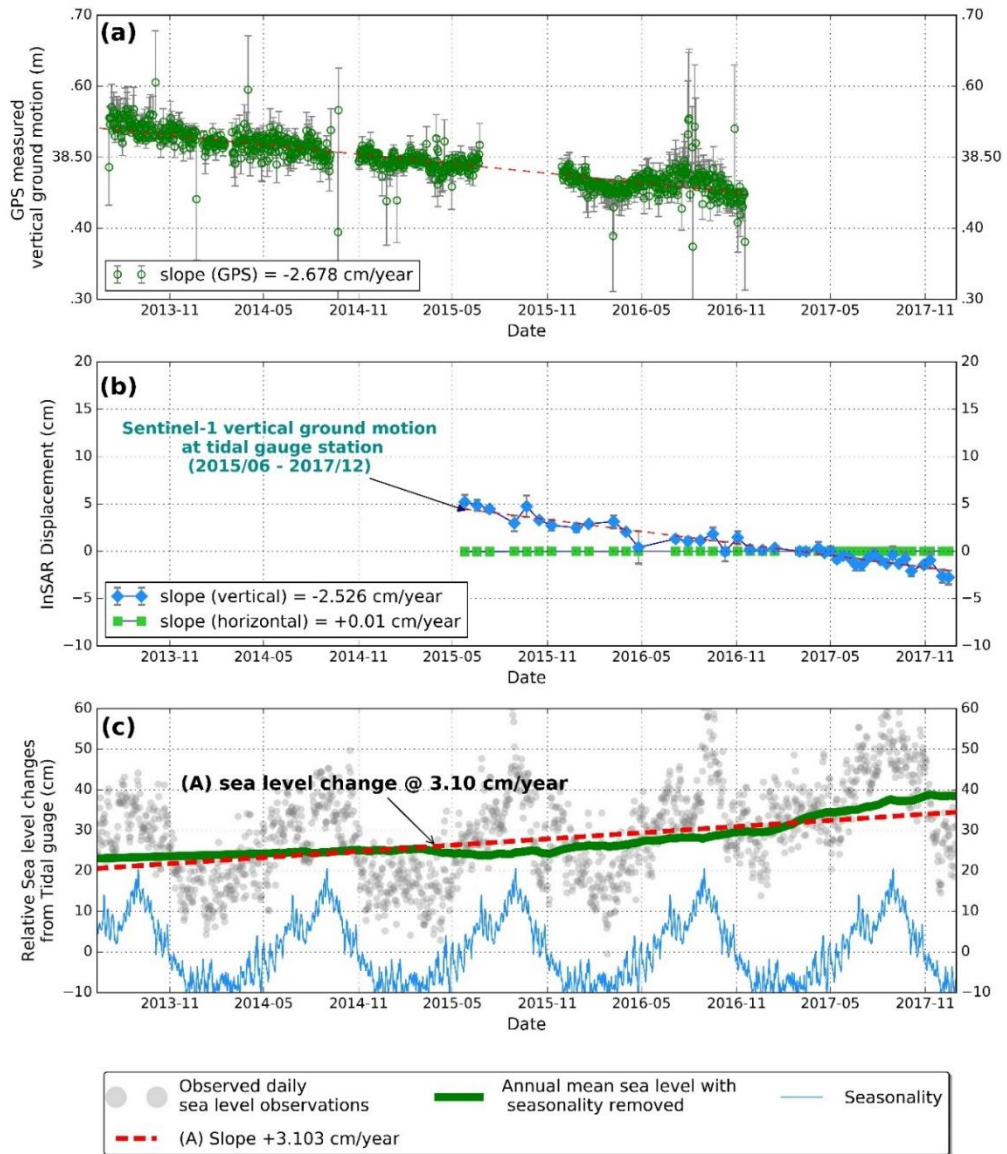


Figure 3.8. Temporal profiles of (a) Absolute vertical ground motion by GPS (b) Relative vertical ground motion from InSAR displacements (c) Sea level records observed at Pohang tidal gauge station since 2013.

3.2.5. *Discussion and Limitations*

The local sea level change at Pohang station has significant deviations from regional and global sea level change. Such sea level measurements may comprise large contributions of previously mentioned ground motions at tidal gauges and therefore sea level records vary considerably from nearby tidal gauge stations (Ulsan, Mukho) and also found contrast with the rate of global mean sea level.

The time-series PSI results reveal the vulnerable areas of the Pohang coast that experiencing the vertical (downward) ground motions (Figure 3.5). In particular, the breakwater where Pohang tidal gauge station is located has found to be subsided at the rate of 2.53 cm/year. It is worth noting that the InSAR displacements from both ascending and descending tracks showed similar displacement patterns (i.e., linear subsidence trend). Furthermore, the reliability of the PSI ground motion trend is in good agreement with the available continuous GPS vertical velocity profile (POHA) that collocated with Pohang tidal gauge station (Figure 3.8). Especially, the Guhang port area where the tidal gauge is grounded has been built on the reclaimed land of Hyongsan river. Our InSAR estimates showed severe subsidence signals on the Guhang port, which is about 2.53 cm/year on the tidal gauge (Figure 3.5). Ground motion in reclaimed land is primarily induced by the compaction of underneath clay soils (Jiang and Lin 2010). Thus, the ground deformations in this reclaimed land are expected to affect the tidal gauge and GPS observations in the Pohang.

After removing the seasonality in the observed tidal gauge observations, the non-seasonal sea level trend showed a significant SLR of about +3.1 cm/year at the Pohang

tidal gauge (Figure 3.8). However, the slope of SLR is quite large in recent years compared to the long-term sea level rise about 5.8 mm/year (Watson 2019). It is worth remarking that the SLR trend observed since 2015 is possibly the combination of original SLR and local ground motion. Therefore, the inference is made that the rapid increase in SLR is most likely as a result of the vertical ground motion (about -2.53 cm/year) along the breakwater. Furthermore, our InSAR estimates are substantiated by the strong agreement against the linear velocity of vertical ground motion observed from POHA GPS measurements (Figure 3.8). Additionally, it is expected that the difference between the linear sea level trend (+3.1 cm/year) and the estimated vertical ground motion (-2.53 cm/year) since 2013, (i.e., ~6 mm/year) is most likely the original sea level rise around the Korean peninsula.

As the tide gauges are installed along the coastlines, where the terrain might have both dominant scatters (coherent pixels) and non-dominant scatters (non-coherent). The terrain like the Pohang region discussed in this chapter consists of sufficient coherent pixels around the tide gauge areas, which have minimal phase due to decorrelation over time. However, the StaMPS PSI analysis discussed in this section has the challenge to identify PS pixels in the natural terrain. Therefore, it is desirable to form interferograms with short temporal SLC images, which minimize the decorrelation and able to detect underlying signal from non-dominant scatter.

3.3.Development of StaMPS-SBAS InSAR using Sequential InSAR pair selection suitable for coastal environments

"Monitoring the Vertical Land Motion of Tide Gauges and Its Impact on Relative Sea Level Changes in Korean Peninsula Using Sequential SBAS-InSAR Time-Series Analysis [P.V.S.Krishnan et al., 2021]"

For the multi-temporal InSAR analysis, I have employed the StaMPS-Small Baseline Subset (StaMPS-SBAS) time-series analysis of single-look slowly-decorrelating filtered phase (SDFP) pixels in a single-look interferogram (Hooper 2008, Hooper et al. 2012) to identify the isolated SDFP pixels surrounded by completely decorrelated pixels. Whereas, the standard SBAS methods work with interferograms that are multi-looked, filtered, and unwrapped the phase individually (Berardino et al. 2002). Also, a statistical cost flow 3D phase unwrapping (space and time) algorithm is applied to unwrapping the phase of SDFP pixels in the time-series multiple reference interferograms (Hooper 2009).

Fundamentally, a network of multiple reference interferograms is constructed based on small baseline methods that have minimized perpendicular, temporal, and Doppler baselines to reduce the decorrelation effects due to geometrical, temporal, and topographic errors. Further, spectral filtering in the range is applied to reduce the phase decorrelation and discards the non-overlapping Doppler frequencies in azimuth (Gatelli et al. 1994, Hooper 2008).

3.3.1. Sequential InSAR pair selection

In this study, a modified approach for the selection of interferograms is proposed to extend the amplitude difference dispersion index and optimize its measure to increase the

density of SDFP candidates. To minimize the $D_{\Delta,A}$ criterion, the time-series interferograms was formed in the sequential order ($n=5$) for the StaMPS-SBAS algorithm, rather than standard StaMPS small baseline interferograms as shown in Figure S1. The approach is referred to as sequential InSAR pair selection for StaMPS-SBAS. In this study, M SAR images are assumed to be connected to N interferograms and $N = (M \times n) - n$ under the condition of $n=5$ sequential SAR scenes. For *SAR scene 1*, the n interferograms are formed, this includes reference-reference interferograms as shown in Figure 3.9. Following that, utilizing temporal coherence γ_x (Equation. 2.11) to identify the SDFP pixels. The main objective of this approach is to minimize the $D_{\Delta,A}$ value of a pixel according to the Equation. 2.9. To demonstrate the efficiency of this sequential pair selection approach, the comparative study was conducted using standard SBAS pair selection and sequential pair selection for StaMPS-SBAS as described in Section 2.5.

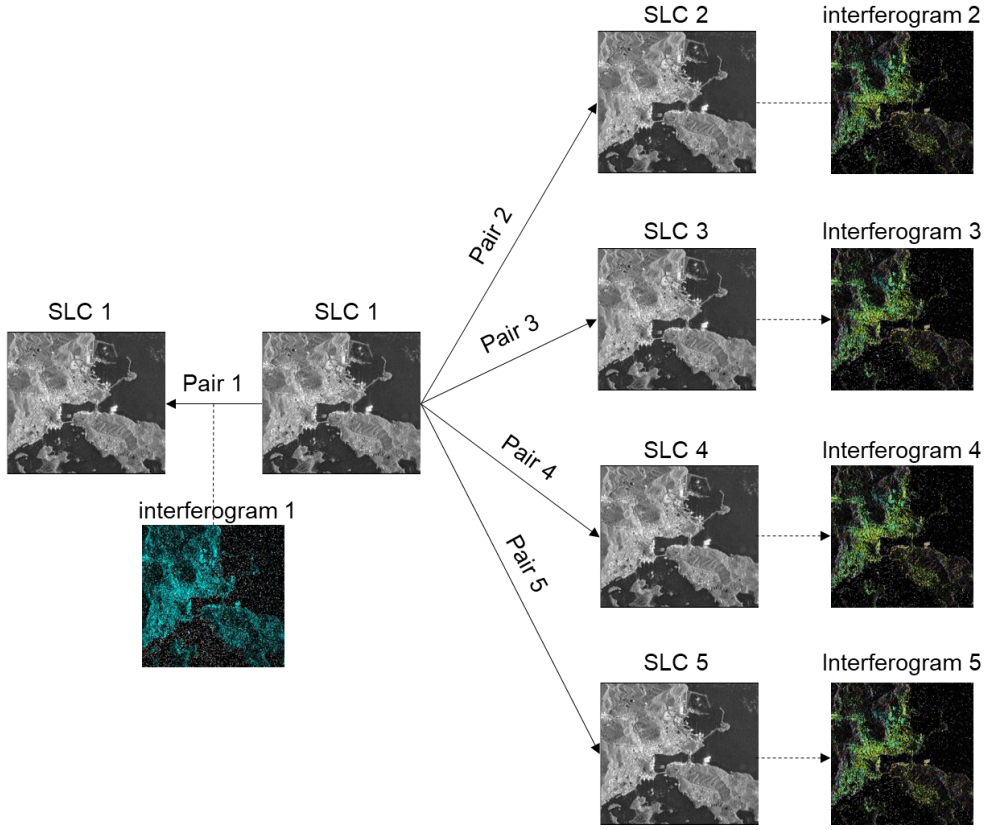


Figure 3.9. Sequential InSAR pair selection for StaMPS time-series InSAR analysis

The Amplitude Difference Dispersion (ADD) index for Sequential SBAS is presented below:

$$D_{\Delta, A}^{seq} = \frac{\sigma_{\Delta A}}{\mu_A} = \frac{\sqrt{\frac{\sum_{i=1}^{N_{seq}} (|M_i| - |S_i|)^2}{N_{seq}}}}{\frac{1}{2N_{seq}} \sum_{i=1}^{N_{seq}} |S_i|} \quad (3.2)$$

$$D_{\Delta,A}^{seq} = \frac{\sigma_{\Delta A}}{\mu_A} = \frac{\sqrt{\frac{\sum_{i=1}^{N_{conv}+N_s} (|M_i| - |S_i|)^2}{N_{conv} + N_s}}}{\frac{1}{2N_{conv} + N_s} \sum_{i=1}^{N_{conv} + N_s} |S_i|} \quad (3.3)$$

$$N_{seq} = N_{conv} + N_s \quad (3.4)$$

Where,

N_{conv} is the number of scenes for conventional SBAS

N_s is the number of scenes for reference-reference pairs

In this approach, both short temporal interferograms N_{conv} and reference-reference N_s interferograms pairs were selected for StaMPS-SBAS. As mentioned in the Equation 3.2, the ADD index is the ratio between the standard deviation amplitude difference and mean amplitude of the scenes. By introducing the reference-reference pairs, in the Equation 3.3, the sum of the amplitude difference remains unchanged, however the mean amplitude of the scenes has been modified for each pixels. In order to analyse the change of the mean amplitude between the conventional StaMPS-SBAS and Sequential SBAS, the relationship between the conventional and sequential ADD index were presented as below in Equation 3.5.

$$\frac{D_{\Delta,A}^{seq}}{D_{\Delta,A}^{conv}} = \frac{\mu_{\Delta A}^{conv}}{\mu_{\Delta A}^{seq}} \cdot \frac{\sigma_{\Delta A}^{seq}}{\sigma_{\Delta A}^{conv}} \quad (3.5)$$

As the sum of amplitude difference for sequential SBAS remains unchanged with reference to the conventional SBAS, the ratio of standard deviation of the amplitude

difference between conventional and sequential SBAS varies with number of scenes, subsequently, the equation 3.5 can be further expanded as shown in below:

$$\frac{\mu_{\Delta A}^{conv}}{\mu_{\Delta A}^{seq}} \cdot \frac{\sigma_{\Delta A}^{seq}}{\sigma_{\Delta A}^{conv}} = \frac{\frac{1}{2N_{conv}} \sum_{i=1}^{N_{conv}} |S_i|}{\frac{1}{2N_{conv} + N_s} \left| \sum_{i=1}^{N_{conv}} |S_i| + \sum_{i=1}^{N_s} |S_i| \right|} \cdot \frac{\sqrt{N_{conv}}}{\sqrt{N_{seq}}} \quad (3.6)$$

Because,

$$\frac{\mu_{\Delta A}^{conv}}{\mu_{\Delta A}^{seq}} = \frac{\frac{1}{2N_{conv}} \sum_{i=1}^{N_{conv}} |S_i|}{\frac{1}{2N_{conv} + N_s} \left| \sum_{i=1}^{N_{conv}} |S_i| + \sum_{i=1}^{N_s} |S_i| \right|} \quad (3.7)$$

The equation 3.7 can be simplified as shown in equation 3.8,

$$\frac{\mu_{\Delta A}^{conv}}{\mu_{\Delta A}^{seq}} = \frac{N_{conv} + N_s}{N_{conv}} \left| \frac{A}{A+B} \right| \quad (3.8)$$

Because,

$$A = \sum_{i=1}^{N_{conv}} |S_i|$$

$$B = \sum_{i=1}^{N_s} |S_i|$$

Finally, the relationship between the ADD of conventional and sequential SBAS can be described as below in equation 3.9:

$$D_{\Delta, A}^{seq} = \frac{N_{conv} + N_s}{N_{conv}} \left| \frac{A}{A+B} \right| \cdot \frac{\sqrt{N_{conv}}}{\sqrt{N_{seq}}} \times D_{\Delta, A}^{conv} \quad (3.9)$$

The relationship between the ADD for sequential and conventional SBAS in equation 3.9 shows that when the reference-reference pairs introduced to the SBAS interferograms network and therefore, the estimation of ADD index varies with respect to the mean amplitude of reference-reference pairs. As the number of scenes used in the sequential SBAS are greater than the conventional SBAS, the ADD index has been minimized and therefore, the initial pixel candidates on the coherent areas for time-series StaMPS SBAS has been increased. Though, the theoretical explanation for the selection of additional coherent pixels has not been analysed in detail, the experiment results on different coastal areas showed that the inclusion of reference-reference pairs in the SBAS network was found to be useful in the selection of additional candidates for time-series StaMPS-SBAS processing in the coastal regions.

3.3.2. Experimental results

To evaluate the approach, I have applied the sequential pair selection in the StaMPS-SBAS algorithm as outlined in the previous section to the Yeosu region, located in the southern part of the Korean Peninsula. The Yeosu region was chosen for this experimental setup as the terrain has both dominant (PS) and non-dominant scatter (DS). In this method, 60 scenes of Sentinel-1 A/B SLC scenes acquired during November 2014 and April 2019 in the descending mode. The TOPS stack Sentinel processor is implemented in this study using InSAR Scientific Computing Environment (ISCE) software (Rosen et al. 2012, Fattahi, Agram, and Simons 2017) to generate a stack of coregistered SLC images and resampled with respect to a reference acquisition (the first scene in the acquisition). Sentinel-1 Precise orbit data and 1-arc second DEM from Shuttle Radar Topography Mission (SRTM) were used in this processing to remove the topographic phase. To preserve the high-resolution phase information, we skipped the multi-looking step. Next, a network of single-look interferograms were generated for the subset area (1614 x 461 pixels) based on two cases (1) Standard StaMPS-SBAS pairs and (2) Sequential pair selection, $n=5$. For the standard SBAS approach, the interferogram pairs were formed with the thresholds of perpendicular baseline ($B_{\text{perp}} < \pm 250$ meters and temporal baseline ($B_{\text{temp}} < 250$ days which generates about 194 interferograms. On the other hand, for a sequential network, the interferograms were formed with nearest neighbor images of 5 connections. This includes reference-reference, reference-secondary1, reference-secondary2, reference-secondary3 and reference-secondary4, which generates 290 interferograms (Figure 3.10). As shown in Figure 3.10, by applying the proposed approach the histogram of $D_{\Delta A}$ values in sequential pair selection approach

are skewed to the lower values of $D_{\Delta,A}$ compared to standard SBAS. By applying the threshold value $D_{\Delta,A}$ less than 0.6, more SDFP candidates having low amplitude pixels are selected in the sequential pair selection compared to standard SBAS pair selection.

Subsequently, SDFP pixels are selected based on both γ_x and $D_{\Delta,A}$ values, having a minimum $D_{\Delta,A}$ and maximum γ_x value is fixed as the threshold (Hooper 2008). The total number of SDFP candidates for sequential pair selection is ~2 times as much as the standard SBAS pair selection. Considering the final selection of SDFP pixels for the sequential approach the number has increased by ~1.2 times in comparison to the standard SBAS pair selection as illustrated in Table 3.2.

Table 3.2. Comparison of SDFP pixels statistics between StaMPS-SBAS and sequential pair selection approach.

S.No.	Description	StaMPS-SBAS	Sequential StaMPS-SBAS
1.	Initial SDFP selected candidates	60731	124467
2.	SDFP density (pixels/km ²)	1230	2520
3.	Initial gamma threshold	0.3	0.3
4.	Re-estimated gamma threshold	0.002	0.265
5.	Selected SDFP pixels	55515	66792

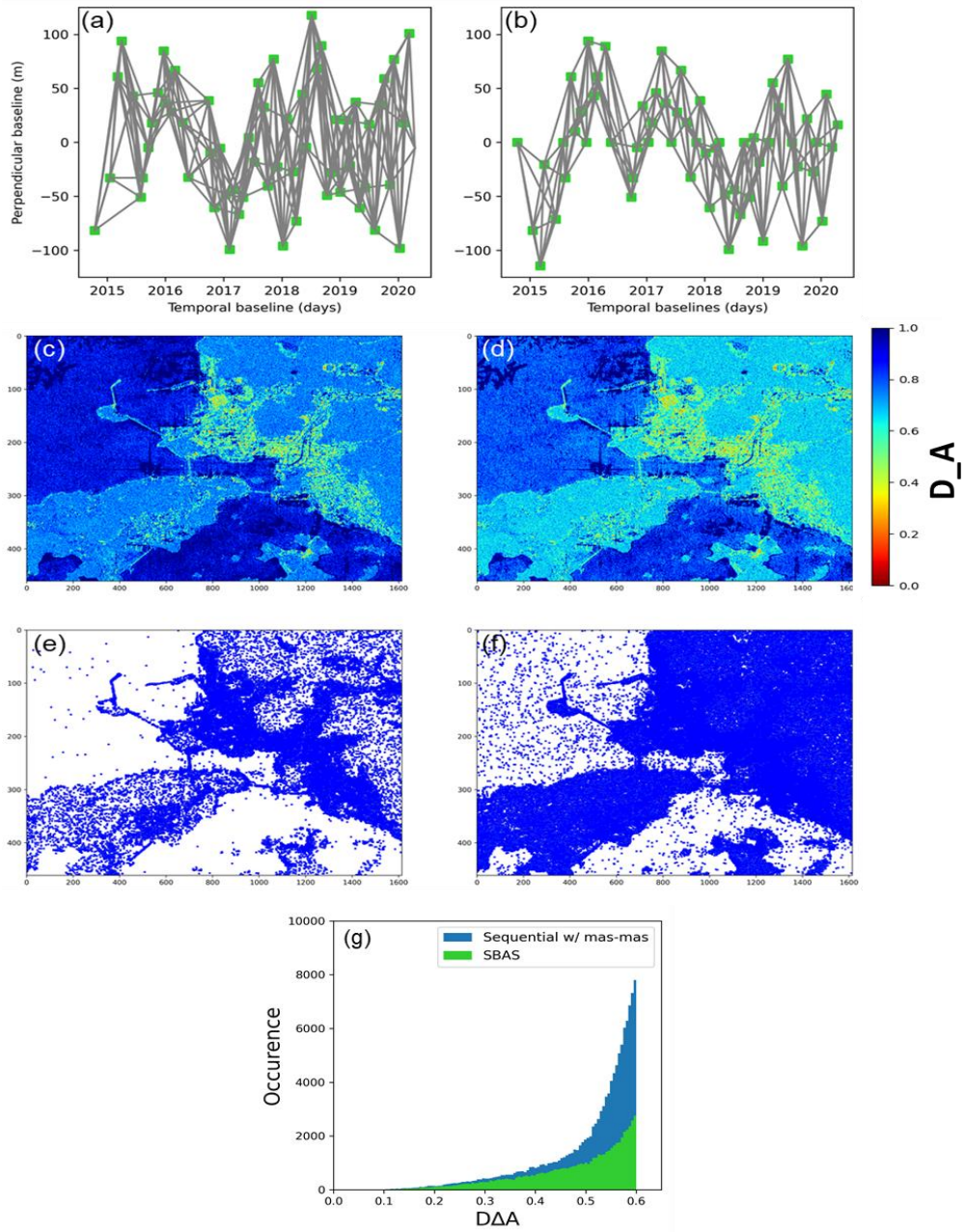


Figure 3.10 (a) and (b) plot between Perpendicular baselines and Temporal baselines for standard Stamps-SBAS and Sequential pair selection, respectively. (c) and (d) D_A estimated for standard Stamps-SBAS and sequential pair selection, respectively, (e) and (f)

the initial coherent candidates selected based on the threshold value $D_{\Delta,A} < 0.6$. (g) and (h) histograms of $D_{\Delta,A}$ for sequential and standard SBAS pair selection.

As described in Table 3.2., the sequential pair selection approach selects about 1.2 times more SDFP pixels than the standard SBAS approach. Figure 3.11. illustrates the selected SDFP pixels overlaid on the OpenStreetMap® image. It is clearly shown that both approaches detect SDFP pixels commonly in the urban regions. However, having closer look at the zoomed inset images in Figure 3.11, numerous SDFP pixels over the vegetation areas were retained in the standard SBAS approach which could be the false alarms, whereas, our approach has its capability to drop SDFP pixels over dense vegetation and increased ~ 1.2 times of SDFP pixels in the coastal areas especially along the coasts.

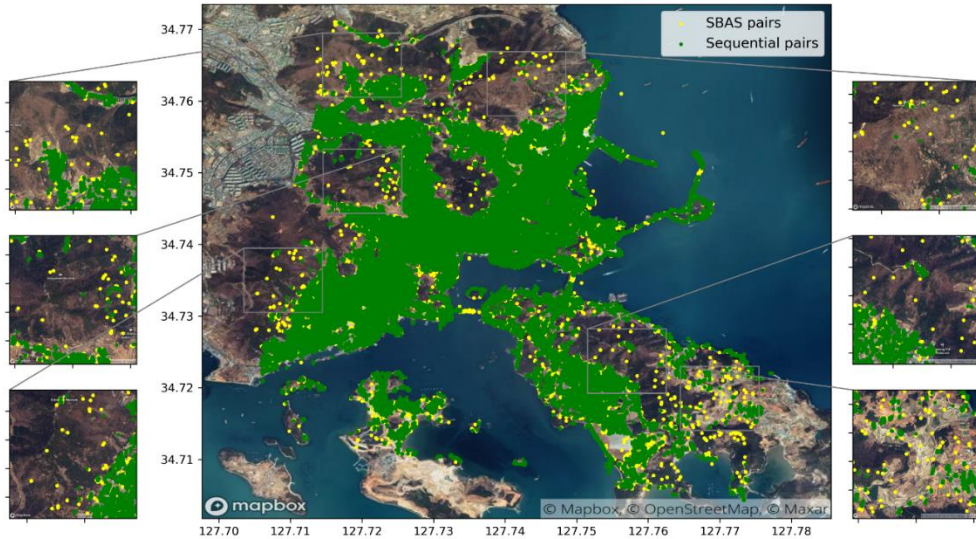


Figure 3.11. Spatial distribution of SDFP pixels obtained from SBAS pair selection and sequential pairs selection.

Lastly, the comparison of mean velocity from the experimental results was presented in Figure 3.12. In a larger view, the major deformation signals exist in both approaches. It is worth noting that the LOS displacements in the final mean velocity may comprise the considerable amount of noisy SDFP pixels in the standard StaMPS-SBAS, whereas in the sequential StaMPS-SBAS those noisy SDFP pixels were dropped in the spatially uncorrelated error estimation and phase stability analysis. Figure 3.12. shows that the time-series results derived from the sequential pair selection approach are quite consistent with standard StaMPS-SBAS. The time-series LOS displacements of pixel A which is located in the significant ground motion region (Figure 3.12c) reveal that the LOS displacements from the two approaches are consistent as well.

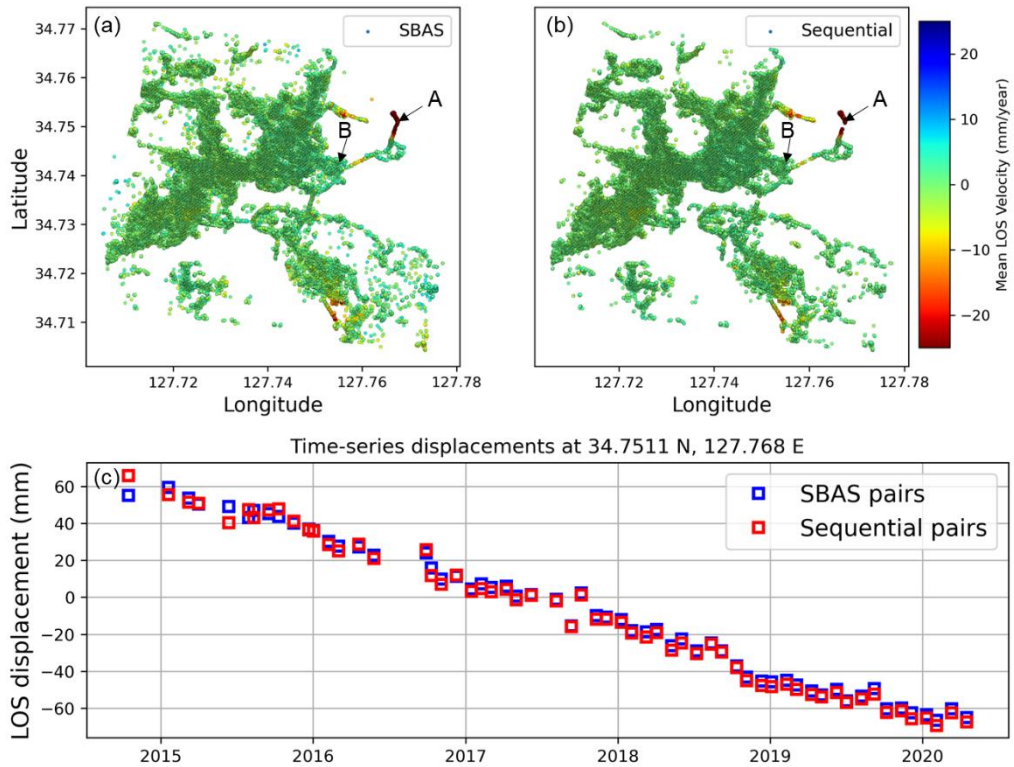


Figure 3.12. Comparison of mean LOS velocity map (descending) between (a) StaMPS-SBAS and (b) Sequential pair selection, respectively. Time-series displacements between two approaches (c) at pixel A and (d) at pixel B.

3.3.3 Vertical Land Motion of Korean Tide gauges

Based on the time-series interferometric analysis described in the previous section 3.3.2, the StaMPS-SBAS analysis was employed on the selected 10 tide gauge sites in the Korean Peninsula. The station information is listed in Table 3.3. Since this study aims to monitor the local ground motion at tide gauges and to reduce the computational time, I have only processed the ground area that covers the tide gauge station and its vicinity rather than processing the entire scene, approximately about $0.04^\circ \times 0.04^\circ$ size on the ground in the range and azimuth direction, respectively.

Table 3.3. Tide gauge stations used in the interferometric analysis.

S.No	Station name	Latitude	Longitude
1.	Pohang	36.047222	129.383889
2.	Incheon	37.451944	126.592222
3.	Jeju	33.5275	126.543056
4.	Mokpo	34.779722	126.375556
5.	Samchonpo	34.92416667	128.06972222
7.	Yeosu	34.747198	127.765873
8.	Seogwipo	33.24	126.561667
9.	Tongyeong	34.8275	128.434722
10.	Gadeokdo	35.025	128.811

The synthetic Aperture Radar SAR dataset over the Korean Peninsula is acquired by the C-band Sentinel-1 A/B satellite from November 2014 to April 2019. The acquisitions consist of 6 frames each in ascending and descending mode (70 to 100 scenes for each frame) as shown in Figure 3.13. European Space Agency's (ESA) Sentinel-1 A/B satellite has the Interferometric Wide Swath (IW) acquisition mode, also referred to as Terrain Observation with Progressive Scans (TOPS) with a 6-day revisit time. Each IW scene is comprised of three sub-swaths that cover the area in the range of 250 km and the single-look spatial resolution for this dataset is 5 m in range and 20 m in azimuth. The number of 10 tide gauge stations selected is shown in Figure 3.14 to estimate the VLM of tide gauges.

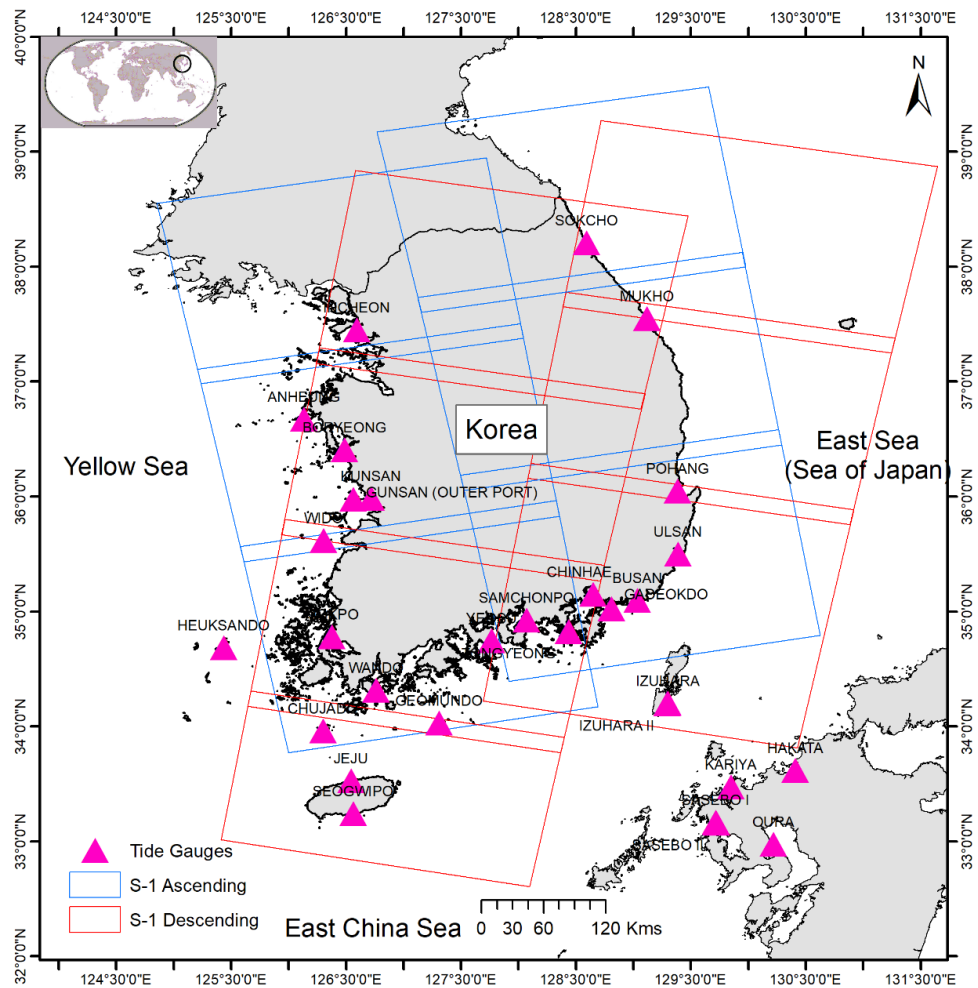


Figure 3.13 Sentinel-1 Synthetic Aperture Radar (SAR) image acquired over the tide gauges located in the Korean Peninsula.

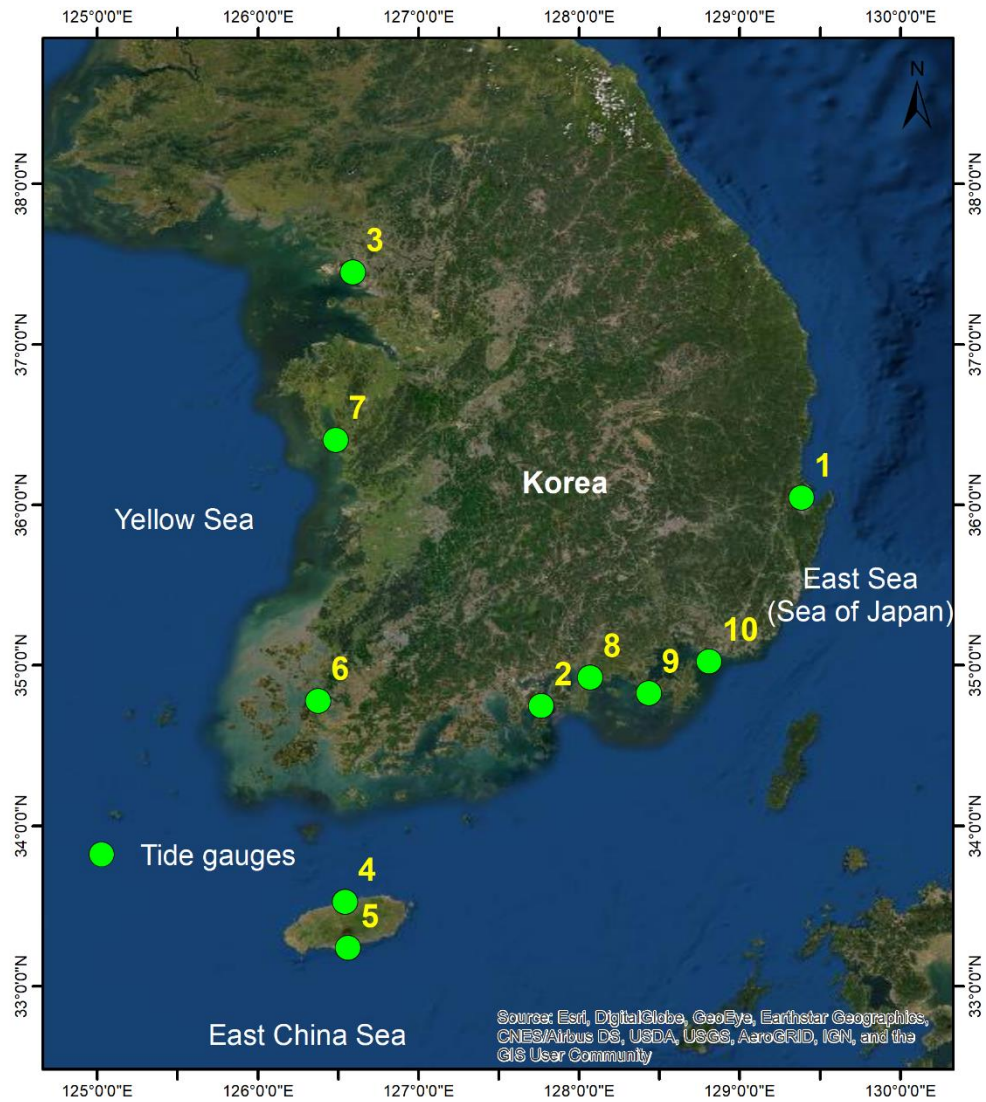


Figure 3.14. Tide gauge stations used in this interferometric analysis.

Based on the time-series interferometric analysis described in Section 3.3.1, the StaMPS-SBAS analysis is applied to the selected 10 tide gauge sites in the Korean Peninsula (Figure 3.14). The station information is listed in Table 3.3. Since this study aims to monitor the local ground motion at tide gauges and to reduce the computational time, the ground area that covers the tide gauge station and its vicinity rather than processing the entire scene, approximately about $0.04^\circ \times 0.04^\circ$ size on the ground in the range and azimuth direction was processed, respectively. The processing workflow for each station that applied in this section is summarized in Table 3.4

Table 3.4 Processing workflow of StaMPS-SBAS for vertical land motion at each tide gauge.

Step	Processing step	Product Output
1.	Acquisition of Sentinel-1 SAR data for each tide gauge station	SLCs stack for ascending and descending
2.	ISCE TOPS stack processor	Coregistered SLC stack, N
3.	Sequential pair selection (section 3.3.1)	M sequential interferograms
4.	ISCE2StaMPS	Initial SDFP candidates
5.	StaMPS time-series analysis	Mean LOS velocity and time-series displacements
6.	LOS2VH decomposition	Vertical and horizontal velocity and time-series displacements

Using Sequentially selected interferogram pairs in StaMPS-SBAS analysis, the one-dimensional (1D) mean velocity of SDFP pixels along the line-of-sight (LOS) direction for each SAR dataset was estimated. The mean LOS velocity results from ascending and descending datasets were combined to decompose the two-dimensional (2D) displacement vectors as described in Equation 3.1. The 2D decomposition results provide the vertical (upward-downward) and horizontal (east-west) components over the overlapping acquisition date ranges and spatial coverage of viewing geometries.

In this section, the results were presented by using the sequential pair selection for the StaMPS-SBAS approach. In this section, Fig 3.15 – 3.20 presents the mean vertical displacement rate of the selected tide gauge stations processed using StaMPS-SBAS with sequential interferogram pairs during the 2016-2020 SAR periods. The mean displacement rate map is superimposed on the satellite-style base map from Mapbox. Each figure has comprised of subplots shows the following results:

(a) and (b) shows the mean LOS displacement rate in the ascending and descending directions, respectively.

(c) and (d) shows the mean vertical displacement rate and mean horizontal (E-W) displacement rate, respectively.

(e-h) shows the zoomed displacement rate in ascending, descending, vertical and horizontal (E-W) geometries, respectively at the tide gauge station.

(i) shows the time-series displacements of SDFP pixels at the tide gauge location.

Sentinel-1 A/B SAR acquired from both ascending and descending track SAR data for 10 selected tide gauge, however, there is only descending track SAR data for 2 tide gauge

stations (i.e., Jeju and Seogwipo). The positive values in the mean velocity map indicate that the surface is uplifting, whereas the negative values indicate the subsidence in the vertical direction. The presented mean displacement rates map shows high-resolution InSAR derived ground motion at tide gauges and their vicinity. Since the spatial coverage of InSAR results is a small and adequate number of SAR scenes, the mean velocity maps are not affected by atmospheric noise or by orbital errors and ensure the reliability of the InSAR displacements.

The velocity maps reveal the linear displacement rates in the Pohang tide gauge station, about -19.34 mm/year, and -19.56 mm/year for ascending and descending track, respectively. On the other hand, the ground motion is quite stable in the inland areas.

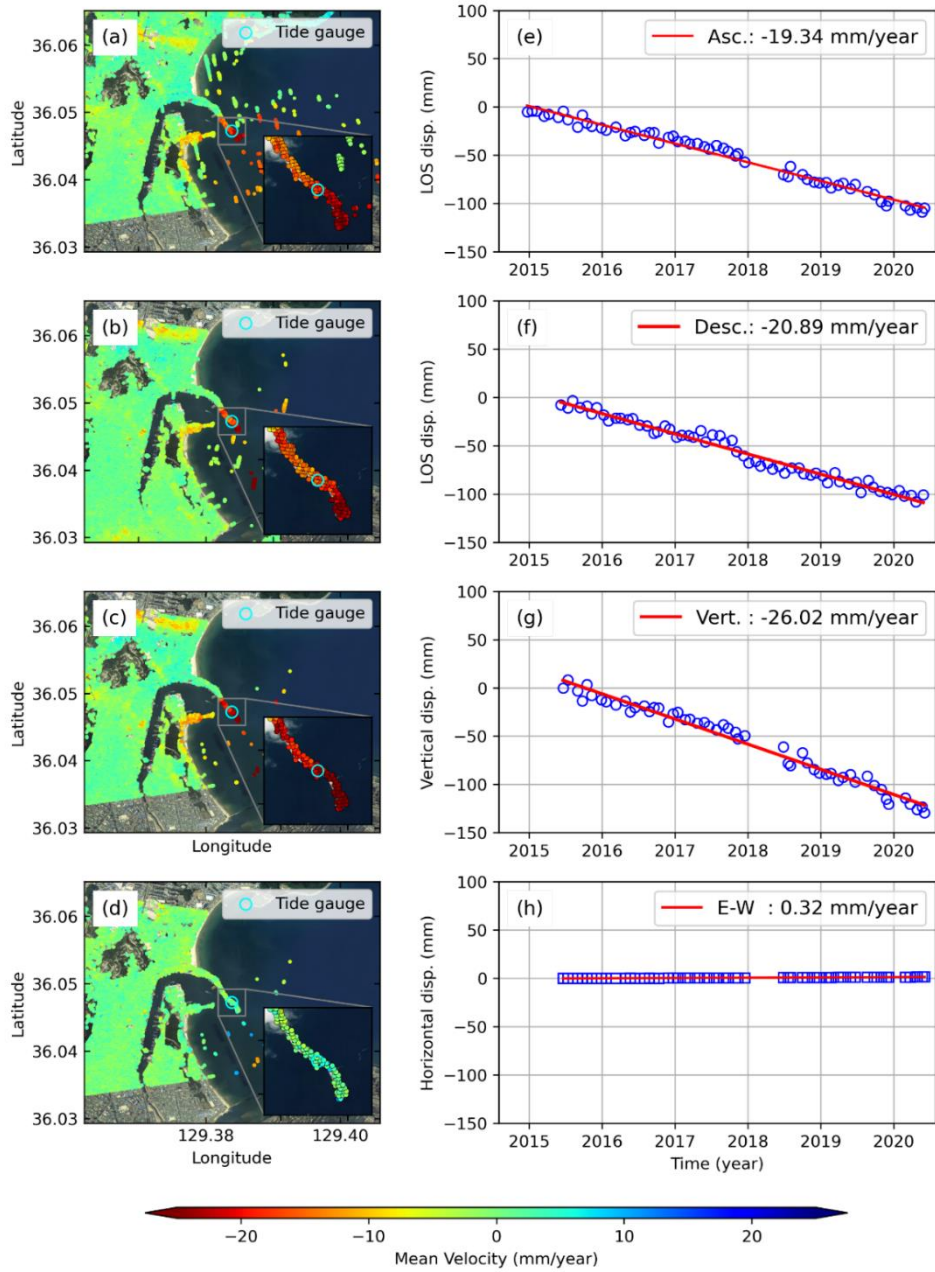


Figure 3.15. Pohang tide gauge station: (a-h) Mean InSAR velocity maps and (i) time-series displacements (grey triangle denotes ascending and grey circle denotes descending track)

The relative sea-level changes obtained over the past 30 years at the Pohang tide gauge station are illustrated in Figure 3.16(a-c). The temporal variability of sea-level rise at Pohang TG is highlighted with decadal analysis. The Pohang TG has recorded the highest sea-level change fluctuation in the Korean Peninsula. Over the 30 years, the sea level rise at Pohang TG has significantly accelerated, and more importantly in the recent decade, the sea level rise is estimated as $6.79 \text{ mm/year} \pm 1.4 \text{ mm}$ which is double the global mean sea level rise value. On the other hand, a permanent GNSS station collocated with Pohang TG is available from 2010 to 2020. Some discontinuities in the time-series observation, however, the linear velocity is observed over the observation period.

By considering, the long-term sea-level trend obtained from tide gauge records, the tide gauge exhibits significant sea-level rise since the Pohang TG was relocated to the current location in the year 2002 (<https://www.gloss-sealevel.org/sites/gloss/files/publications/documents/Korea-National-Report-2019.pdf>, last accessed on 2020/09/18). Since then, a linear increase in the sea level rise was observed therefore, KHOA applied de-trending using the leveling data observed about -2.6 cm/year (Figure 3.16b). It is worth noting that, the vertical land motion derived from our SBAS-InSAR, collocated GNSS, and leveling measurements are highly consistent with each other.

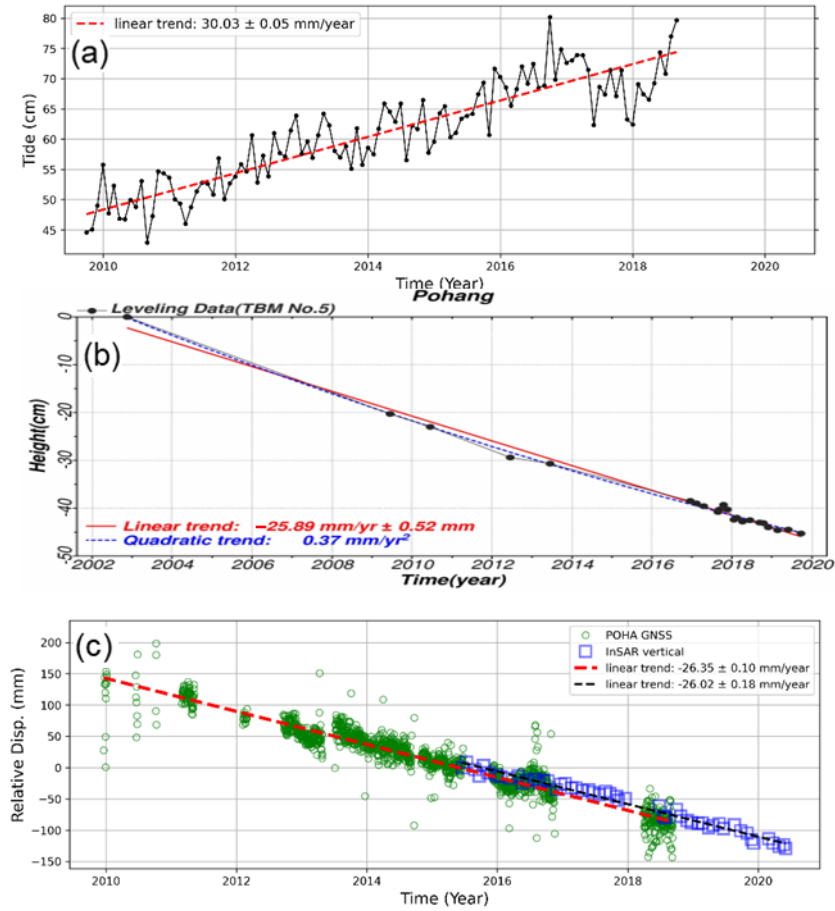


Figure 3.16. KHOA's sea-level changes observed from Pohang tide gauge for the period (a) 1989 – 2018, (b) Leveling data obtained at TBM No. 5. (c) Vertical displacement observed from InSAR and POHA GNSS station co-located with Pohang tide gauge

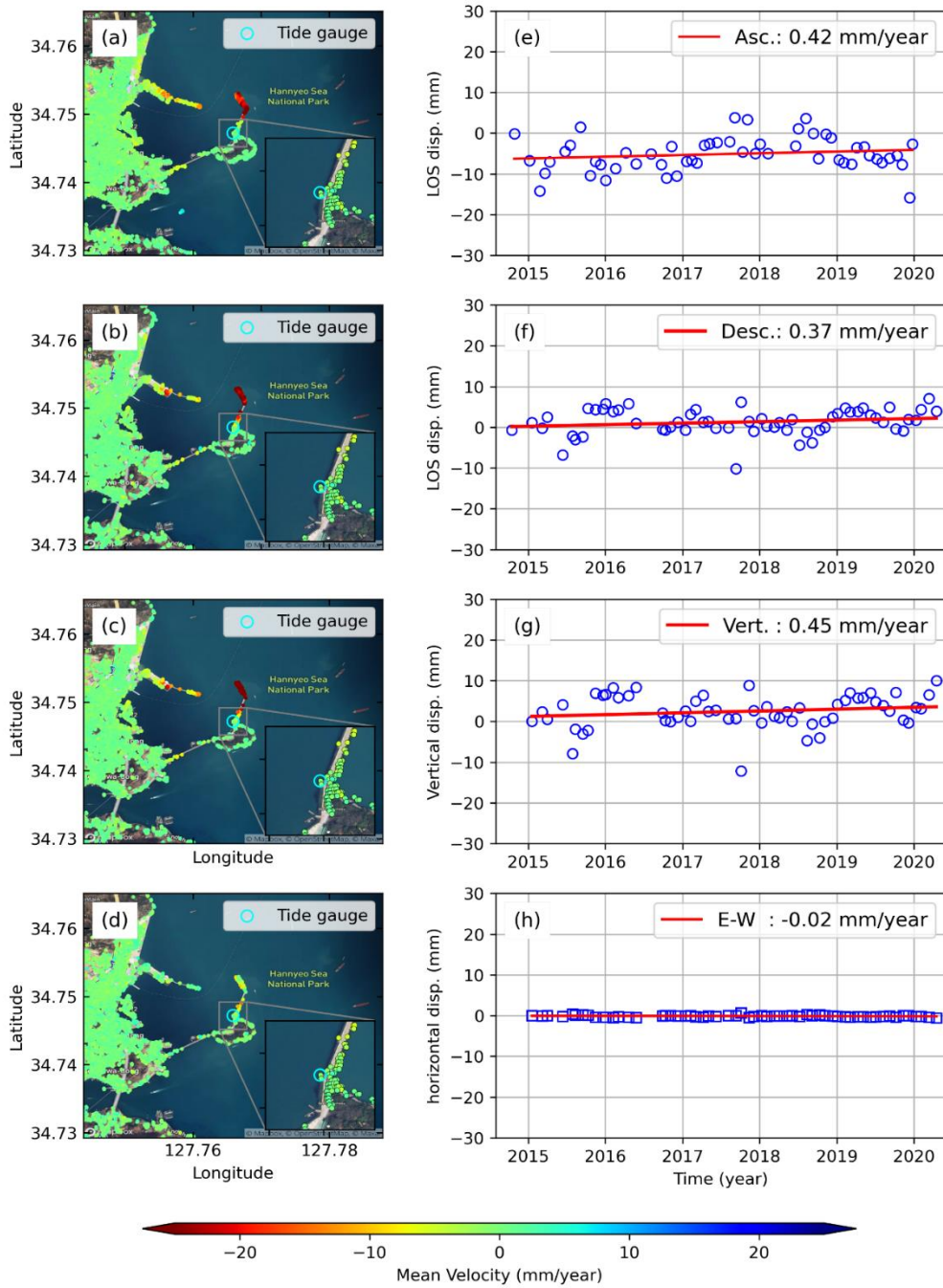


Figure 3.17. Yeosu tide gauge station: (a–d) Mean InSAR velocity maps for ascending, descending, vertical, and horizontal geometry, respectively. (e–h) time-series InSAR displacements for ascending, descending, vertical, and horizontal geometry, respectively.

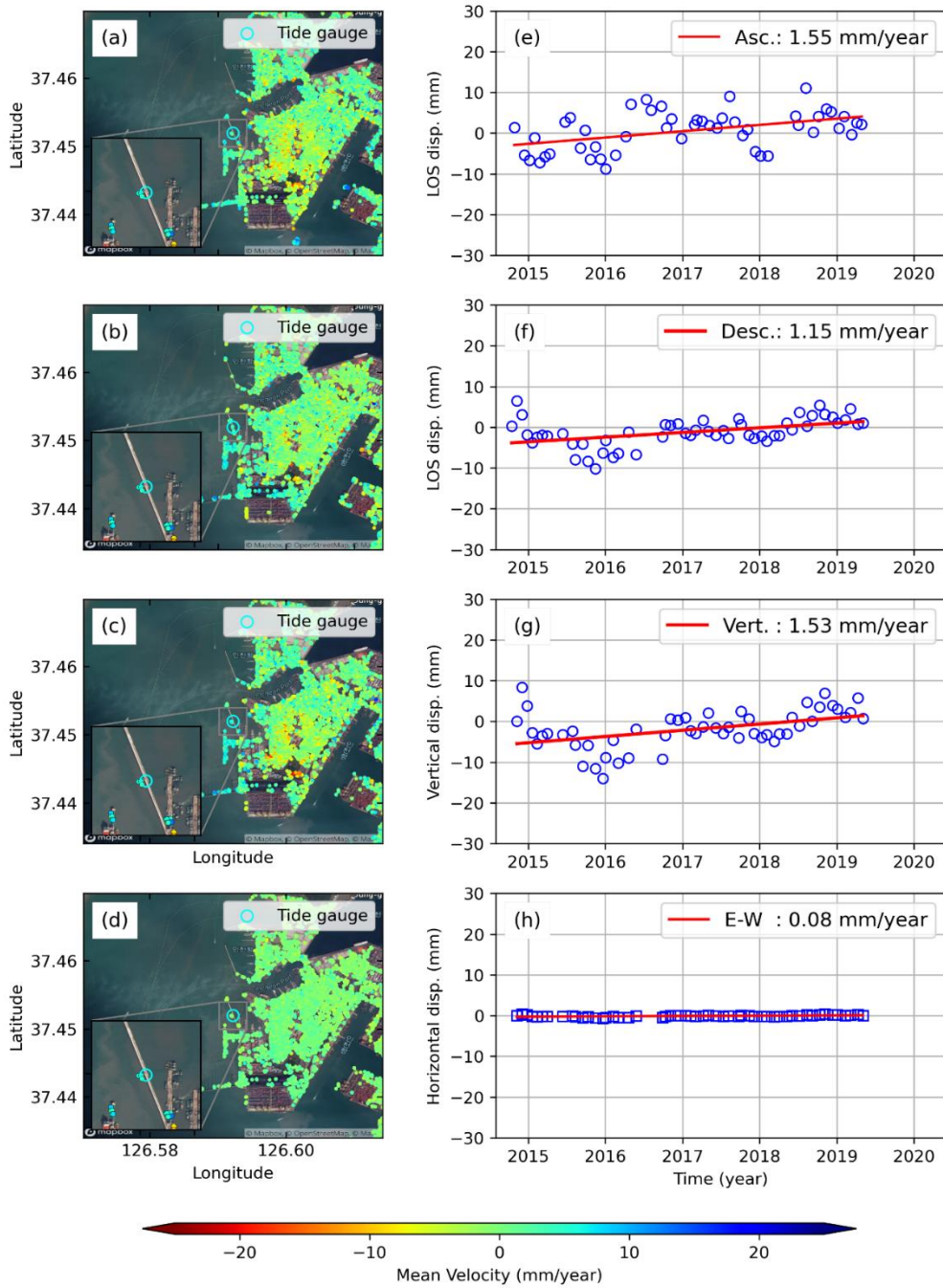


Figure 3.18. Incheon tide gauge station: (a–d) Mean InSAR velocity maps for ascending, descending, vertical, and horizontal geometry, respectively. (e–h) time-series InSAR displacements for ascending, descending, vertical, and horizontal geometry, respectively.

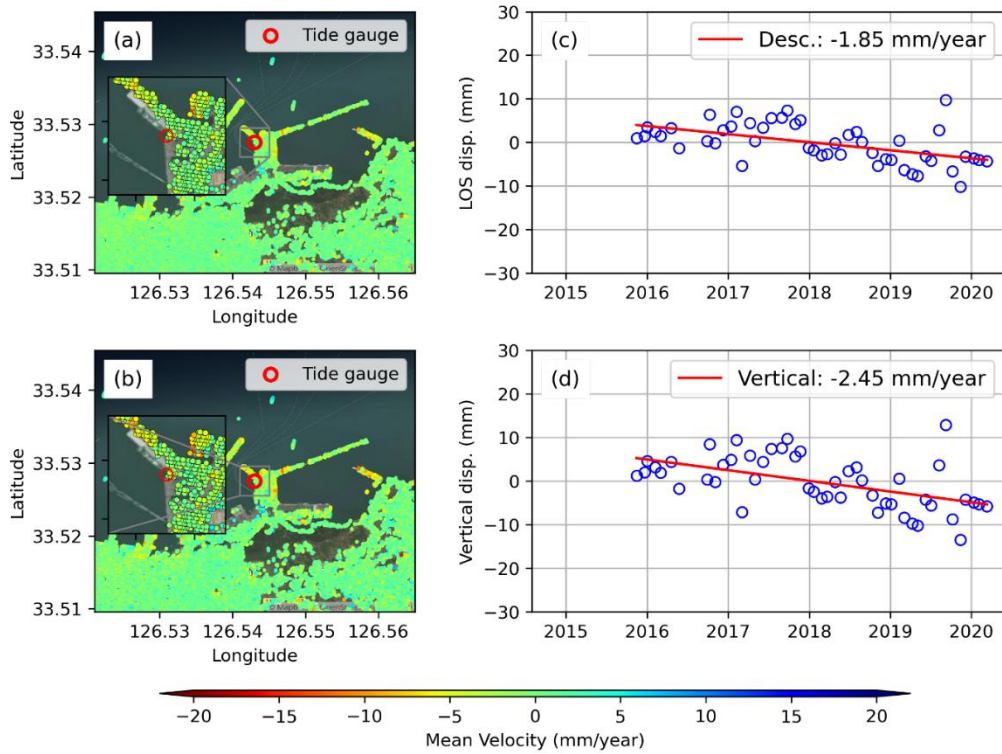


Figure 3.19. (a,b) Mean InSAR velocity maps at Jeju along descending and vertical geometry, respectively, and (c,d) time-series InSAR displacements along descending and vertical geometry, respectively.

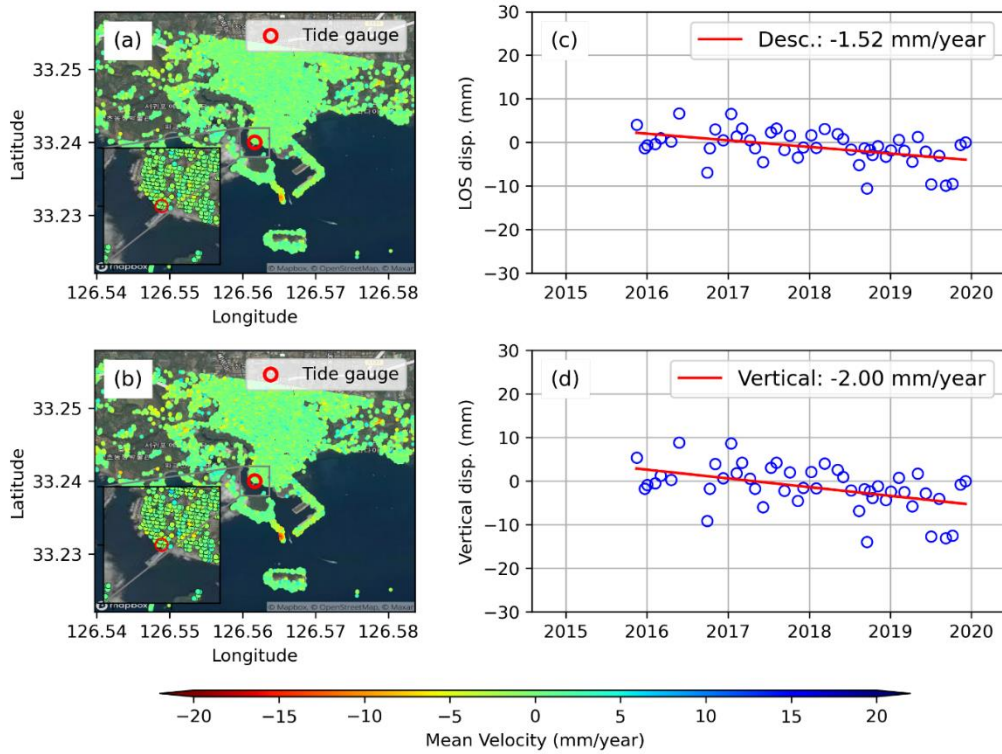


Figure 3.20. (a,b) Mean InSAR velocity maps at Seogwipo along descending and vertical geometry, respectively, and (c,d) time-series InSAR displacements along descending and vertical geometry, respectively.

3.4. Discussion

In this work, a modified approach of sequential pair selection is presented for estimating the vertical land motion of tide gauges chosen in the Korean Peninsula using StaMPS-SBAS. The experimental results demonstrate that incorporating the sequential pair selection with reference–reference interferograms minimizes the amplitude dispersion criterion and therefore it has the capability of selecting a higher number of initial coherent pixel candidates than the traditional StaMPS-SBAS approach (approx. 2 times).

The results also demonstrate the significance of time-series StaMPS-SBAS analysis for measuring VLM estimates of tide gauges in the Korean peninsula at unprecedentedly high spatial resolution. The overall vertical land motion of the selected tide gauges and their vicinity were assessed. By using the single-look and sequential interferograms, the SDFP pixel density was increased and identified at least one SDFP pixel on the tide gauges, so the vertical displacement of the SDFP pixels was believed to represent the ground motion of the tide gauges.

The InSAR processing results revealed downward VLM in the following tide gauges: (1) Pohang TG (-26.02 mm/year), (2) Seogwipo (-2.0 mm/year), (3) Jeju (-2.45 mm/year), and (4) Samchonpo TG (-3.59 mm/year); whereas there was upward VLM in tides such as (1) Incheon TG ($+1.53$ mm/year), (2) Yeosu TG ($+0.45$ mm/year), and (3) Mokpo TG ($+0.77$ mm/year). The results presented in this study address the VLM of tide gauge, primarily the recent coastal variability due to anthropogenic processes such as land reclamation (Poitevin et al. 2019), and natural processes such as sediment erosion/deposition and the uplift force on breakwater (Takahashi et al. 2014). Other contemporary studies using SAR interferometry addressed similar ground motion

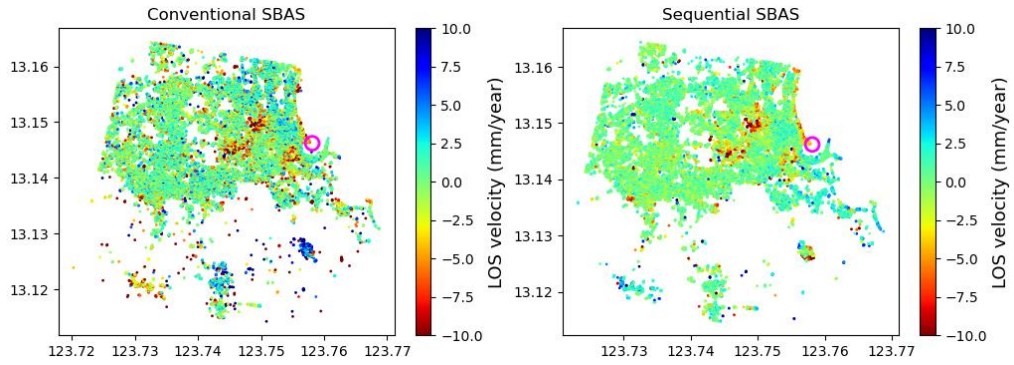
processes linked with land reclamation. Firstly, the largest VLM was observed at Pohang TG during 2015–2020, which agrees well with the co-located POHA GNSS observations and with our previous study using StaMPS PS-InSAR analysis during 2015–2018. Since the Pohang TG that is located on the breakwater that is built on the reclaimed land exhibits the continuous linear VLM, it seriously contaminates the sea-level change observation of Pohang TG. Secondly, the tide gauges located in the west on the coast of the Yellow Sea revealed upward VLM; for instance, Incheon TG showed linear VLM (Figure 3.18) that is consistent with the slow rate of sea-level change over time. This VLM is consistent with the difference between the rate of relative linear sea-level trend during 2009–2018 and the rate of global mean sea-level rise (Pörtner et al. 2019).

The tide gauges are installed along the coast and the density of coherent scatterers along the coastal areas are generally low in most of the areas and high in some of the urbanised coastal areas. i) PS-InSAR: For the areas, with high density of coherent scatterers, the single-master PS-InSAR technique is very useful. ii) StaMPS-SBAS: For the areas, with moderate density of coherent scatterers, the StaMPS-SBAS will be able to detect coherent scatterer with sufficient spatial correlation. Therefore, the estimation of mean velocity at tide gauges are also, reliable. iii) Sequential-StaMPS SBAS: However, the tide gauges that are located in the areas with poor density of coherent scatterers are affected by the spatial decorrelation. However, the conventional SBAS detects pixels near the tide gauges, due to the spatial decorrelation of initial pixel candidates, the estimation of mean velocity at tide gauges are affected by the noisy pixels. Our Sequential SBAS identifies high density of initial coherent pixel candidates, better estimation of the spatially correlated terms and eventually high temporal coherence.

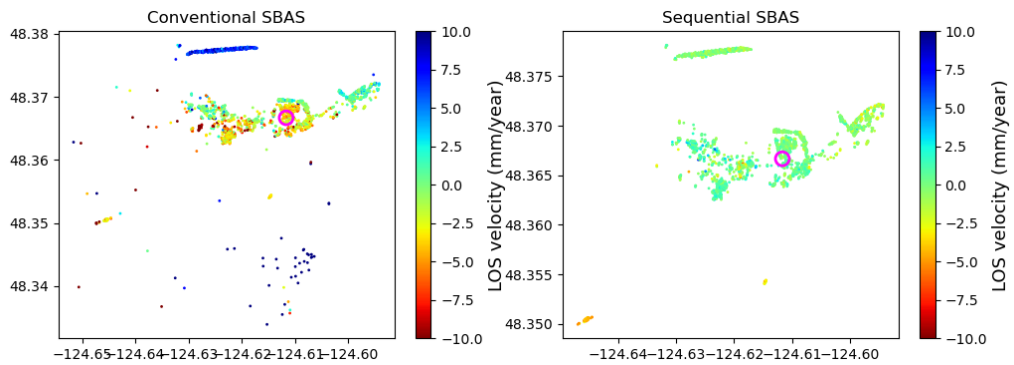
Therefore, the noisy pixels were effectively dropped and reduces the phase unwrapping errors in the coastal areas.

Following are the examples for the coastal areas with low coherent scatterers and comparison of mean velocities between the conventional StaMPS-SBAS and Sequential-SBAS approaches.

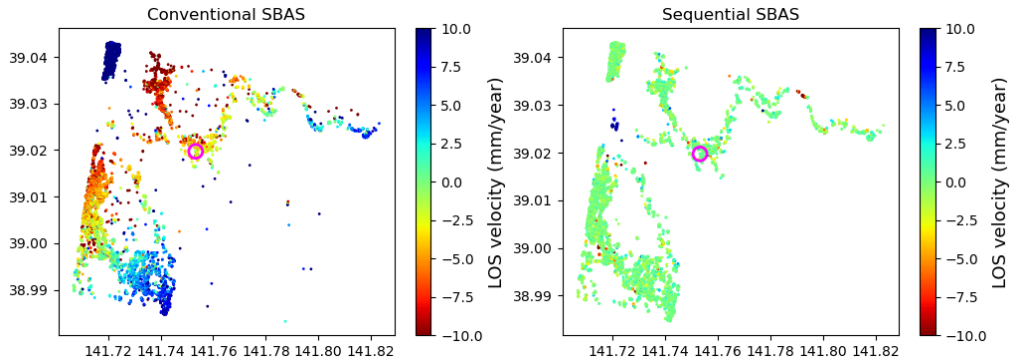
(a) Legaspi, Philippines



(b) Ofunato, Japan



(c) Neah Bay, USA



(d) USCG Freeport, USA

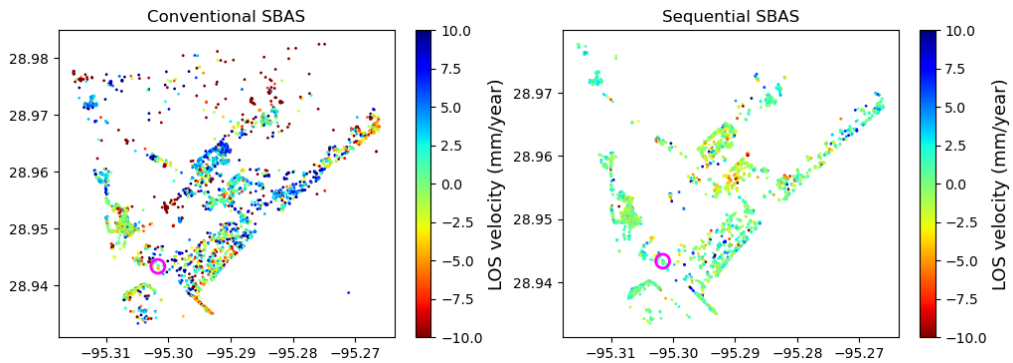


Figure 3.21. Comparison of mean LOS velocity maps between the StaMPS-SBAS and sequential-SBAS

The major limitation of this approach is when the tide gauge stations are located in areas such as dense vegetation terrain; unstable coherent targets such as containers in the port often lose the stable coherent targets, leading to phase unwrapping error. For instance, the Gadeokdo station, which is a small island with vegetation terrain; there were not enough pixels found to estimate the VLM at tide gauges. As the volume of SAR data has grown rapidly with the launch of Sentinel-1 A/B which has the quasi global coverage

over the land, further research using these sentinel-1 A/B SAR data, the proposed method could be used to reveal the VLM at tide gauges exhibiting abnormal sea level trend, and when the in-situ measurements such as GNSS and leveling measurements are not available.

Chapter 4.

Application of time-series Sequential-SBAS InSAR for Vertical Land Motion estimation at selected tide gauges around the world using Sentinel-1 SAR data

Global sea level has been rising at a rate of 3.35 ± 0.4 mm/year in the past three decades, which has significantly accelerated compared to the sea level change in the past century (1.56 ± 0.3 mm/year). Sea level rise can be a significant hazard to the low-lying coastal areas as it exacerbates coastal threats such as coastal erosion, inundation, and flooding. Global mean sea level estimates comprised of multiple components including Ice sheet melting, Glacier melting, steric and dynamic sea level change, GIA, and vertical land motion (Frederikse et al. 2020). VLM of tide gauges directly influences the relative sea level change and leads to exacerbated global sea level change. GIA-related vertical land motion can be modeled and corrected (Schumacher et al. 2018, Frederikse et al. 2020). However, the non GIA-related VLM is difficult to estimate as it ignores the land motion caused by present-day tectonic movements and local effects.

With the advent of the Sentinel-1 SAR satellite, which has quasi global coverage with an unprecedented spatial and temporal resolution, a large amount of SAR data are freely available for the novel interferometric applications. On the other hand, the tide gauges installed around the world need to be monitored to ensure the stability of the datum where the tide gauges are grounded, for reliable relative sea level changes. However, the in-situ leveling and GPS stations are insufficient to monitor the stability of the tide

gauges. Therefore, the role of Sentinel-1 SAR data plays an important role in the estimation of VLM at tide gauges around the world.

In chapter 2, the background of time-series Interferometric technique was discussed in detail, particularly Stanford Method for Persistent Scatterer (StaMPS) algorithm which allows the processing of SAR data at full resolution. In chapter 3.2, the StaMPS PSI algorithm is successfully implemented for measuring the VLM of tide gauges at Pohang tide gauge, the terrain that has sufficient number of coherent scatterers (PS pixels). As a further improvement, Chapter 3.3 presents the modified Sequential pair selection approach for StaMPS-SBAS algorithm, which uses sequential InSAR pairs (including reference – reference pairs) to identify signals from both coherent (PS) and non-coherent (DS) scatterers in the coastal environment. The estimation of VLM at tide gauges selected for the case study was successful.

In this chapter, I investigate the 100 tide gauges around the world that may exhibit the abnormal relative sea level trend. Their VLM are estimated from the Sequential SBAS approach using Sentinel-1 A/B SAR data collected during 2014/10 to 2020/12. I also present the ‘Seq-TInSAR’ framework developed to process these stations automatically for VLM at selected tide gauges.

4.1.Description of PSMSL tide gauge data

The Permanent Service for Mean Sea Level (PSMSL) is the internationally recognized global sea level database for long-term time-series sea level change information from tide gauges. The primary aim of the PSMSL database is to provide long-term sea level information from tide gauges for ocean-related studies. The PSMSL database contains monthly and annual mean values of sea level. The dataset and metadata information is provided free of charge and is made available to the international scientific community through the PSMSL website (www.psmsl.org).

The PSMSL currently holds data from 2067 stations (not all of which are currently active) that are supplied by some 200 data authorities (Holgate et al. 2012). The primary source of the data is the global set of 973 active tide gauges. The data records are separated into two categories; the first is a research quality set that is related to a set of locally defined benchmarks through time, known as revised local reference (RLR). In contrast, there are records that have no datum control, such as investigating short-term variations and seasonal cycle studies. Among the different countries, the countries including the North America, Korea, Europe, Australia, Japan are being regularly supplies the mean sea level data, however, there are still gaps in data from the Arctic and Antarctic, India, parts of South East Asia, South and Central America, and Africa (source: www.psmsl.org).

Figure 4.1 shows the distribution of all these station, both the RLR and the metric tide gauge stations. The mean record length of the RLR data is 37 years (Church and White 2006, Jevrejeva et al. 2006) and however, for analysis of long-term trends, at least 60 years of data are required (Douglas 2001).

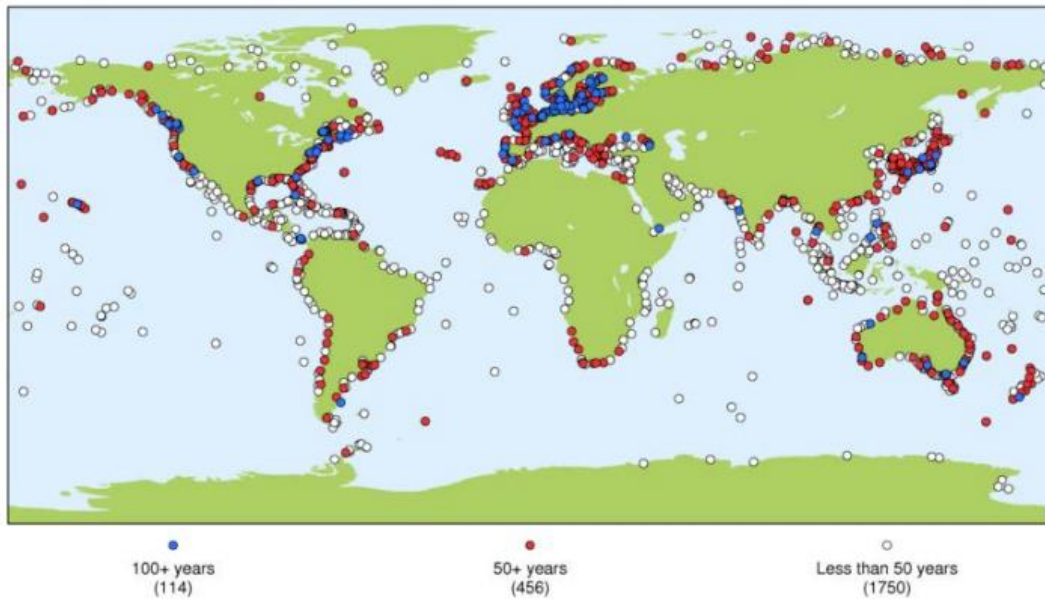


Figure 4.1 Distribution of tide gauge stations (Source: SONEL)

The monthly tide gauge records of 100 tide gauge stations selected from the Permanent Service for Mean Sea Level (PSMSL) are employed in this work (Holgate et al. 2013). In this study, the tide gauge stations were selected based on the abnormal relative sea level trends measured by tide gauges as opposed to global mean sea level trends. Relative sea level trend measured by a tide gauge is a combination of the sea level rise and local vertical land motion, which can be significantly deviated from the global sea level trend. Therefore, in this study, 100 tide gauge stations around the world that has abnormal RSL trend are selected for deriving the more precise present-day VLM, subsequently, this will help to enhance sea level reconstruction from long tide gauge records.

The relative sea level trend for the 973 tide gauge records from PSMSL, were initially computed. Among these stations 100 tide gauge stations were identified based on the following criteria:

1. Abnormal relative sea level trend with par global sea level trend
2. Tide gauge stations having long time-series sea level values
3. Vulnerable deltas from urban to semi-urban coastal areas
4. Discontinuous Sentinel-1 InSAR data availability
5. Popular stations identified as VLM affected stations from previous literature

Figure 4.2 shows the 100 tide gauge stations selected around the world and categorized into five regions namely, North America, Europe, East Asia, South Asia, and Australia & New Zealand as shown in Figure 4.3.

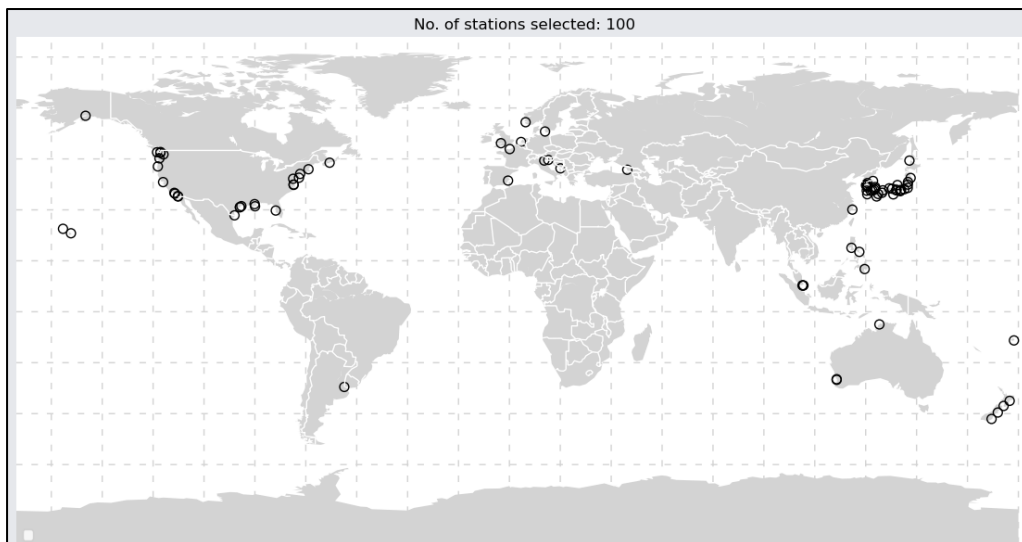


Figure 4.2 100-tide gauge stations selected for estimating VLM in this study

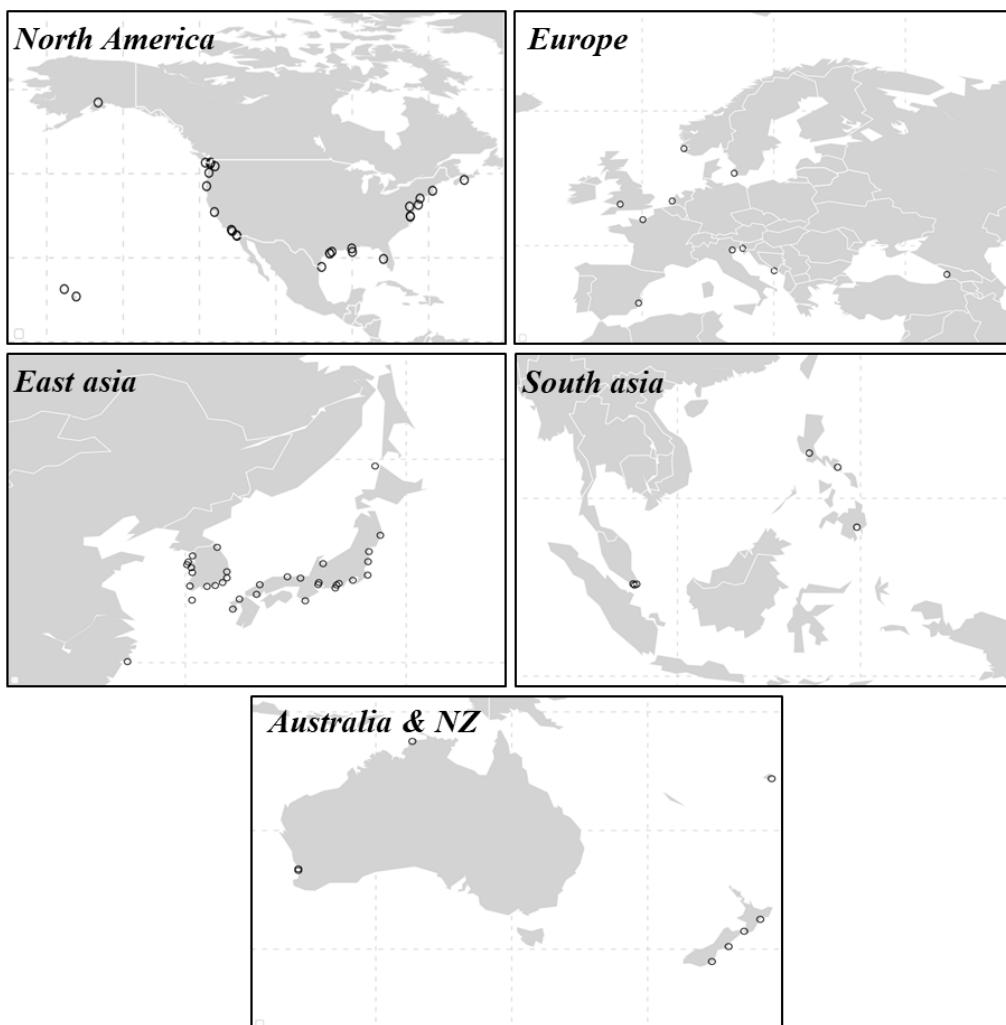


Figure 4.3. Selected tide gauges stations categorized into five regions

4.2.Sentinel-1 A/B SAR data acquisitions

The sentinel-1 A & B satellite is an Earth observation mission launched in 2014 and 2016, respectively by the European Space Agency (ESA). These satellites are 98.6° sun-synchronous orbit at 693 km altitude, operate in four acquisition modes with 6 and 12 days repeat cycle. Sentinel-1 carries a single C-band synthetic aperture radar instrument operating at a center frequency of 5.405 GHz. The right-looking instrument supports the operation in dual-polarization (HH +HV, VV+ VH).

Based on the bounding box (BBOX) information provided by the user for each tide gauge station, an area of interest (AOI) is created. As our focus is mainly on the local elevation changes of tide gauge and therefore, to reduce the computational time, an AOI of covering 10 km² centered with the tide gauge station was processed. For the calculated AOI, the application programming interface (API) query for bulk downloading was build to Alaska Satellite Facility (ASF) open access hub (<https://search.asf.alaska.edu/>) and ESA Copernicus open access API (<https://scihub.copernicus.eu/>) using the following search options listed in table 4.2 and output the search results to CSV file. The output CSV file consists description of all possible SAR datasets covering the AOI both spatially and temporally during the period 2014 ~ 2020.12. Subsequently, the Sentinel-1 dataset list is automatically reviewed and filtered to extract the suitable scenes (path and frames) that having 100 % AOI coverage, and one scene per month to reduce the computational time. Then, the filtered SAR scenes covering the entire monitoring period is between 2014.10 ~ 2020.12 are downloaded to the SLC directory. For the same scenes, the corresponding S-1 precise orbits (POEORB) files and calibration files (AUX_CAL) are downloaded from ESA.

SRTM 1 arc-second global DEM tiles are automatically downloaded from USGS open archive 9 <https://e4ftl01.cr.usgs.gov/MEASURES/SRTMGL1.003/2000.02.11/> using AOI, mosaicked, and corrected for WGS84 projection.

4.3. Automatic Time-series InSAR processing module "Seq-TInSAR"

Since, 100 tide gauges selected over different parts of the world (Hooper et al. 2012) for estimating the vertical land motion velocity and time-series, an advanced fully automatic time-series InSAR processing chain called Seq-TInSAR, is designed using InSAR Scientific Computing Environment (ISCE v2.3.3) software (Agram et al. 2013, Fattahi, Agram, and Simons 2017, Rosen et al. 2012) and StaMPS package (Hooper et al. 2012). In this section, the implementation of the Seq-TInAR fully automatic sequential StaMPS-SBAS approach is described. The seq-TInSAR processing chain is capable of processing Sentinel-1 SAR SLC data. Figure 4.4 depicts the architecture of Seq-TInSAR for generating co-registered D-InSAR products and time-series VLM products of tide gauge stations.

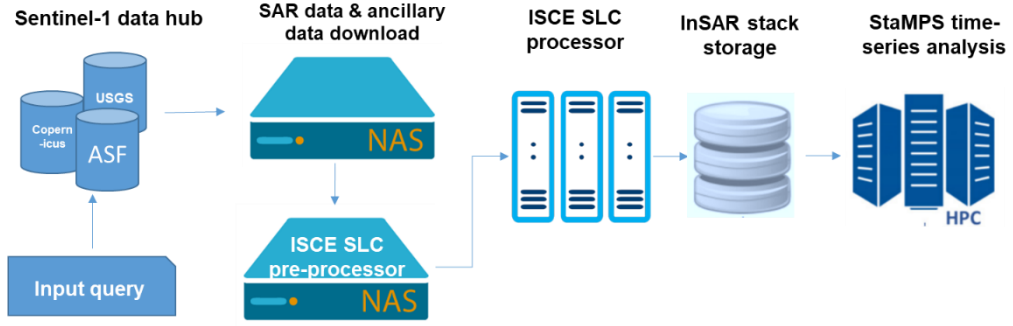


Figure 4.4. Seq-TInSAR architecture for downloading Sentinel-1 data and their time-series interferometric processing

The purpose of the Seq-TInSAR module is to unsupervised and automatically generate the VLM rate and time-series using freely available Sentinel-1 A/B SAR data. For a single tide gauge site covering $0.04^\circ \times 0.04^\circ$ area on the ground, on average 60 to 70 SAR scenes were downloaded and 300 to 350 interferograms generated (around 300 GB). The architecture depicted in Figure 4.4 for generating time-series VLM products is implemented in the python script as shown below.

isce_sl_tinsar.py -S slc_directory -D processing_directory -B 'bounding_box' -R range_looks -A azimuth_looks -P polarization -F flight_direction -M master_date -T MT-InSAR_method

The description of each arguments used in the python script 'isce_sl_tinsar.py' is described in table 4.2

Table 4.2 Input arguments for Seq-InSAR and their usage

	Input arguments	Usage
1.	-S, --slcdir	SLC directory contains sentinel-1 zip files
2.	-D, --homedir	Processing directory to store the processing output
3.	-B, --bbox	Bounding box ('SNWE 'ymin ymax xmin xmax' or xy 'x y' ")
4.	-R, --range_looks	Range looks (default: 1)
5.	-A, --azimuth_looks	Azimuth looks (default: 1)
6.	-P, --pol	Polarization (default: vv, options: vv, vh, hh)
7.	-F, --flight	Flight direction (default: desc, options: asc, desc)
8.	-M, --mas	Reference scene (yyyymmdd, default: first date)
9.	-T, --ts	Time-series InSAR method (0 [PS], 1 [SBAS], 2 [Sequential])

The Seq-TInSAR processing chain presented in this thesis consists of four levels: First, Data downloading that automatically queries and downloads Sentinel-1 SAR data, Auxiliary data, External DEM data; second, an ISCE2 based SLC processor; third, a StaMPS based multi-temporal InSAR (MT-InSAR) processor and finally, post-processing including visualization.

Table 4.3 Selected StaMPS parameters used within the Seq-TInSAR processing module

S.No.	Parameter	Seq-TInSAR
1	ADD threshold	0.6
2	gamma_max_iterations	3
3	gamma_change_convergence	0.005
4	max_topo_err	15 m
5	weed_neighbours	'n'
6	merge_resample_size	50 m
7	filter_grid_size	50 m
8	unwrap_grid_size	50 m
9	drop_ifg_index	reference-reference ifgs
10	unwrap_method	3D
11	ps_mean_v	'do'
12	unwrap_gold_alpha	0.8

The end-to-end fully automatic processing of time-series sequential SBAS as described in Figure 4.4 generates the VLM maps and time-series VLM trend for the selected tide gauge site. The StaMPS sequential SBAS analysis outputs the mean velocity and time-series along the LOS direction. The output LOS ground motion estimates d_{LOS} were recomputed to the vertical land motion d_{vert} using Equation 4.1.

$$d_{vert} = \frac{d_{LOS}}{\cos \theta_{inc}} \dots \dots \dots (4.1)$$

Where, $\cos \theta_{inc}$ is the LOS incidence angle of the reference scene.

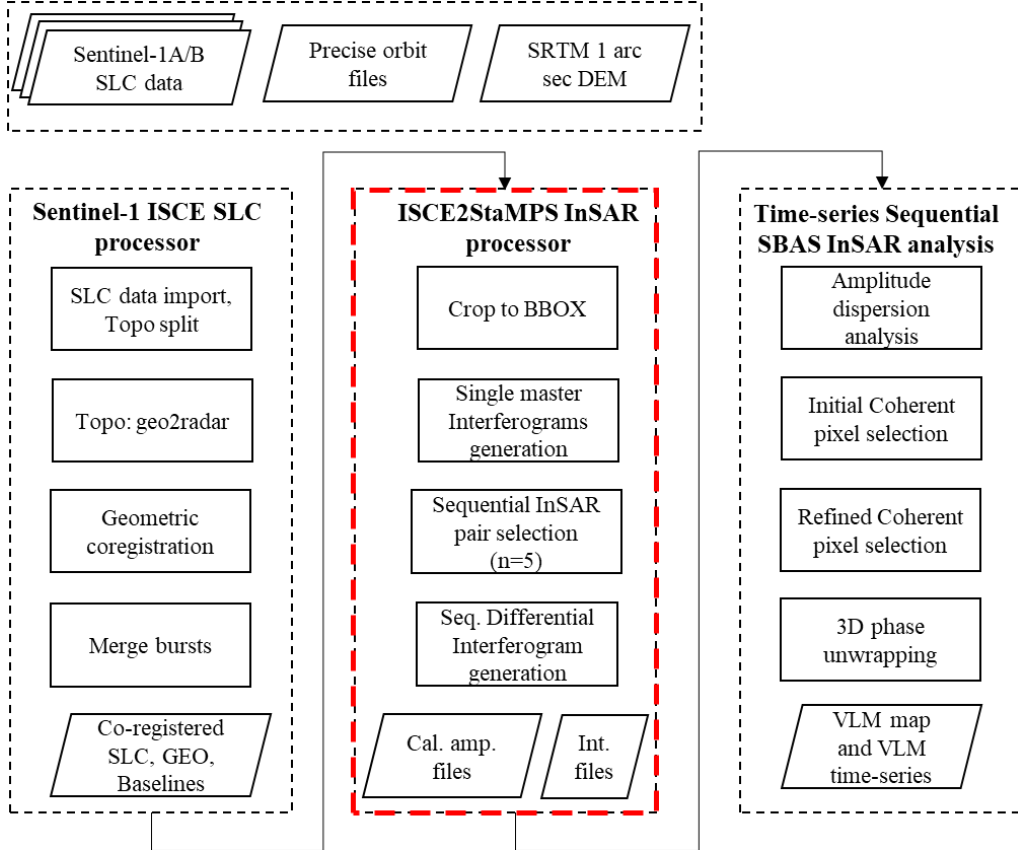


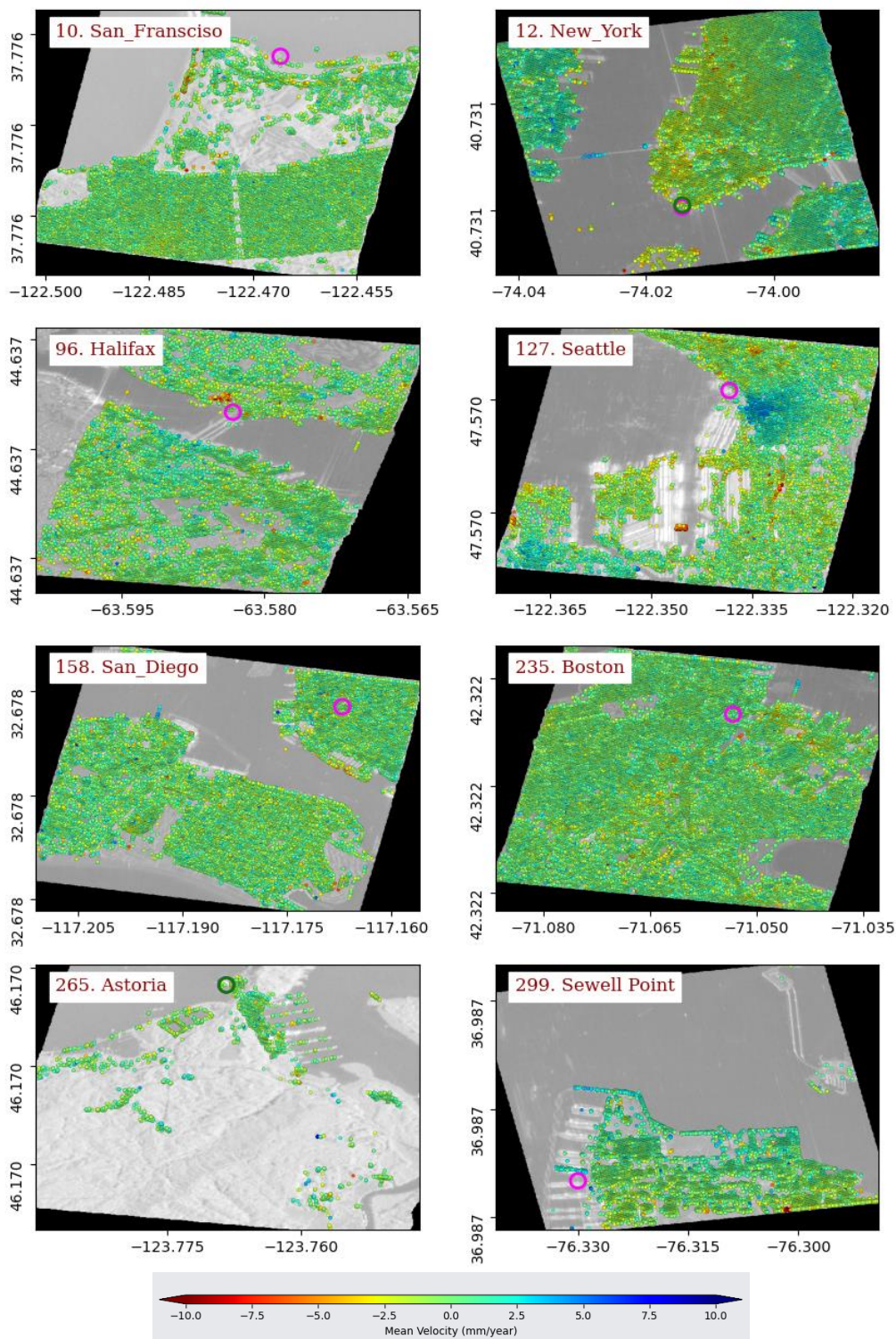
Figure 4.5. The workflow of the proposed Seq-TInSAR module used in this study

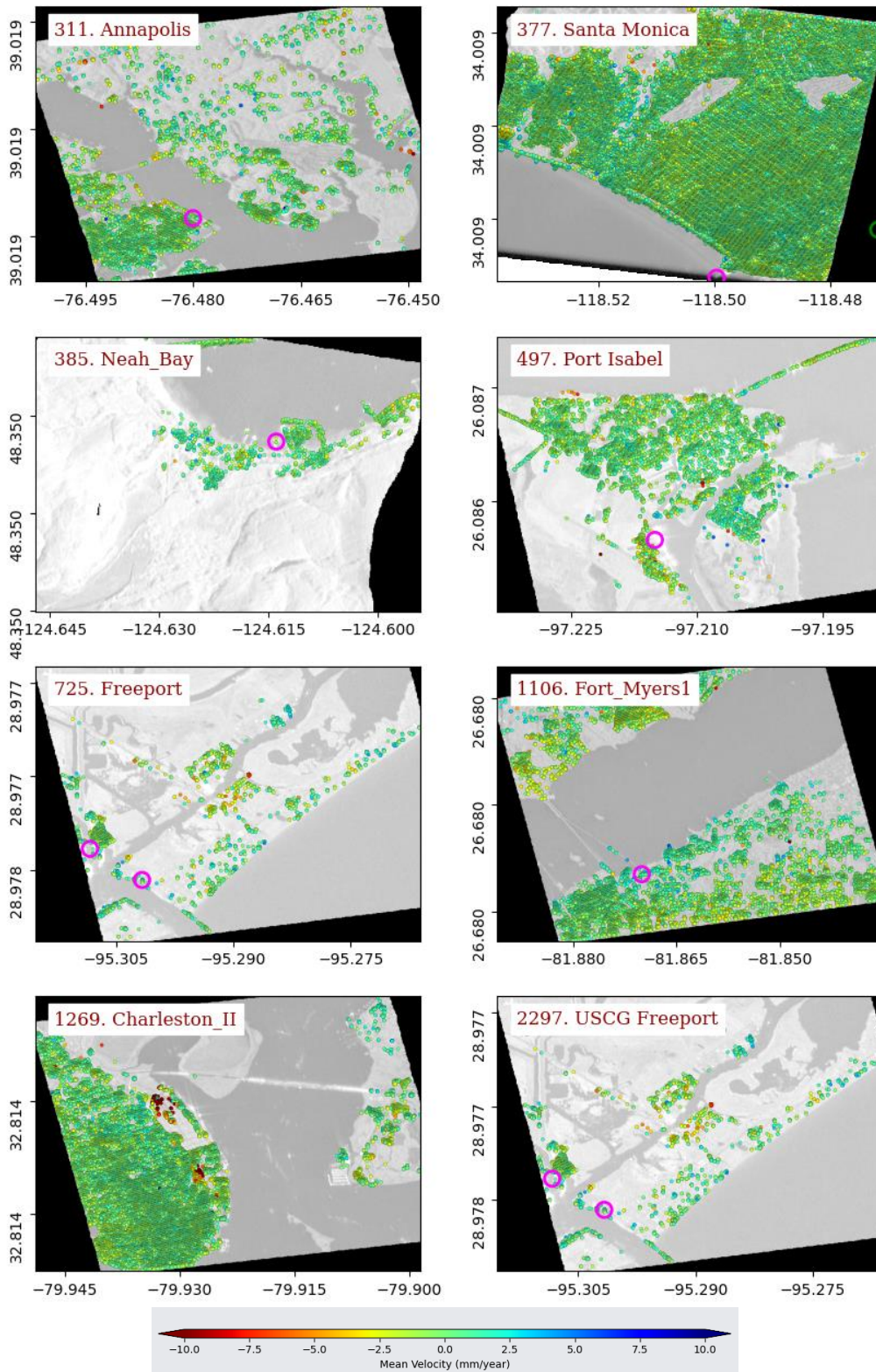
4.4.Results: Estimation of vertical land motions at selected tide gauges

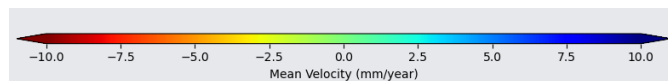
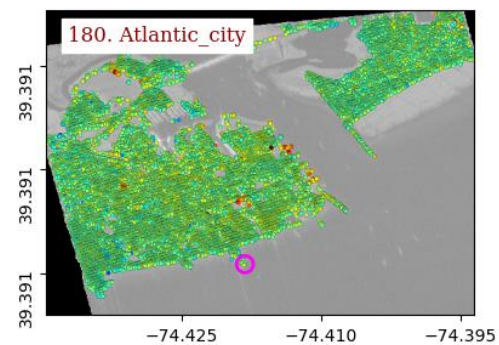
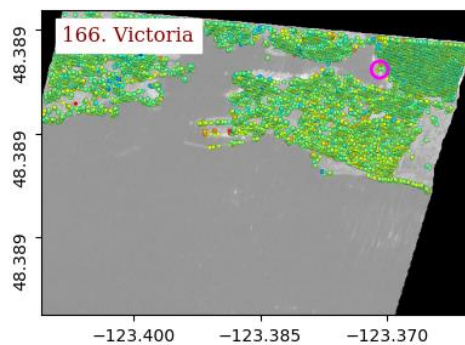
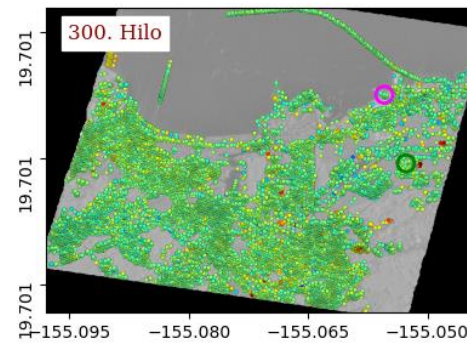
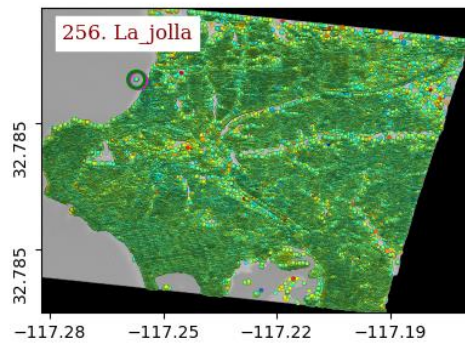
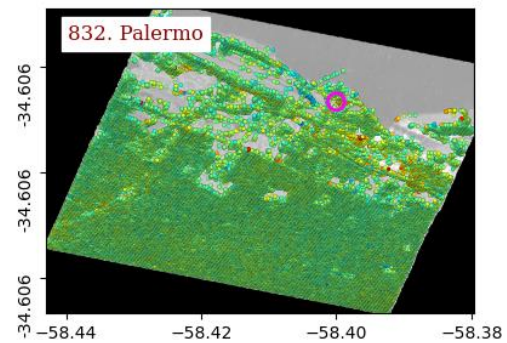
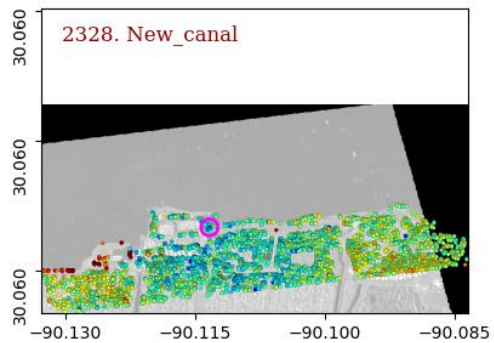
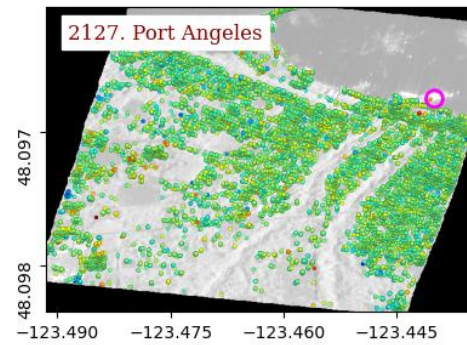
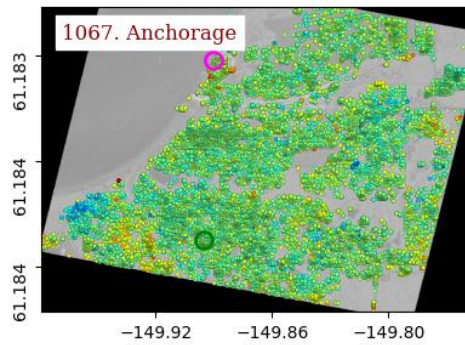
The mean VLM velocity maps generated by Seq-TInSAR module as described in Figure 4.5 for the tide gauge stations selected on the five regions are presented in this section.

The noisy pixels in the VLM velocity maps are filtered out by thresholding the standard deviation value of mean velocity.

North America







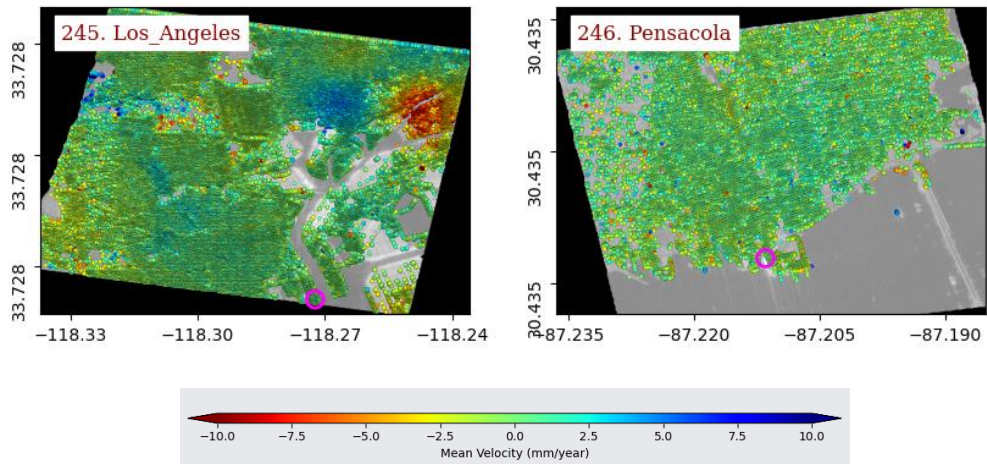
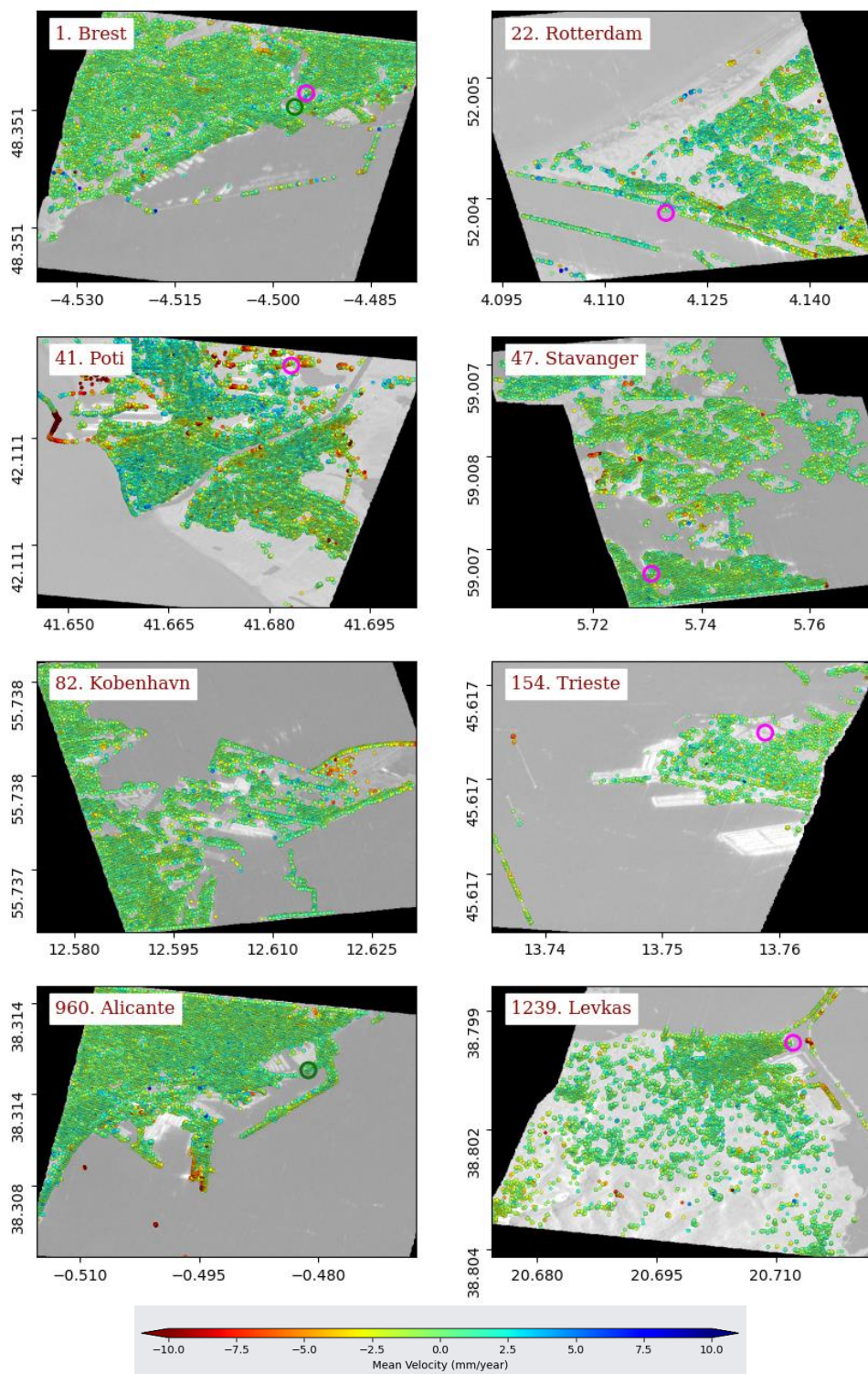


Figure 4.6. Mean VLM rate at tide gauges in the North America region

Europe



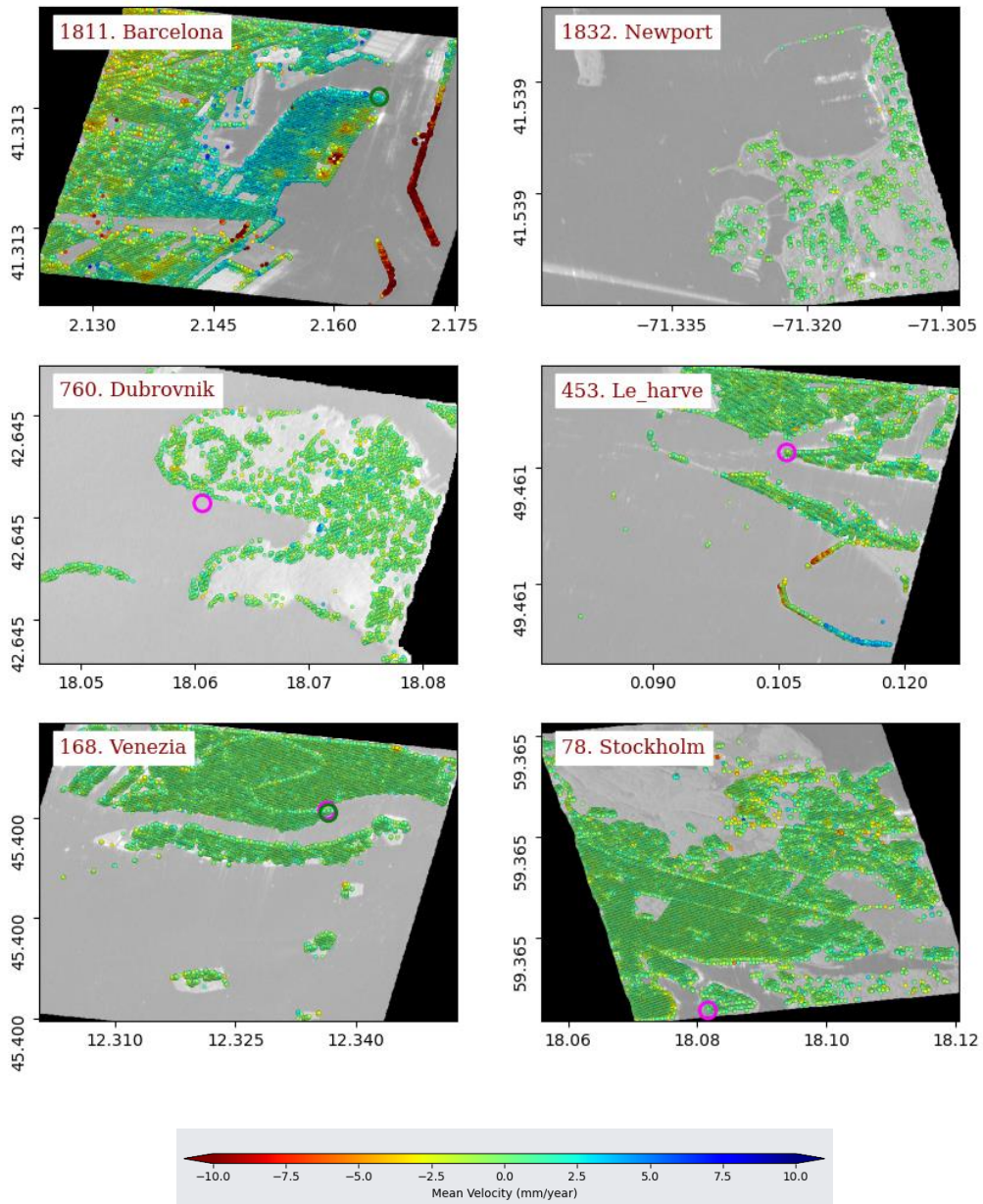
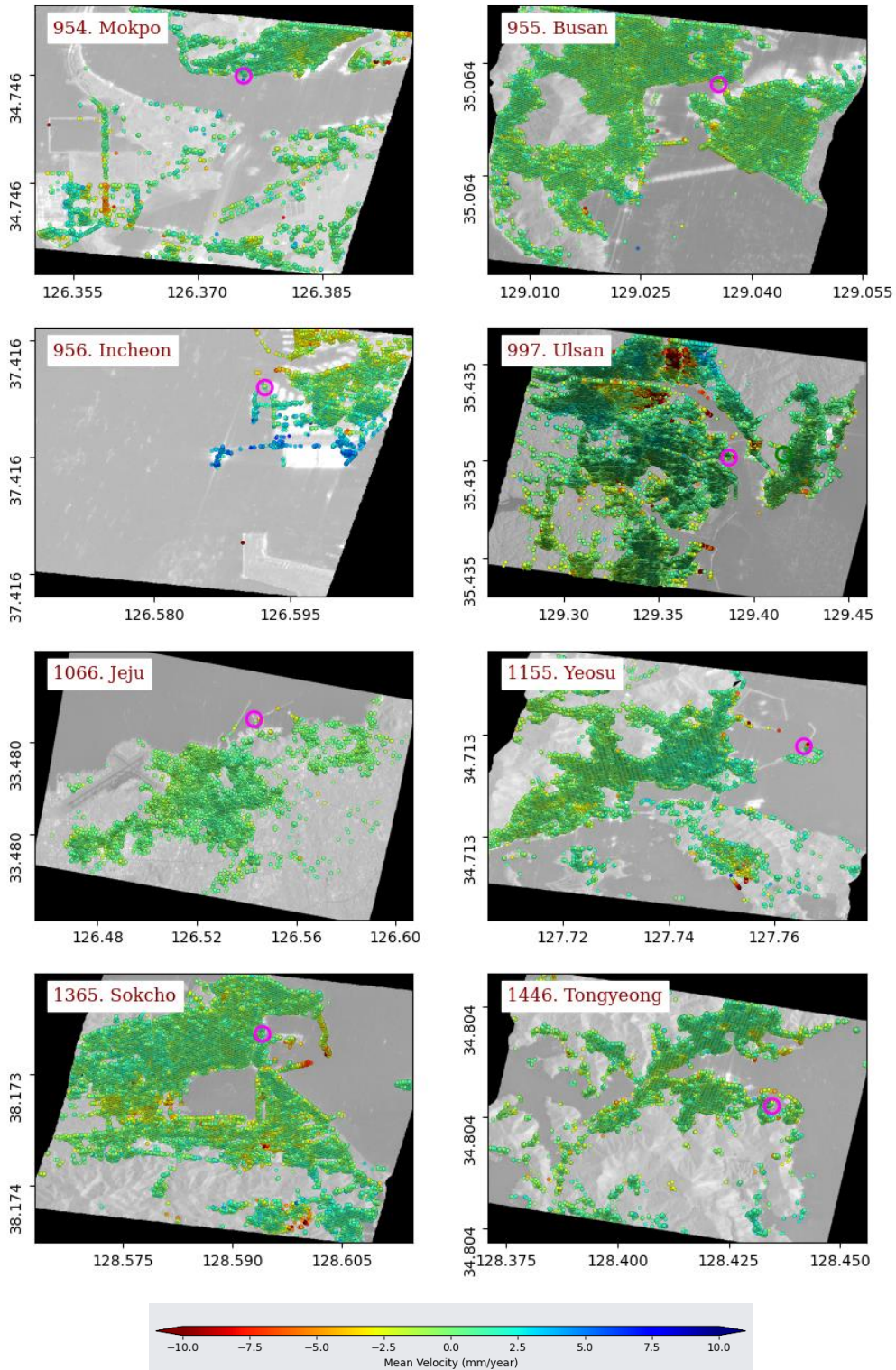


Figure 4.7 Mean VLM rate (mm/year) for tide gauges in the Europe region

Korea



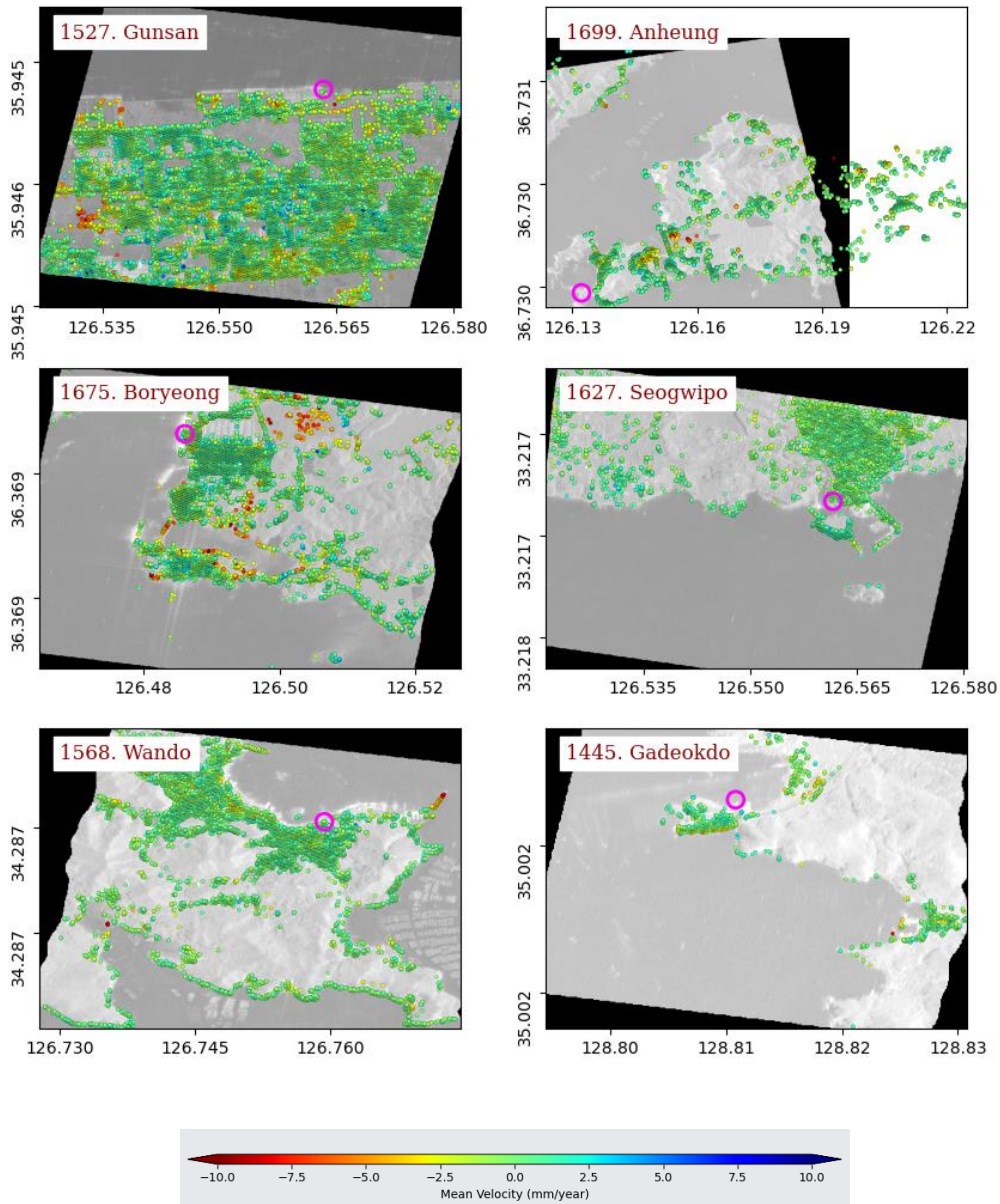
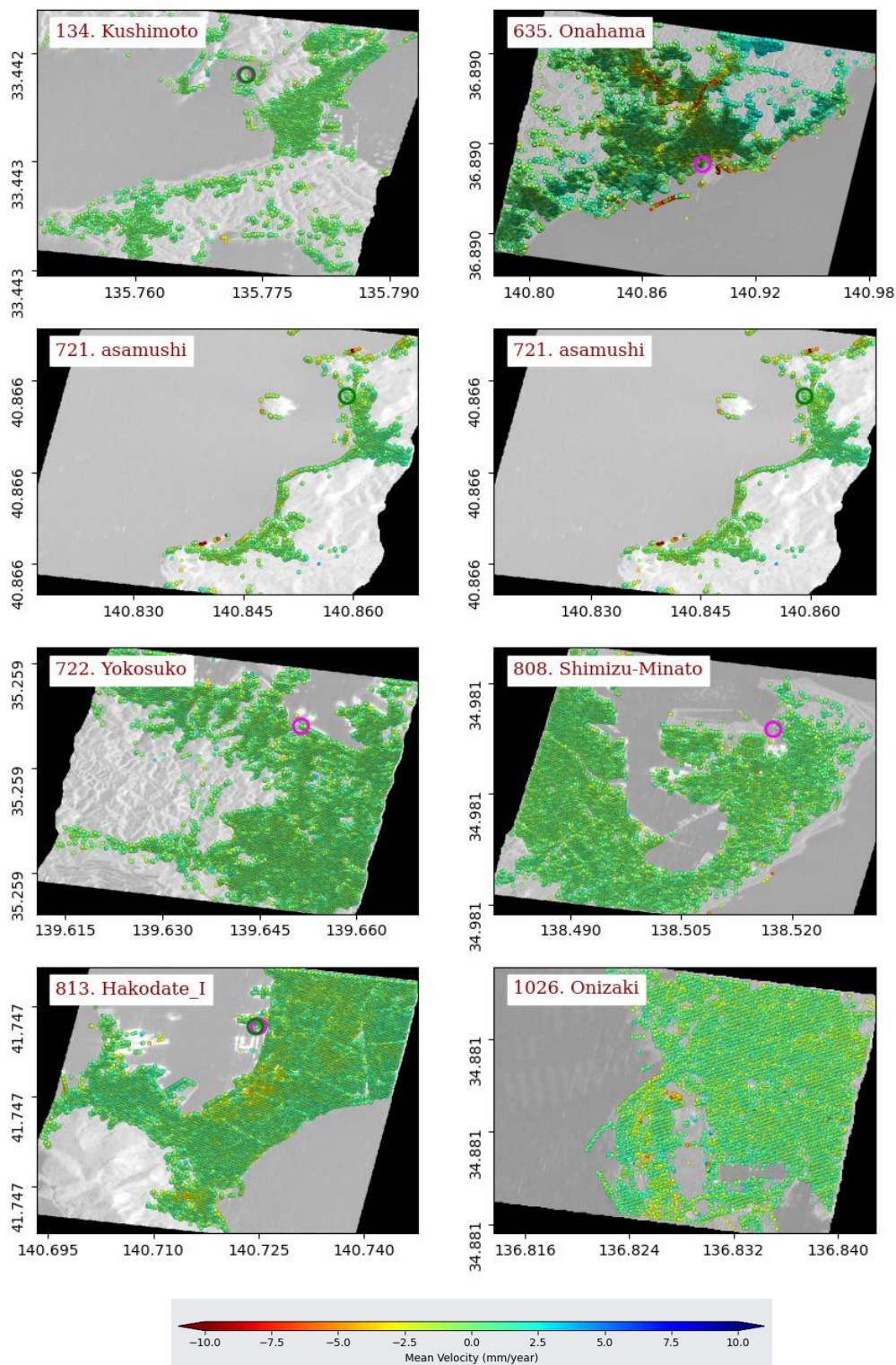
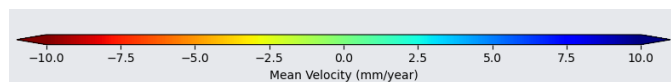
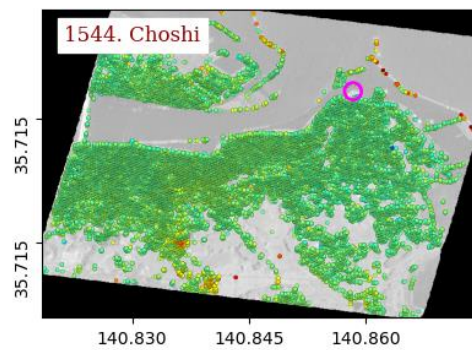
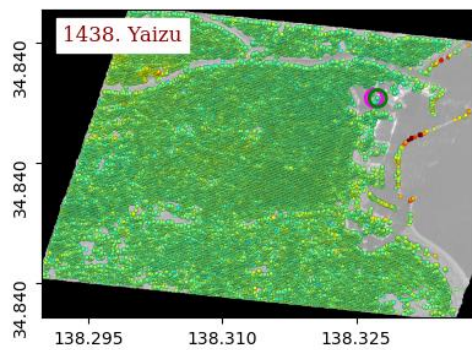
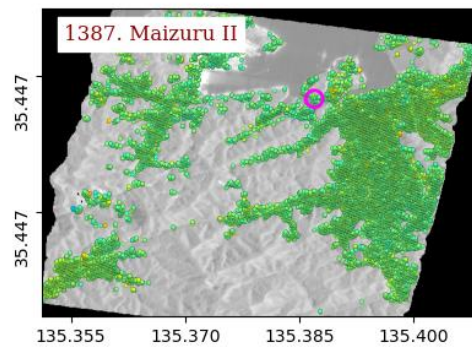
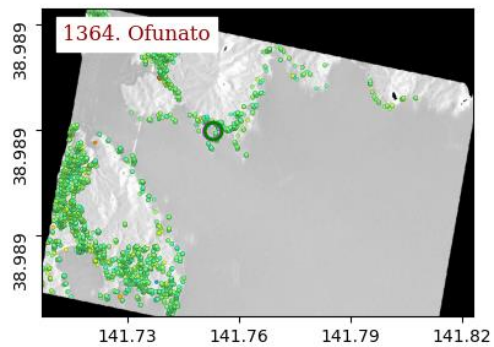
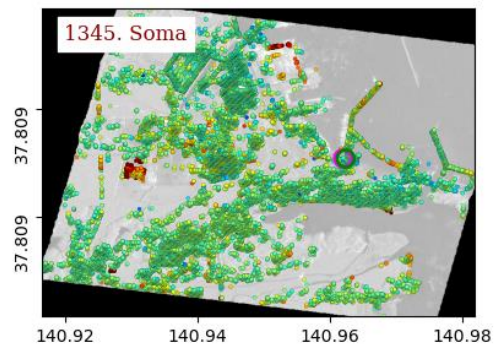
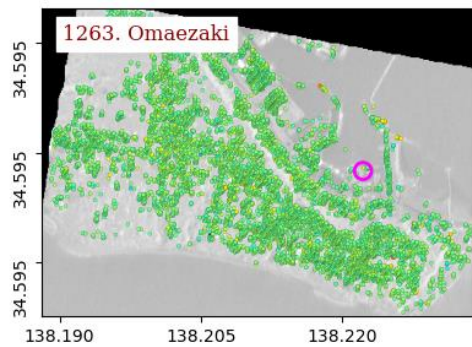
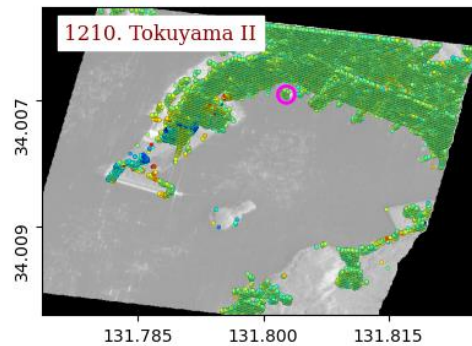
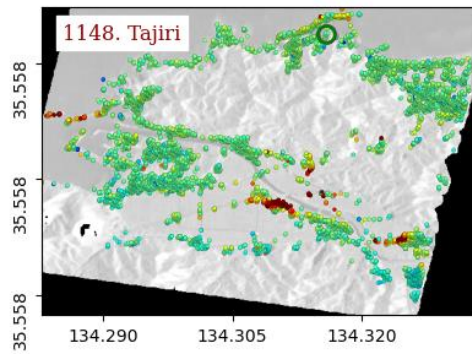


Figure 4.8. Mean VLM rate (mm/year) at tide gauges in the Korea region

Japan





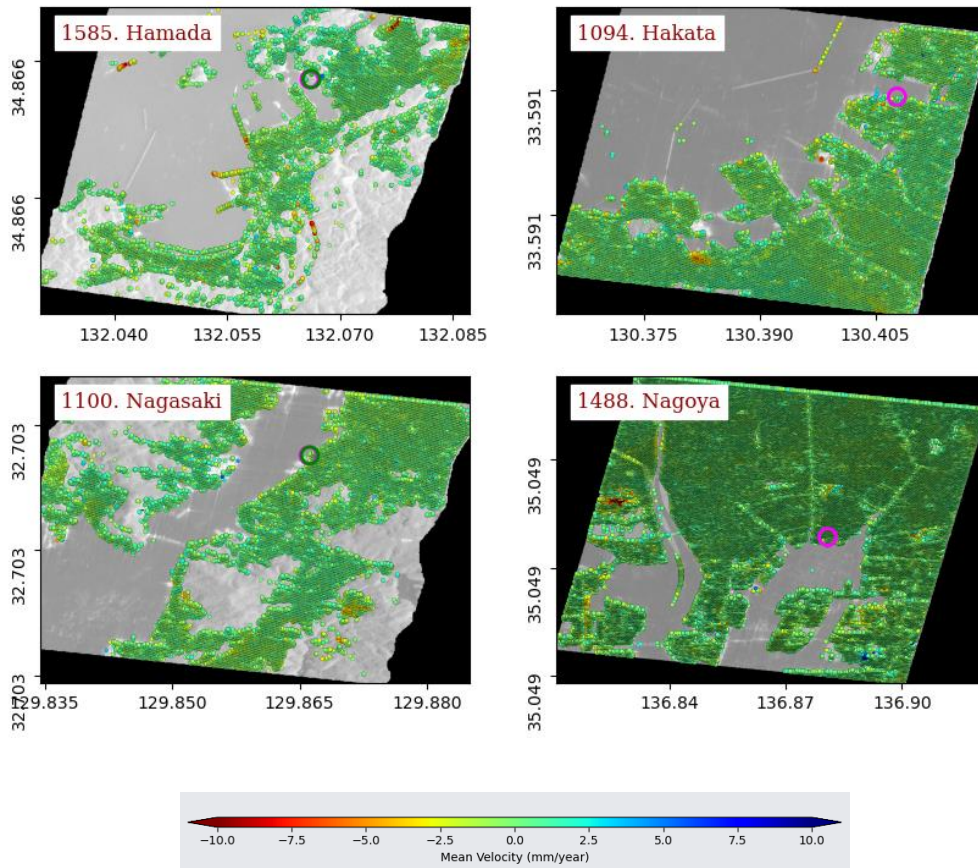


Figure 4.9. Mean VLM rate (mm/year) at tide gauges in the Japan region

South Asia

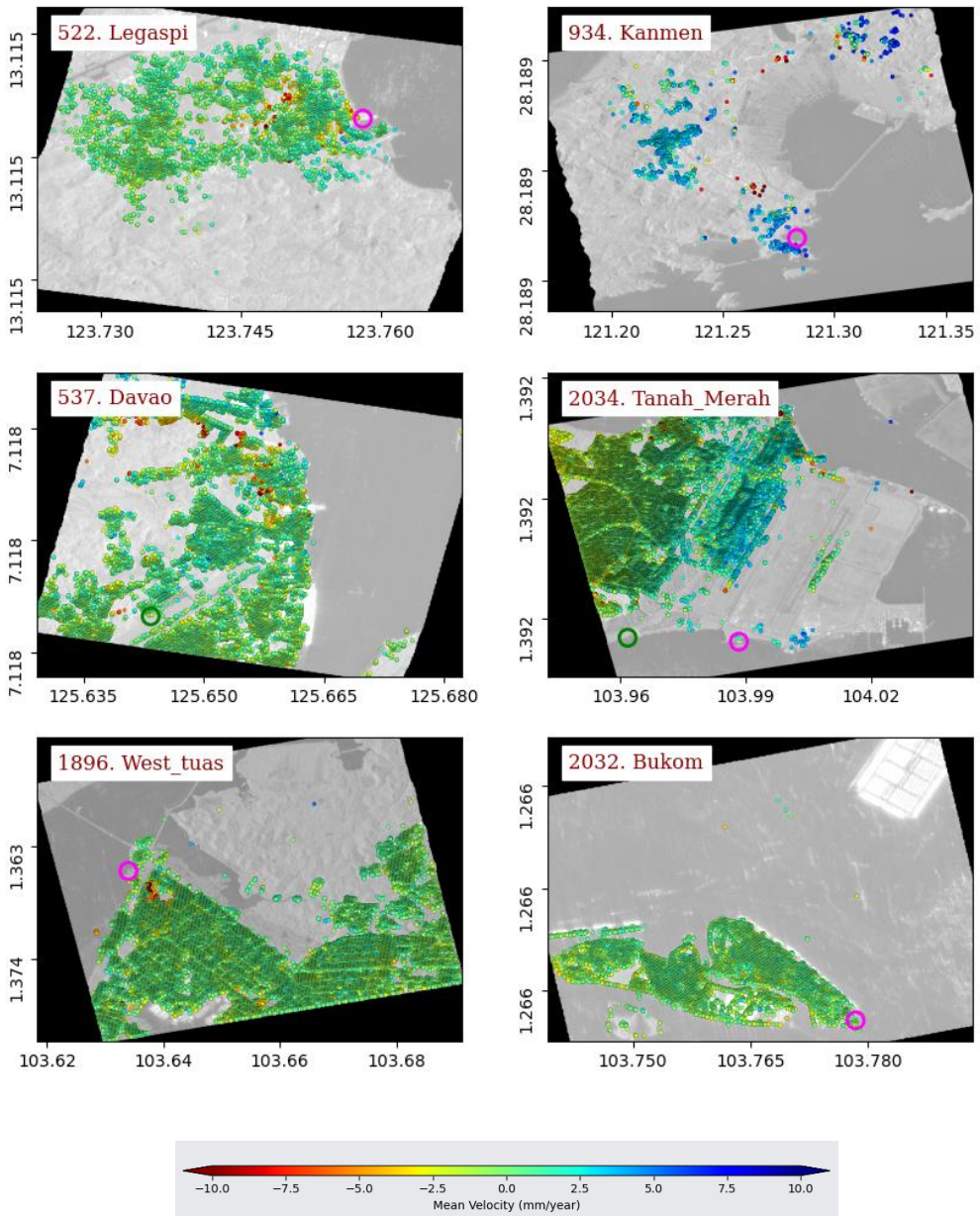


Figure 4.10. Mean VLM rate (mm/year) at tide gauges in the South Asia region

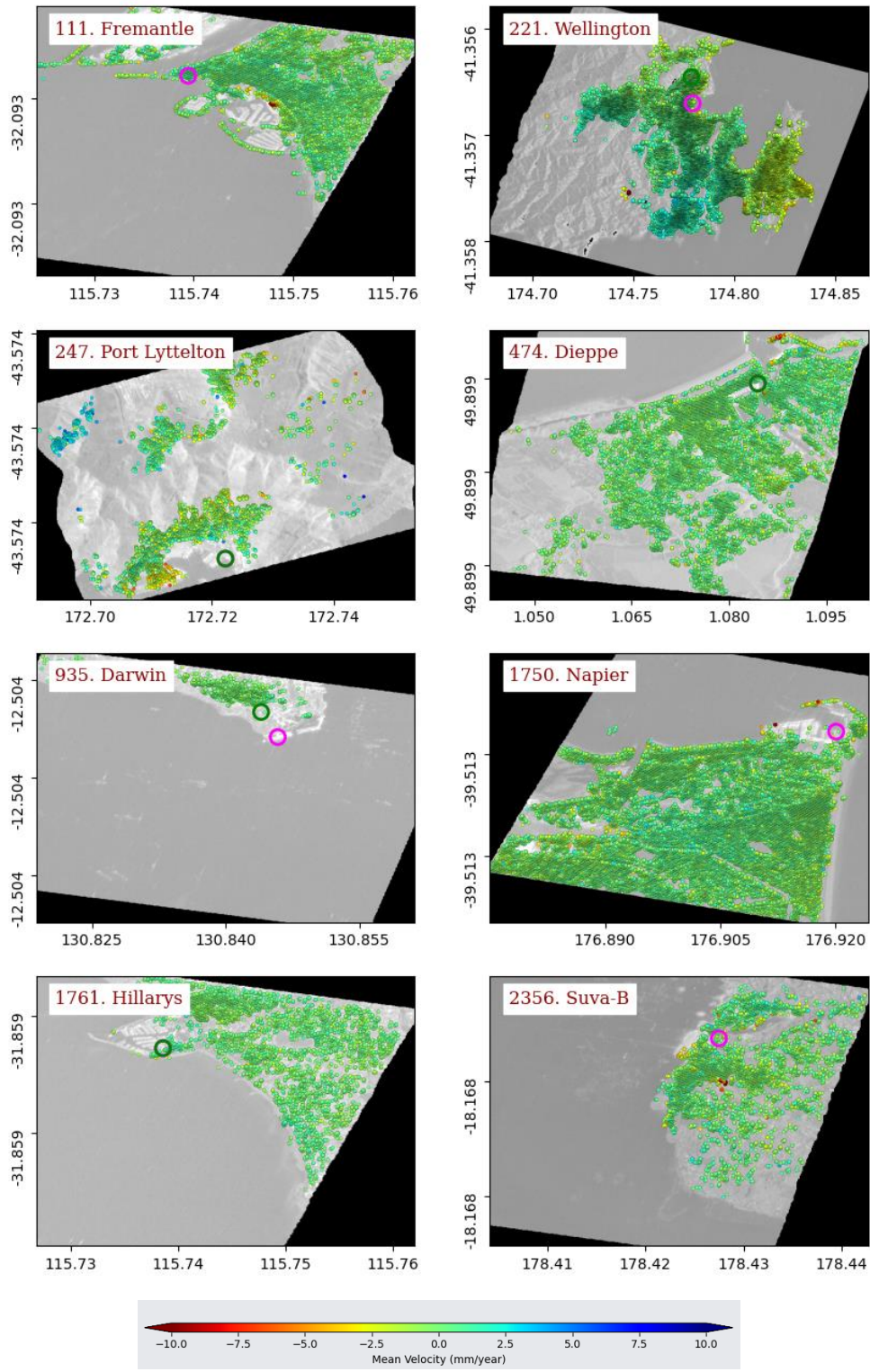
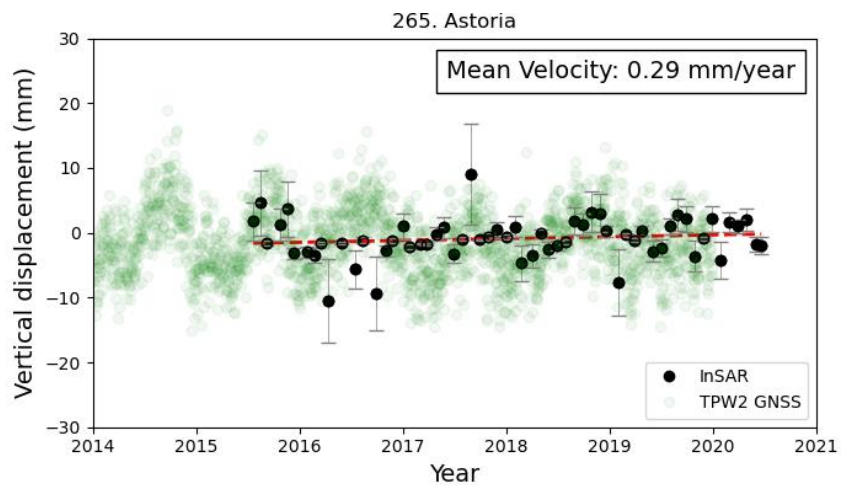
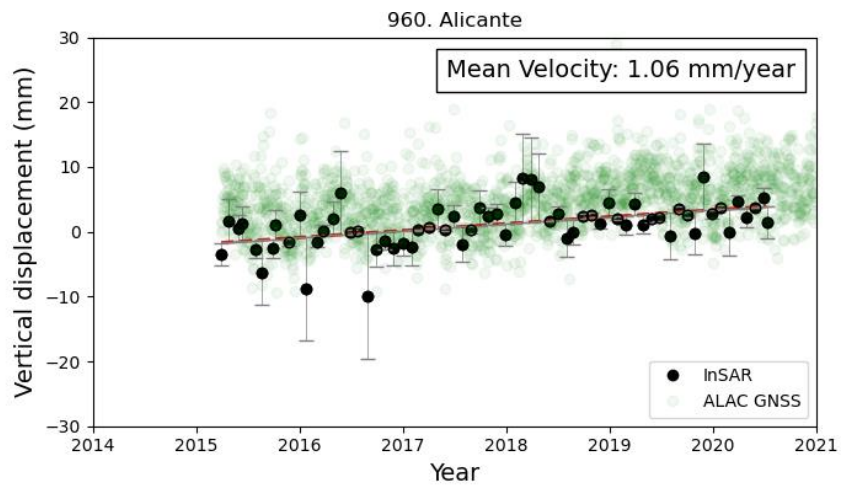
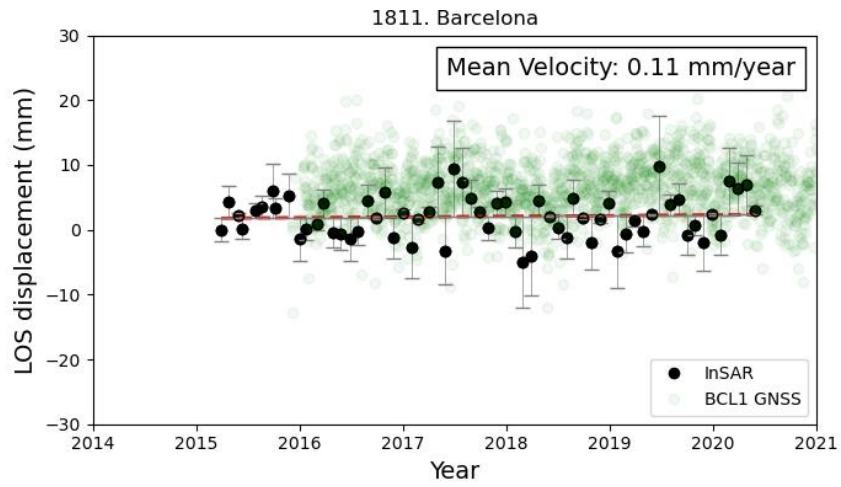


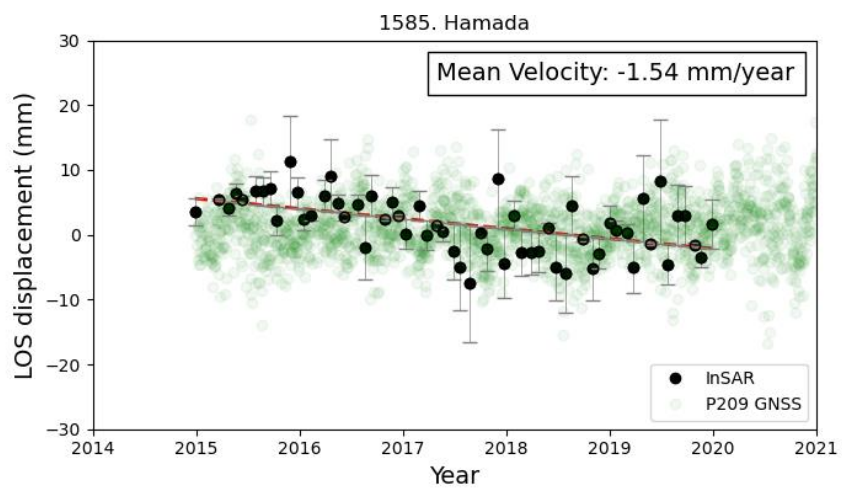
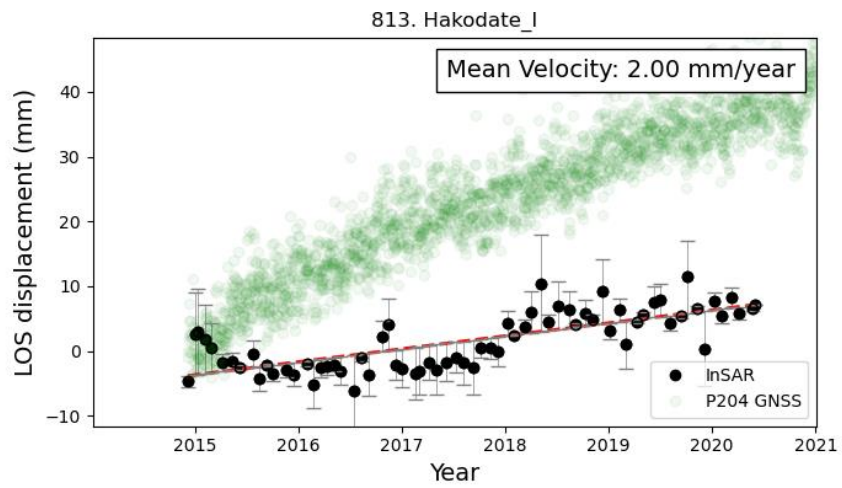
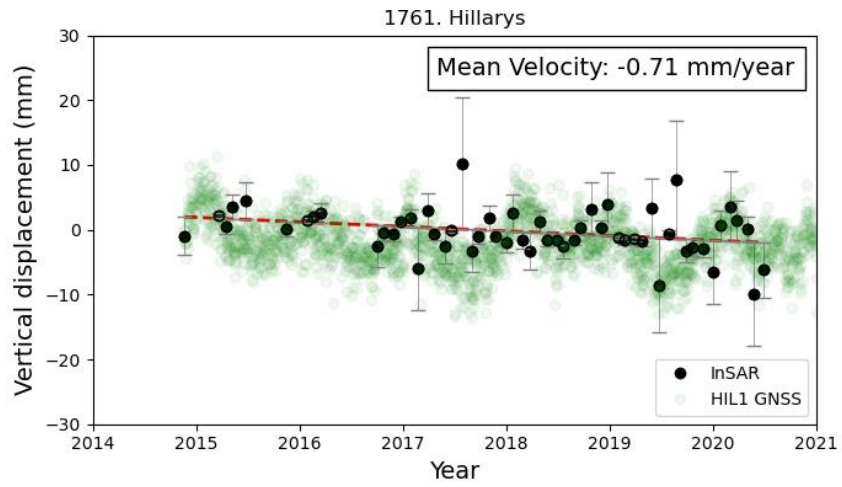
Figure 4.11. Mean VLM rate (mm/year) at tide gauges in the Australia & New Zealand region

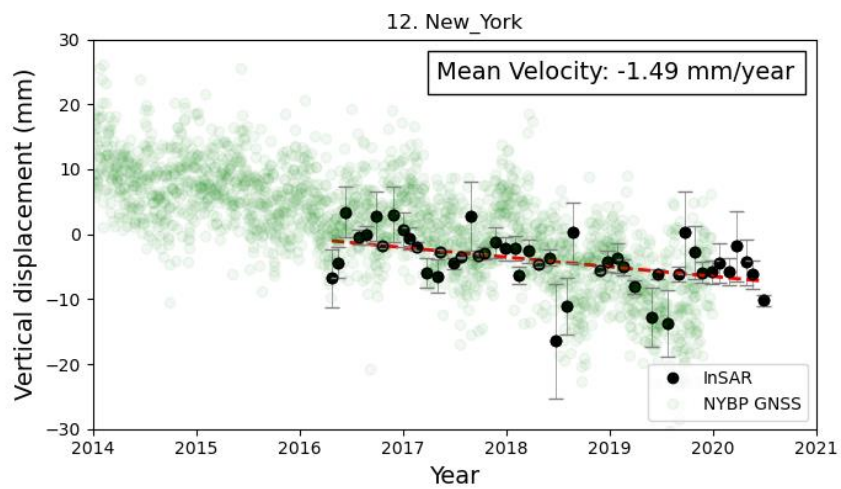
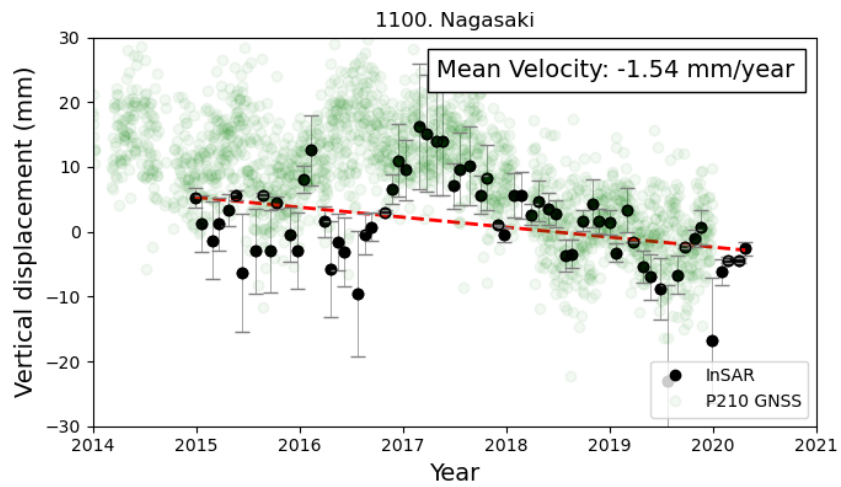
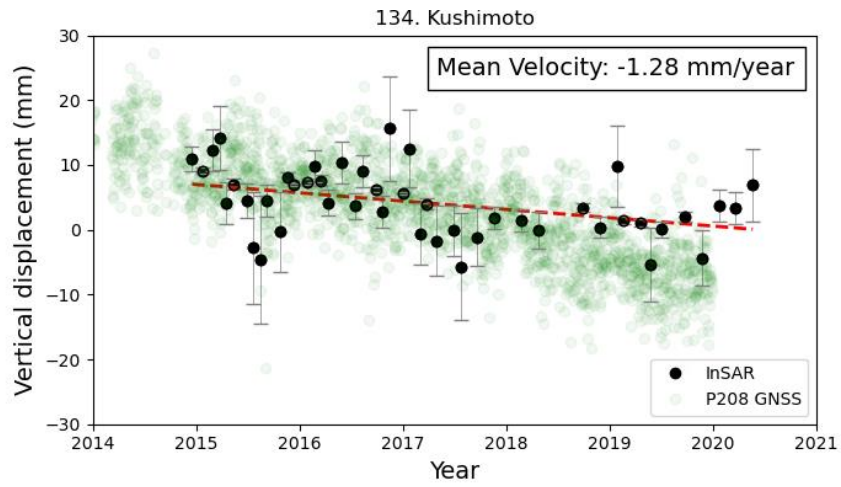
4.5. Comparison of InSAR results with GNSS observations

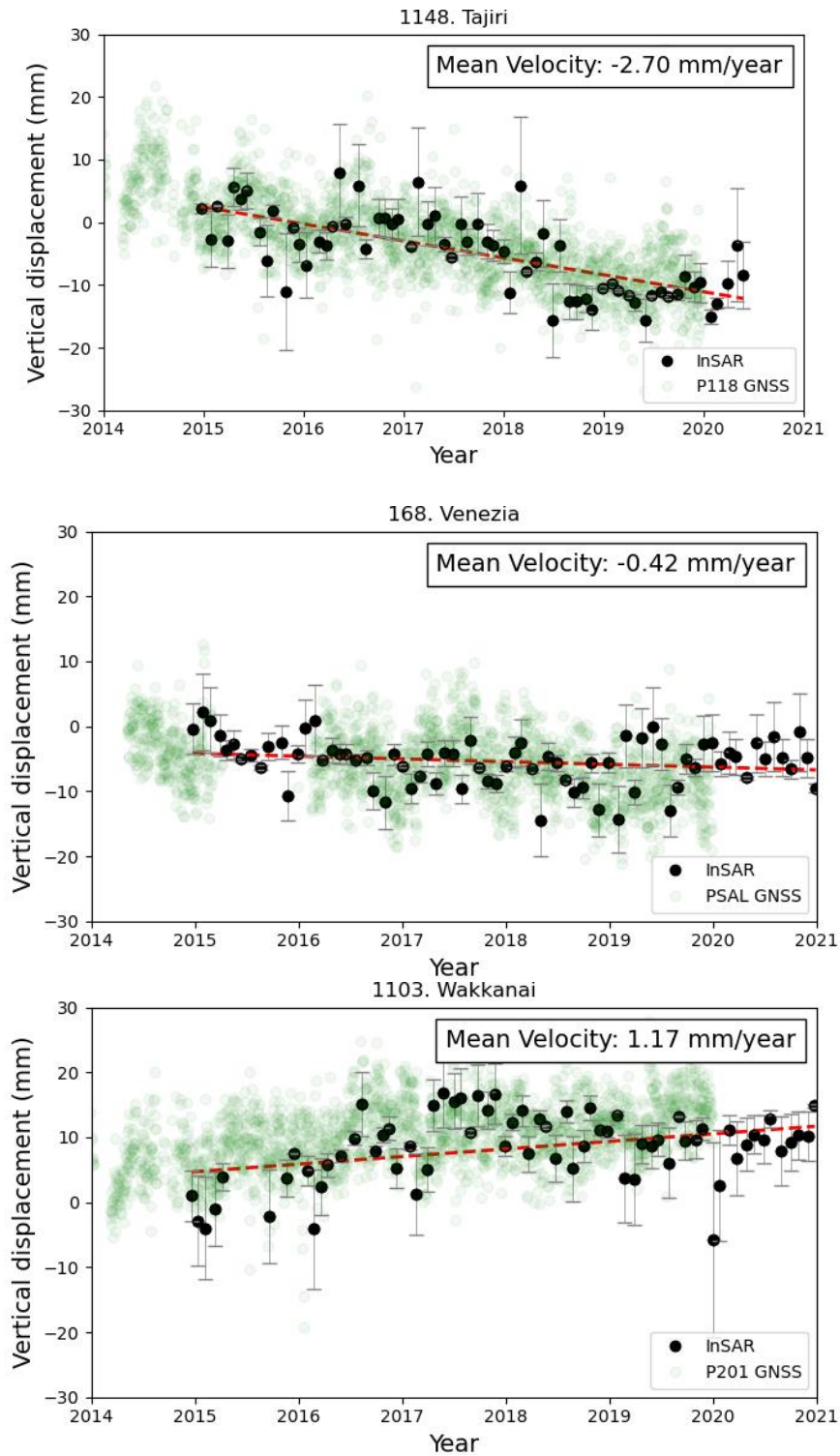
To assess the reliability of the VLM between 2014/12 and 2020/12, the time-series LOS displacement derived from the Seq-TInSAR using Sentinel-1 SAR data are compared to the GPS observations available at tide gauge or near the tide gauge stations. Among the 100-tide gauge sites used in this study, about 12 sites have active GPS observations and therefore, the comparison between the time-series InSAR VLM and GPS derived VLM trend was performed (Figure 4.10).

The continuous ENU position time-series of these GPS stations are obtained from the Nevada Geodetic Laboratory (NGL) at the University of Nevada, Reno, USA (Blewitt et al., 2018). For the comparison, the three vectors of GPS displacements are projected into InSAR line-of-sight direction. Both InSAR and GPS are referenced to common time. Based on the comparative analysis, the VLM derived from Seq-InSAR shows good agreement with the VLM derived from the GPS stations.









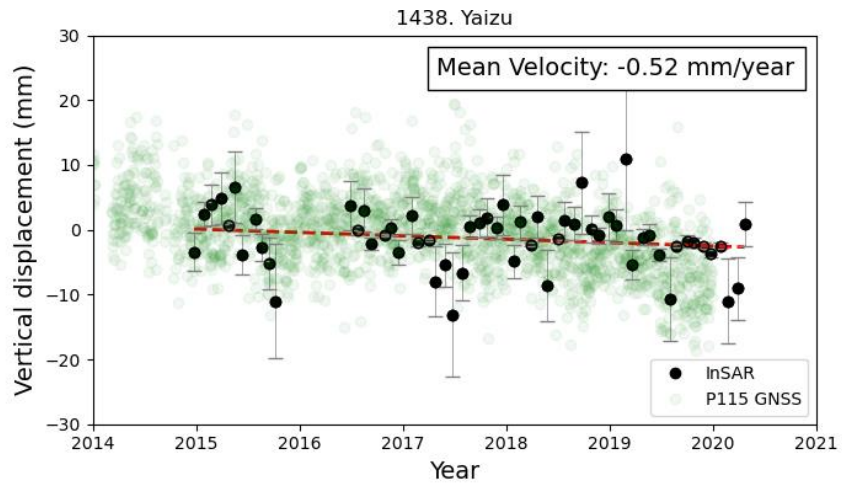


Figure 4.12. Comparison of InSAR VLM trend and GPS derived VLM trend (red dotted line indicates the linear trend of InSAR displacements)

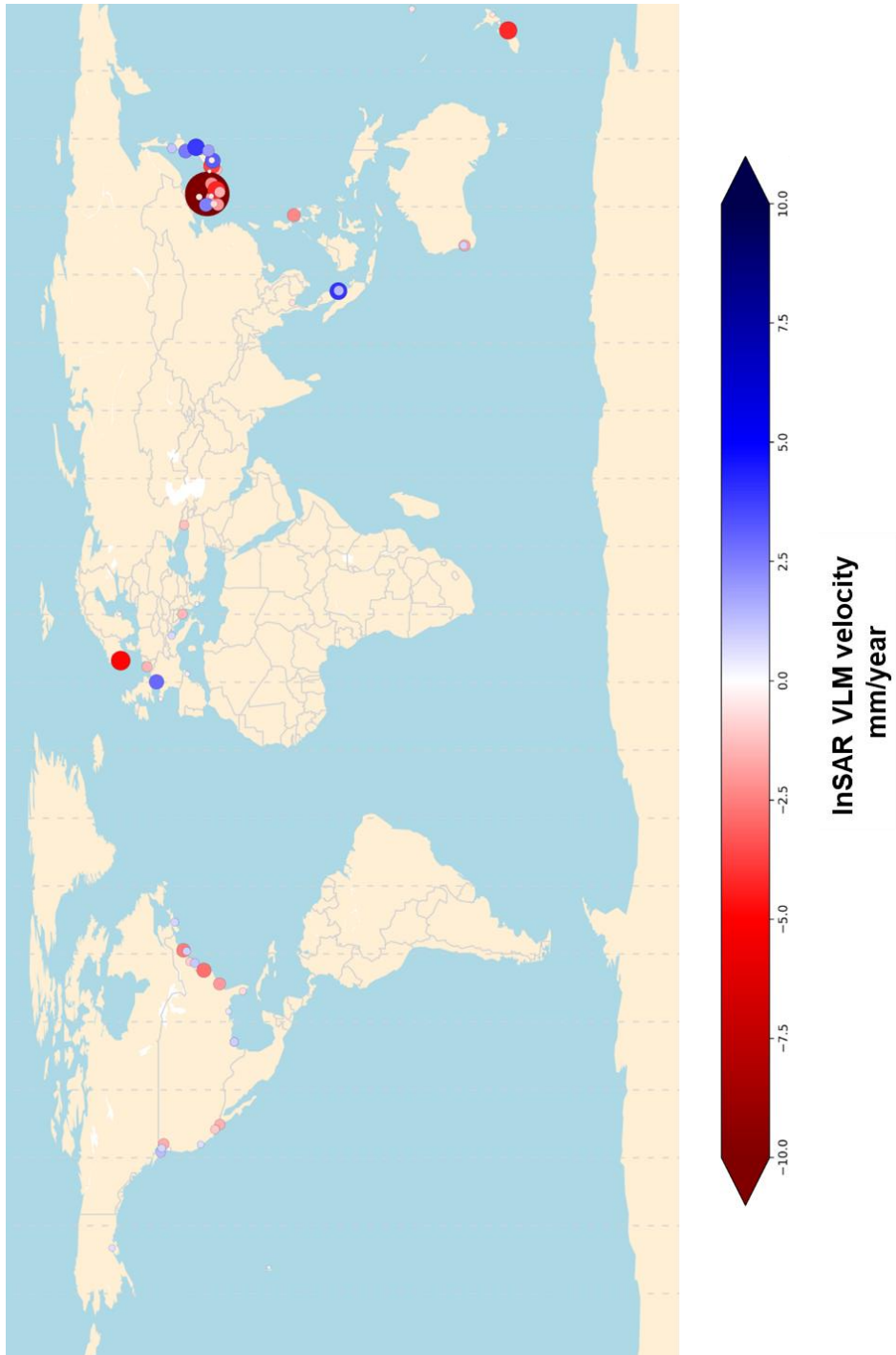


Figure 4.13. Vertical Land Motion velocities at tide gauges around the world estimated from Seq-InSAR

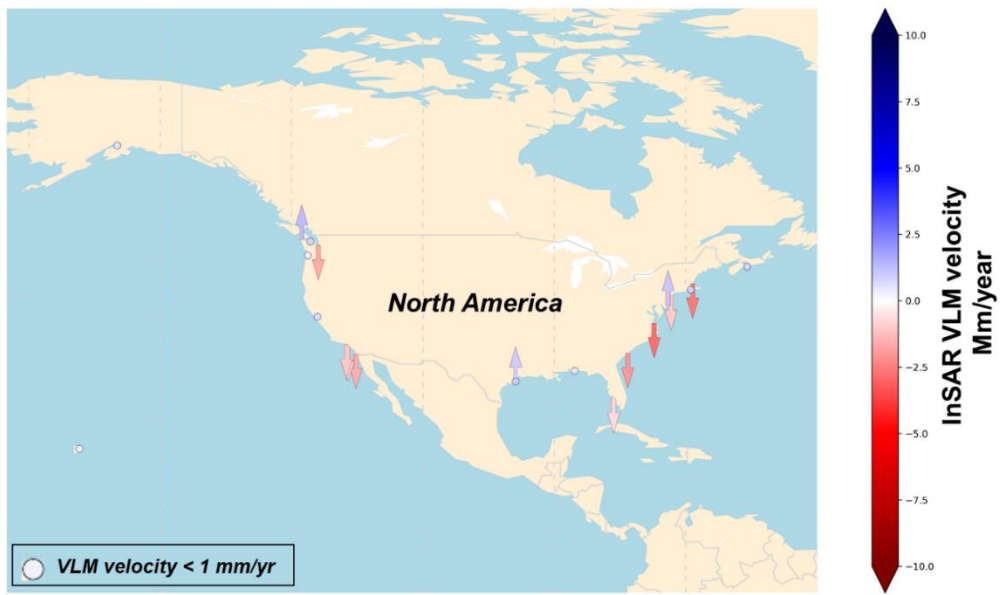


Figure 4.14. Vertical Land Motion velocities at tide gauges in North America region estimated from Seq-InSAR



Figure 4.15. Vertical Land Motion velocities at tide gauges in the Europe region estimated from Seq-InSAR

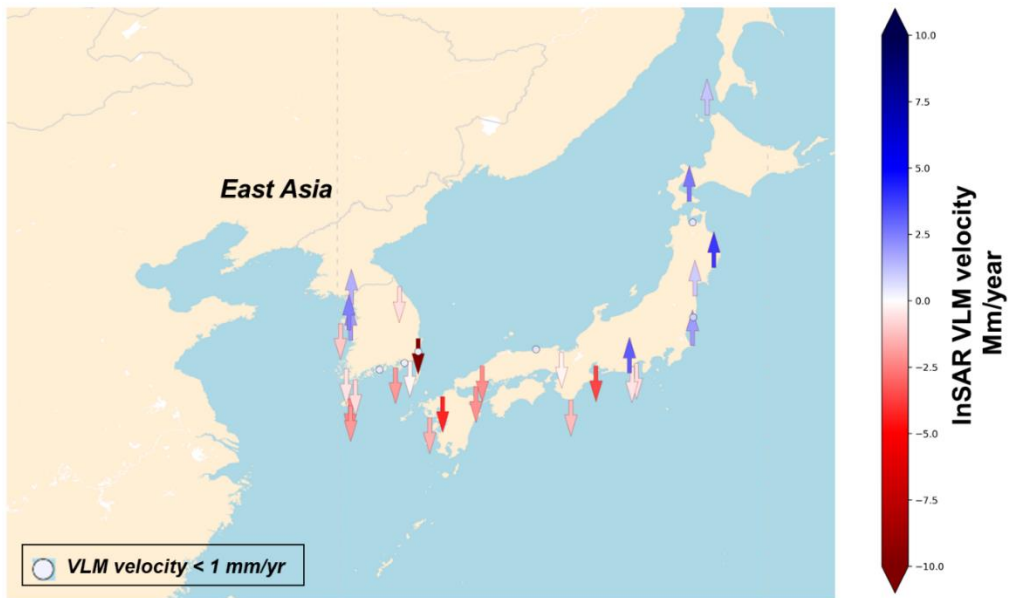


Figure 4.16. Vertical Land Motion velocities at tide gauges in East Asia region estimated from Seq-InSAR



Figure 4.17. Vertical Land Motion velocities at tide gauges in South Asia region estimated from Seq-InSAR



Figure 4.18. Vertical Land Motion velocities at tide gauges in the Australia & New Zealand region estimated from Seq-InSAR

Based on the rate of VLM estimated using the Seq-TInSAR, the impact of the vertical land motions on the tide gauges investigated in this study are illustrated in the Table 4.3. The major tide gauge stations are experiencing the VLM of velocity range between -2 mm/year and 2 mm/year for 35 % and 33%, tide gauges, respectively. Further, 16% of tide gauge stations are experiencing a considerable subsidence range between -2 and -5 mm/year. On the other hand, 9% of tide gauge stations are found to be uplifting. The VLM velocity of 6% of tide gauges are excluded due to the processing error in the Seq-TInSAR processing such as phase unwrapping error, unknown error sources.

Table 4.3 Categorization of tide gauges based on the rate of VLM at tide gauges

S.No.	InSAR VLM _{TG} range (mm/year)	% of Tide Gauges used in this study (100 stations)
1.	$VLM_{TG} \leq -5$	1 %
2.	$-5 \leq VLM_{TG} \leq -2$	16 %
3.	$-2 \leq VLM_{TG} \leq 0$	35 %
4.	$0 \leq VLM_{TG} \leq 2$	33 %
5.	$2 \leq VLM_{TG} \leq 4$	9 %
6.	VLM _{TG} (excluded)	6 %

Relationship between Relative sea level change and VLM_{InSAR}

The VLM velocity at abnormal tide gauges was computed from Sentinel-1 InSAR data for the period 2014/12 – 2020/12 using Seq-TInSAR. Most of the tide gauges investigated in this study were not equipped with GNSS stations or other geodetic methods to estimate the ground motion at tide gauges. In this chapter, a large number of Sentinel-1 SAR datasets were processed to show the potential of the time-series InSAR technique to correct the overestimated relative sea level change.

Among these findings, tide gauges that are affected by vertical land motions both subsidence and uplift are presented in Figure 4.19 and 4.20. First, the Legaspi tide gauge station located in south Asia can be affected by the local coastal subsidence. The Legaspi

tide gauge station showed long-term mean sea level variations as 5.51 ± 0.61 mm/year (NOAA). The VLM derived from Seq-TInSAR processing was estimated as -2.27 mm/year (Figure 4.19). Therefore, the relative sea level trend in Legaspi can be affected by the coastal land subsidence.

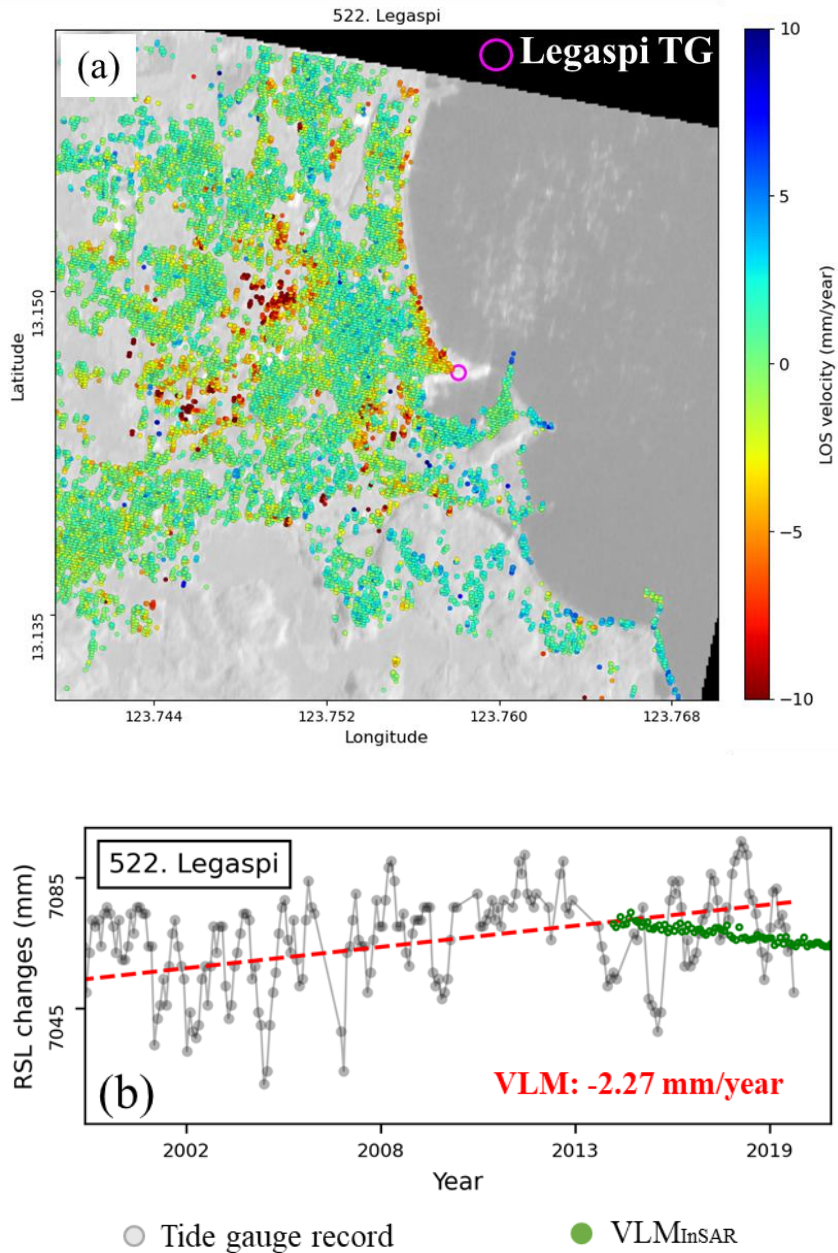
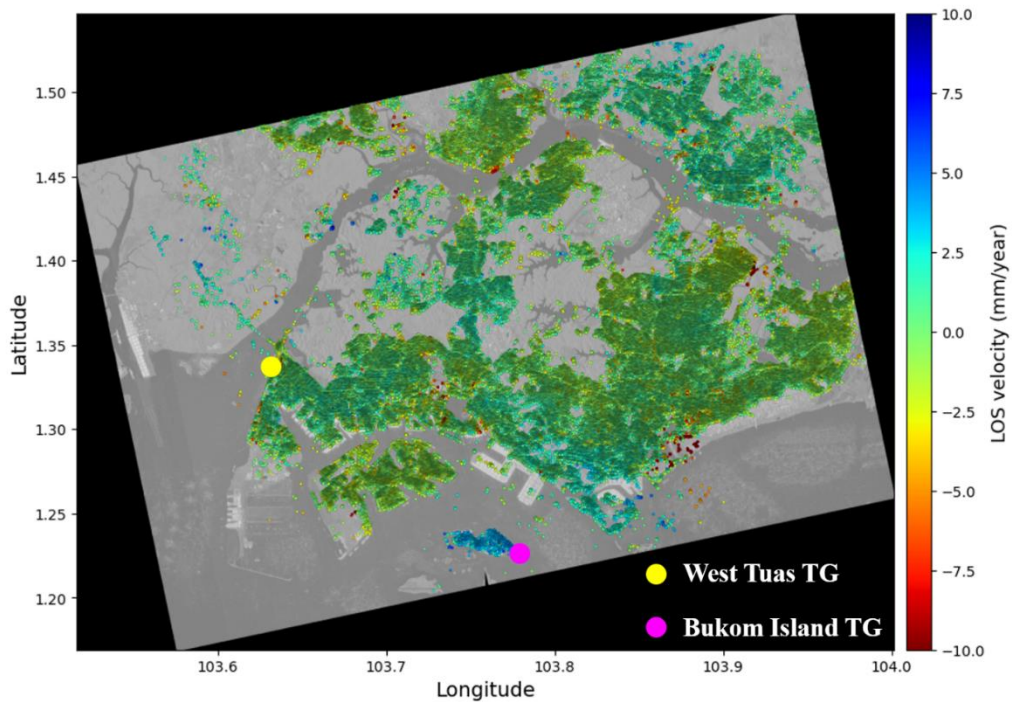


Figure 4.19 (a) Mean LOS velocity from Seq-TInSAR over the Legaspi, Albay bay;
Relationship between the relative sea level trend and InSAR derived VLM.

A linear sea level trend and VLM trend for the two tide gauges in Singapore coast were presented in Figure 4.20. Singapore is one of the densely populated coastal region where land motions (both uplift and subsidence) due to local processes such as soil consolidation, local site disturbances Both the west tuas and bukom island tide gauges in the Singapore were showing abnormal relative sea level changes in the recent years. Since, these stations were not equipped with



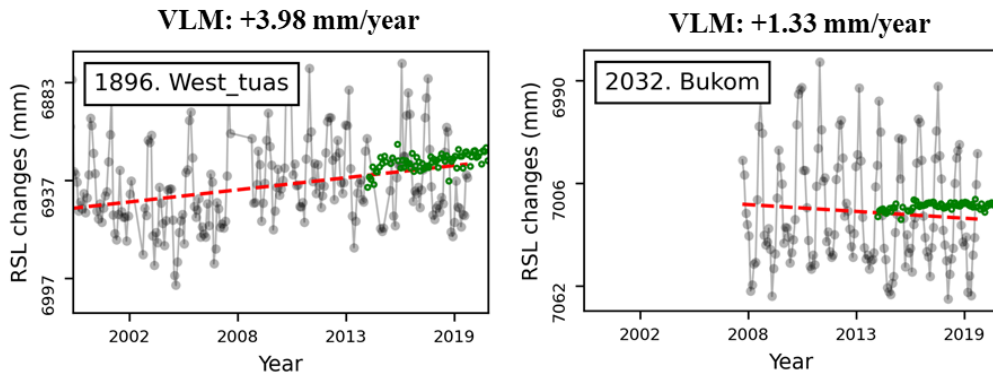


Figure 4.20 (a) Mean LOS velocity from Seq-TInSAR over the Singapore coast; Relationship between the relative sea level and InSAR derived VLM (b) West tuas tide gauge (c) Bukom island tide gauge.

4.6. Discussion

Despite the limitations, tide gauges play a vital role in observing relative sea level changes; however, the observations are limited to land motion and sparse distributions around the world. Several studies have provided the sea level reconstruction for post-glacial rebound and other natural processes (Church & White, 2011; Wöppelmann & Marcos, 2012). Nevertheless, until now the rapid land motion at tidal gauge caused by anthropogenic processes has not been extremely considered for the reconstruction of rapid SLR. Although, the GPS measurements provide useful information on land motions, the lack of co-located stations and sparse distributions are major limitations in representing the localized VLM at tide gauges. As the InSAR and GPS displacements were validated and showed good agreement, the Seq-TInSAR derived VLM at tide gauges are very useful in relative sea level change studies.

In this chapter, the Seq-TInSAR processing chain is introduced to measure the VLM rate of tide gauges for monitoring the stability of the tide gauges. The time-series profiles of individual tide gauges and corresponding InSAR VLM for 100 tide gauges are presented in Appendix – A. The quantitative values of VLM rates of individual stations are listed in Appendix – B.

The mean VLM velocity maps shows that the phase signal from the coherent and low-coherent pixels in the urban and sub-urban coasts are well processed without unwrapping errors. Whereas some tide gauge sites such as Gadeokdo, Fort prachula, Kanmen, Galveston, Grand Isle and Kamaisi are covered by highly vegetated terrains are affected by phase unwrapping error and dropped from estimation. For other stations with acceptable pixel density, after estimating the mean VLM velocities, I have dropped the unreliable pixels based on the standard deviation of the mean velocity estimates. Moreover, it is clear that the majority of the tide gauge sites are not affected by the atmospheric phase delays as their effects are smaller in magnitude and evenly distributed throughout the interferograms which having minimal spatial coverage in our case (Ding et al. 2008).

The general limitations of the study are discussed as follows. One of the key limitations of the study is that the maximum length of the SAR datasets available for the InSAR VLM are only six years from 2017 to 2021, whereas the tide gauge observations spans on average of 30 years. In order to ensure the long-term stability of the tide gauge, the current InSAR estimates are limited. However, the estimated InSAR-VLM can represent the long-term stability of tide gauge sites, which exhibits a linear VLM trend over the

InSAR period and tide gauge period. In addition, the InSAR VLM estimated in the proposed method is optimally separates the non-linear land motion at tide gauges during the InSAR period. This limitation can be overcome by past missions like ENVISAT, ALOS-1, and future SAR missions like NISAR, Radarsat Constellation Mission (RCM). The graphical representation of this chapter is presented in Figure 4.21.

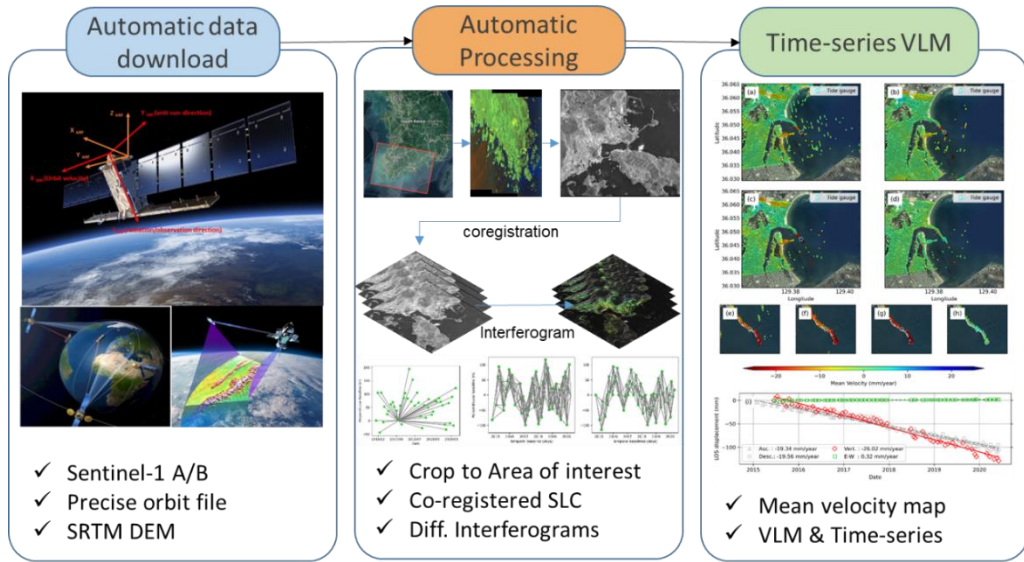


Figure 4.21. Schematic representation of Seq-TInSAR VLM product generation

Chapter 5. Conclusions and Future Perspectives

In this study, the estimation of Vertical Land Motion estimation at tide gauges by time-series InSAR algorithm have been presented using Sentinel-1 A/B SAR data. Due to the regional and local processes, causes inhomogeneity in the sea levels. Despite the importance of sea level measurement accuracy, unexpected local factors can deteriorate sea level records and result in unreliable interpretations. The changes in the regional relative sea level are the cumulative result of many individual geodetic processes that vary both in space and in time. Therefore, the relative sea level records represents the combination of the change in land surface elevation (land motion) and change in global sea level. In coastal areas, the sinking of land surface known as subsidence and uplifting of land surface, are referred to vertical land motion (VLM) and normally occurs at rates of mm/year. Though this VLM rate appears small, it can affect the relative sea level change at the substantial amount. The impact of VLM on tide gauges have different impacts from place to place based on the natural and anthropogenic processes on the coastal areas. The VLM phenomenon on the coasts can be both steady that are ongoing for long-term and transient that occurred in the last few years. It is essential to understand the spatial and temporal characteristics of VLM at any given tide gauge location.

With the advent of recent Sentinel-1 A/B satellite, the freely available C-band SAR data has opened the innovative applications for Interferometric studies. The results from the time-series InSAR analysis carried out with the StaMPS PSI/SBAS algorithm bring completely new knowledge about the VLM at the tide gauges with a great precision and

with an unprecedented spatial resolution in this application using Sentinel-1 A/B SAR data.

From Chapter 3.2, the StaMPS PSI analysis reveals the Pohang tide gauge station is seriously affected local subsidence during the period 2014 to 2017. These vertical movement of Pohang tide gauge station is confirmed with the co-located POHA GPS station and the in the geological context of the Guhang port which is categorized as reclaimed land. In addition, these PSI results shows the unpublished knowledge on the subsidence of the Guhang port at the rate of -25.5 mm/year and rest of the neighbouring areas as stable. The Pohang Tide Gauge Station has been recording sea level rises that are higher than those of neighboring stations and of the global mean. Here, the estimation of vertical ground motion at the Pohang Tide Gauge Station was presented using multi-track time-series InSAR analysis; the results verify that ground motion is a vital factor in the measured sea level change, resulting in an overestimated sea level trend (+3.1 cm/year since 2013). The estimated vertical ground motion (-2.55 cm/year) was validated against the ground motion rate from GPS observations (-2.67 cm/year) at a collocated station. The multi-track PS-InSAR technique can be applied to any tide gauge located in a coastal area to determine the influence of vertical ground motion on the observed SLR with high spatial resolution. Thus, this chapter justifies the StaMPS PSI analysis to estimate the coastal vertical land movements along the coastlines having dominant / persistent scatters.

When extending the method presented in Chapter 3.2 to other vulnerable tide gauge sites, identified a challenging problem. The conventional StaMPS PSI / SBAS analysis faces difficulty in identifying the phase signals where the terrain has both dominant and non-

dominant scatter. In chapter 3.3, a sequential pair selection based time-series Interferometric SAR method was presented to estimate the vertical land motion at tide gauge stations along the coasts of the Korean peninsula. The proposed method demonstrated to increase the density of coherent pixels in a natural terrain along with the coastal areas and estimated VLM with unprecedentedly high spatial resolution. For sequential pair selection approach, the selection of initial PS pixels have been doubled compared to conventional StaMPS SBAS analysis. In addition, the noisy pixels are dropped effectively. The highest rate of vertical land motion was estimated at Pohang tide gauge station at -26.02 mm/year and has a good agreement when compared to linear trends of collocated GNSS vertical velocities (-26.35 mm/year) and in-situ leveling measurements (-25.89 mm/year). An uplift of the Incheon tide gauge ($+1.53$ mm/year) and subsidence at Jeju (-2.4 mm/year) and Seogwipo (-2.0 mm/year) was observed. Due to the limited existence of collocated GNSS stations, the vertical land motions were unveiled at these tide gauges in the Korean peninsula. Our findings suggest that the time-series SAR Interferometry method has taken the advantage of large spatial coverage and high repeat cycle for monitoring of vertical land motion over the study area to a millimeter level accuracy. Further, this chapter reveals the importance of VLM in the Korean tide gauges, and therefore it is essential to correct the VLM affected tide gauge records in the future using InSAR velocity estimates. Additionally, our approach is expected to apply beyond the Korean peninsula, especially at tide gauges in which vertical land motions are not monitored. However, it is necessary to highlight that there is a need for further developments to mitigate the InSAR derived vertical land motion at relative sea-level changes for future sea-level projections.

The modified InSAR pair selection approach is proposed in Chapter 3 improves the quality of time-series InSAR processing in order to achieve the sub-millimeter per year and acceptable uncertainty, for the estimation of vertical land motion. Here, the short temporal Sentinel-1 interferograms generated at full resolution, because the target is to monitor the tide gauge site. Hence, the optimal processing parameters are carefully opted for sequential StaMPS-SBAS analysis to isolate the reliable coherent pixels with minimal error sources. The key limitation in this method is to ensure the acquisition of Sentinel-1 SAR data with fair temporal resolution. Because the data gaps more than 6 months in the data stack introduces phase unwrapping error and unknown decorrelation sources. Therefore, the method can be further improved for applicable to the tide gauge sites located with sufficient spatial and temporal resolution.

In chapter 4, the proposed method is implemented to the 100 tide gauge sites selected around the world that exhibiting abnormal sea level change trends. Due to the increasing interest to apply the proposed method to selected tide gauge sites, it is evident that the acquisition and exploitation of large Sentinel-1 SAR dataset needs effective solutions for downloading, storing and processing. From this processing point of view, a fully automatic framework for Sequential SBAS approach, referred to as Seq-TInSAR, is presented in this study. The detailed Seq-TInSAR architecture and each component of Seq-TInSAR is explained in the chapter 4. As a final result, the VLM time-series and corresponding mean VLM velocities were computed for the period between 2014 and 2020. The results presented in the Chapter 4 demonstrates the effectiveness and robustness of the proposed Seq-TInSAR approach and exploitation of large volume of Sentinel-1 SAR data. As for the future perspective, the proposed Seq-TInSAR module is

tested for Pohang tide gauge site in the Amazon Web Services (AWS) EC2 instance to improve the computational efficiency.

The VLM estimated for the selected 100 tide gauge sites from the Sentinel-1 SAR data is presented in this study. The mean VLM velocity maps derived from Seq-TInSAR module are categorized into five regions based on the abnormal trend observed in the tide gauge observations. Under this assumption, majority of tide gauge sites identified over the North America, Europe and East Asia regions where, long-term sea level changes are being observed. The time-series VLM estimates were compared with the permanent GPS stations and found good agreement between two methods. The estimated VLM rates are obtained with sub-millimeter accuracy. Apart from Pohang tide gauge stations the tide gauge sites along the eastern Japan and south eastern American coasts showed significant VLM velocities. Most of the other sites showed VLM velocities within the range of -1 mm/year to +1 mm/year. The estimated VLM velocities of tide gauges are relative estimates, not the absolute velocities. Despite this limitation, the local linear and non-linear VLM of tide gauge sites investigated in this study is distinctive as this is a first of its kind for employing SAR data to derive InSAR based VLM on a global scale.

The full exploitation of huge volume of Sentinel-1 SAR data through the time-series StaMPS SBAS techniques that are fully automatic, efficient and easy to implement, provides insight to estimate the influence of vertical land motion to the relative sea level changes in the tide gauge observations. The Seq-TInSAR module presented in this work is able to process other operational satellite SAR data including COSMO-SkyMed and ALOS-1 and 2, and has great potential to employ future satellite missions like NISAR and Radarsat Constellation Mission (RCM).

국문 요약문

전 세계적으로 발생하는 해수면 상승은 저지대 해안과 도서 지역에 심각한 위협으로 작용한다. 해안 지역을 보호하기 위해 전 지구 및 해당 지역의 해수면 변화를 이해하는 것은 대단히 중요하다. 조위 관측소는 전 세계에 설치되어 해당 지역 기준에 따른 해수면 변화를 직접 측정한다. 지난 30년간 해수면은 IPCC (정부 간 기후 변화 패널)가 추정한 20 세기의 해수면 상승 (3.35mm / 년)대비 1.8mm / 년 가까이 상승하였다. 그러나 해수면 상승의 원인과 함께 연직 지반 운동 (VLM)은 지역 해수면 변화를 이해하는데 필수적인 요소이지만 그 기여도는 여전히 불분명하다. VLM 은 자연 활동과 인간 활동 모두에 의한 지역적 변화로 인해 조위 관측소에서 지반의 고도 변화로 정의되며 해수면 변화 정확도를 악화시키고 유사 해수면 변화의 가속을 초래할 수 있다. 전 세계 및 지역 해수면 상승을 재구성하려면 1 밀리미터 미만의 정확도로 조위 관측소에서 VLM 을 평가하는 것이 필수적이다. 이전 연구는 GPS (Global Positioning System)를 통해 제한된 위치에서 VLM 을 관측하려고 시도하였으나 국소적인 GPS 신호들로부터 관측된 VLM 으로는 그 추정이 불확실하다.

본 연구에서는 시계열 SAR 간섭계 (InSAR) 기법을 이용하여 SAR (Synthetic Aperture Radar) 데이터를 통해 공간적, 시간적 변화를 포함한 상대적 VLM 을 직접 측정하기 위한 대안적 접근 방식을 제안한다. 이 작업은 시계열 InSAR 분석을 사용하여 광대역에 걸쳐 높은 공간 해상도로 VLM 속도의 추정을 향상시키는 데 기여한다.

첫째로, Sentinel-1 A / B 위성의 C-band Interferometric Wide-swath (IW) 모드 SAR 영상이 본 연구에서 조위 관측소의 VLM 속도를 추정하는 데 사용되었다. Sentinel-1 A / B SAR 영상은 2014 년 10 월부터 2020 년 12

월까지 (~ 6 년) 기간 동안 수집되었다. 고정 산란체를 위한 스탠포드 기법 – 고정 산란 간섭계 (StaMPS-PSI) 시계열 InSAR 알고리즘이 한반도 포항 조위 관측소의 2014 ~ 2017 년 동안의 조위 관측소의 안정성과 VLM 속도를 모니터링하기 위해 적용되었다. 포항 조위 관측소 부지의 경우, 위성궤도의 상승 및 하강 경로로 획득한 SAR 영상을 통해 시선 방향을 따라 조위 관측소에서의 지면 이동 속도를 도출하였다. 포항 GPS 관측소의 연직 이동은 두 기법 간의 상관성을 판단하기 위해 InSAR 기법으로부터 추정된 VLM 속도와 비교되었다. 포항 조위 관측소의 VLM 속도는 2014 ~ 2017 년의 기간 동안 -25.5mm / 년으로 관측되었다. StaMPS-PSI 추정에 의해 도출된 포항 조위 관측소의 VLM 속도는 해안 지역의 강한 산란 체에서 기인한다.

둘째로, 강한 산란체가 수가 적고 분산된 산란체가 더 많은 지형의 경우, 본 연구에서 Sequential StaMPS-Small baselines (StaMPS-SBAS)이라는 하는 단기 InSAR 쌍의 선택에 의한 접근 방식이 제안되었다. Sequential StaMPS-SBAS 는 짧은 시간 범위($n = 5$)의 간섭계 영상을 형성하여 조위 관측소 부근의 자연 지형에서 변화가 적은 화소 선택을 증가시킨다. Sentinel-1 A / B SAR 영상은 2014 년 ~ 2020 년 사이에 서로 다른 지형 조건을 가진 한반도의 10 개 조위 관측소에서 수집되었으며, VLM 속도 및 시계열 변위를 추정하기 위해 Sequential StaMPS-SBAS 와 함께 사용되었다. 초기 화소 밀도는 기존 StaMPS-SBAS 분석을 통해 확인 된 최종적인 불변화소 밀도의 약 1.25 배와 두 배로 도출되었다.

셋째로, Sequential StaMPS-SBAS 분석에 의한 시계열 VLM 비율의 완전한 자동 추정 가능성을 조사하였다. Seq-TInSAR 라고하는 완전한 자동 처리 모듈이 개발되었으며, 3 개의 하위 모듈로 구성되어있다. 1) Sentinel-1 SLC

(Single Look Complex) 영상, 정밀한 궤도 정보 및 DEM (Digital Elevation Model)의 자동 다운로드 2) SLC 전 처리기 : 영상 별 Burst 추출, 정밀한 통합 및 Stacking, 3) Sequential StaMPS-SBAS 프로세서 : VLM 속도 및 VLM 시계열 변위의 추정

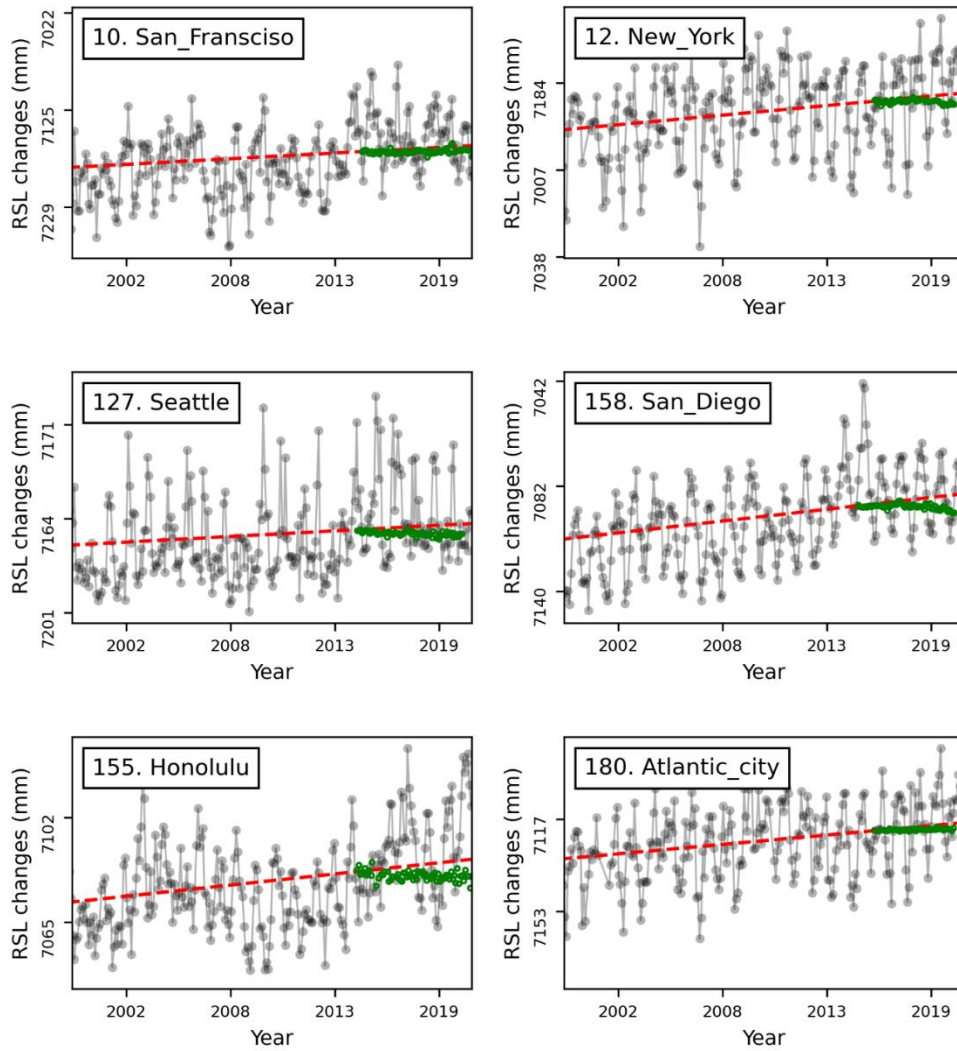
마지막으로, Seq-TInSAR 모듈은 동위 평균 해수면 평균으로 비정상적인 해수면 추세를 보이는 100 개의 조위 관측소에 적용된다. 조위 관측소 지점별로 60 ~ 70 개의 Sentinel-1 A / B SLC 영상을 획득하고 300 ~ 350 개의 시계열 간섭계 영상을 처리하여 조위 관측소에서 VLM 을 추정하였다. 정량적인 VLM 속도와 시계열 VLM 은 선정한 조위 관측소에 대해 추정하였다. VLM 속도를 기반으로 본 연구에서 도출한 조위 관측소는 다양한 VLM 범위로 분류된다. 12 개의 조위 관측소에서 취득한 현장 GPS 관측 자료를 InSAR로부터 추정한 VLM 비율과 비교하여 강력한 상관성을 찾았고, 이는 본 연구에서 제안한 접근 방식이 조위 관측소에서 VLM 의 공간적 및 시간적 변화를 측정하는데 신뢰할 수 있는 자료로 사용될 수 있음을 시사한다.

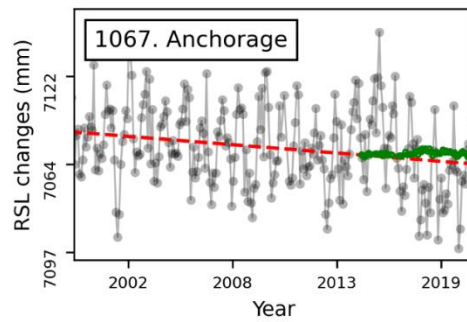
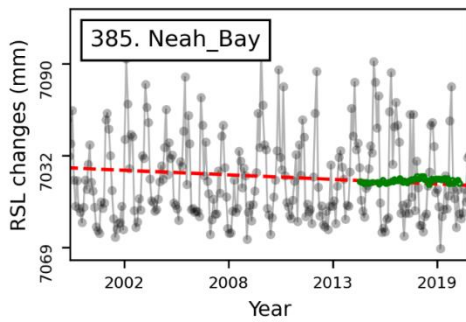
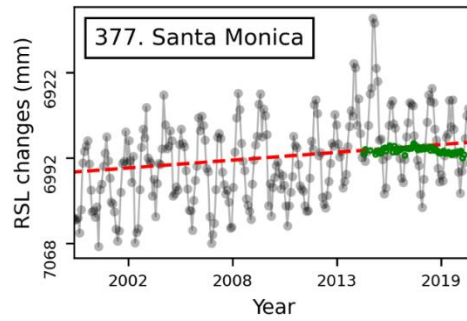
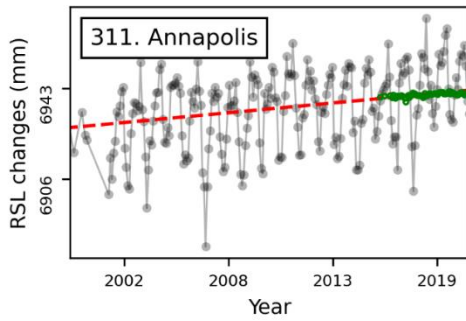
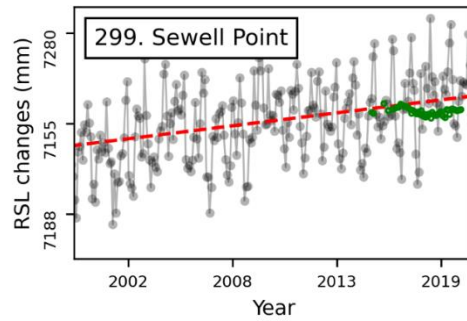
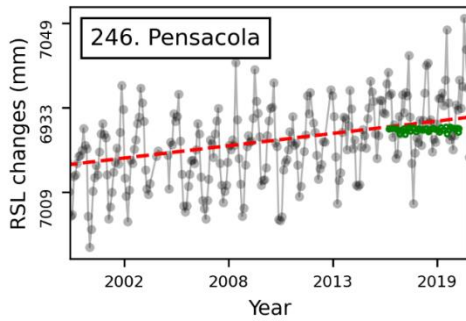
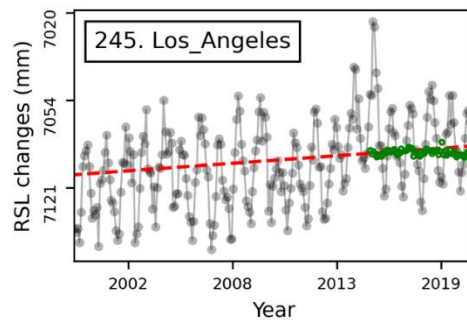
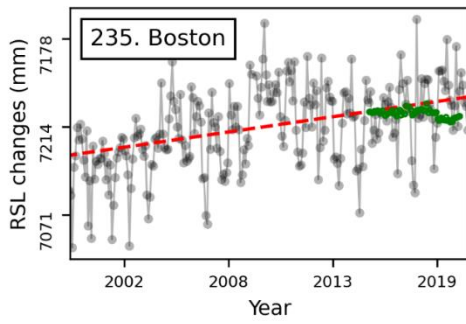
주요어 : Sea level rise, Tide gauge, Relative sea level, Vertical land motion, GPS, Synthetic Aperture Radar, SAR Interferometry, Time-series InSAR, StaMPS

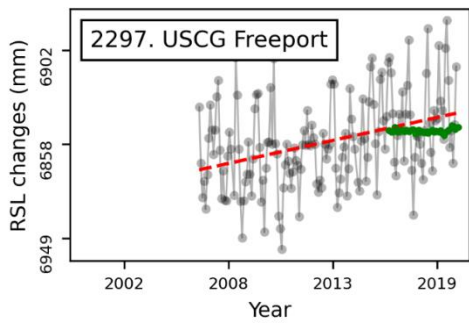
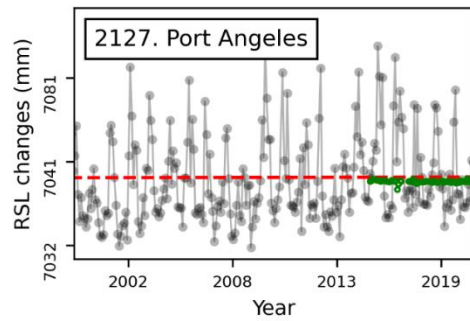
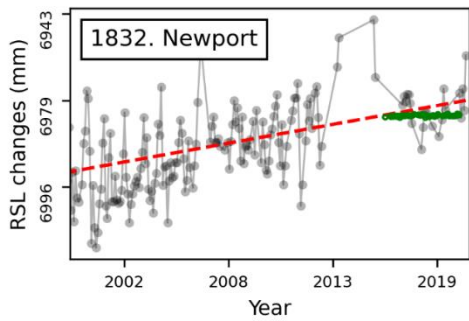
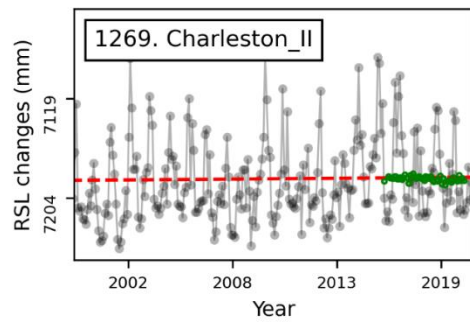
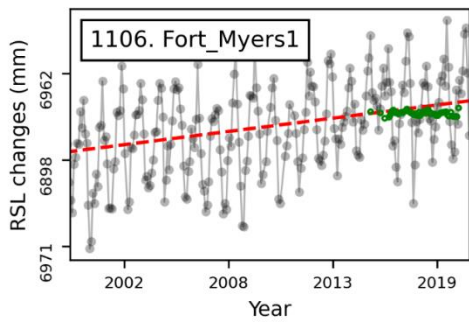
Appendix – A

Plots showing the monthly relative sea level changes from tide gauges and Seq-TInSAR

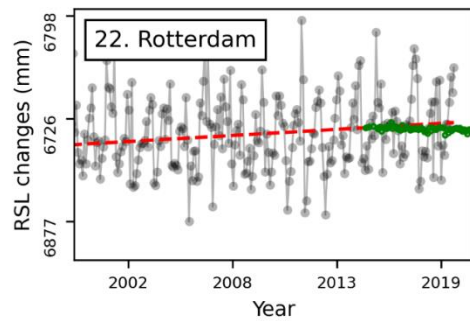
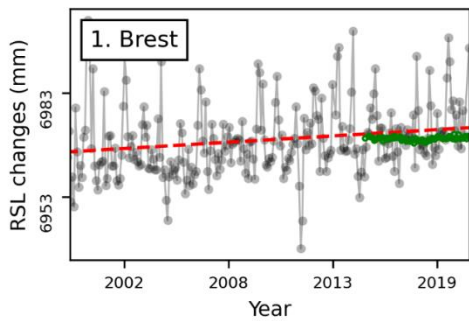
VLM trend

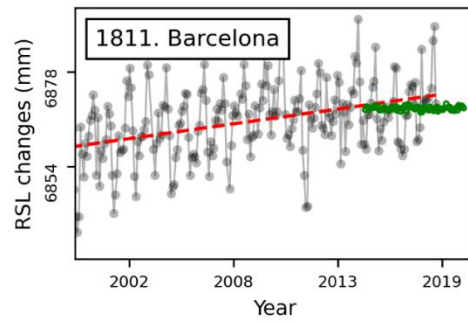
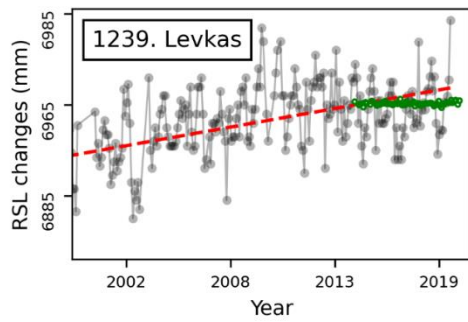
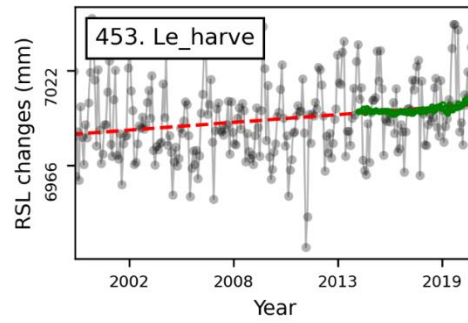
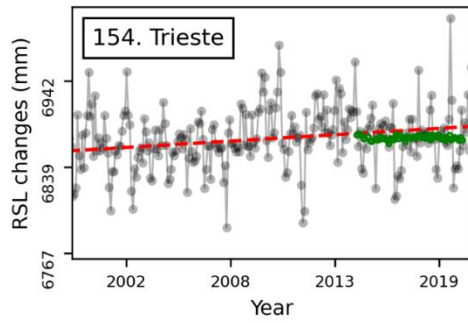
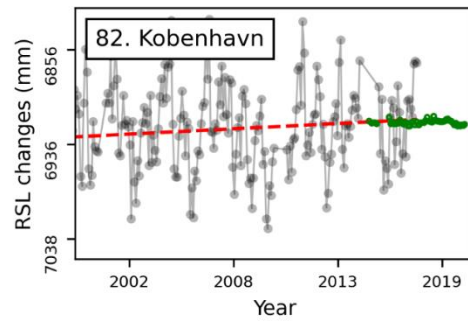
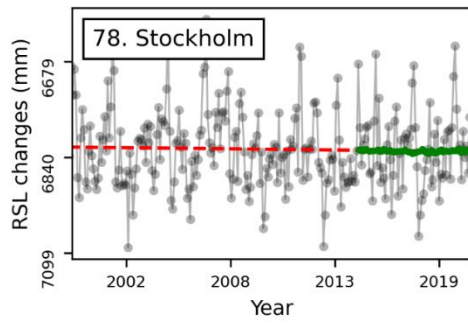
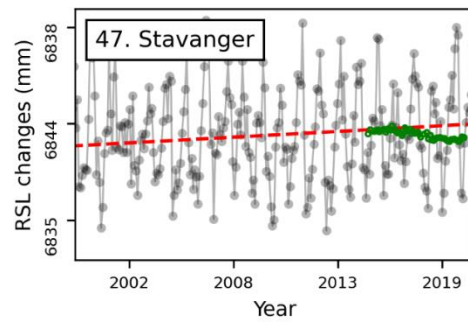
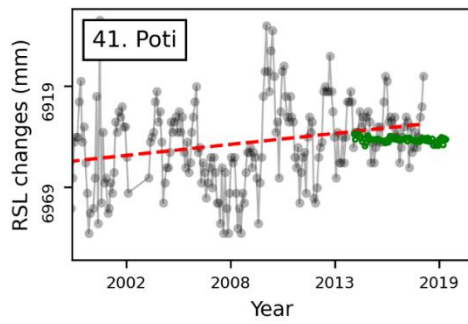


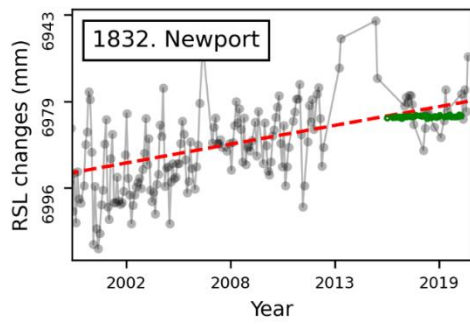




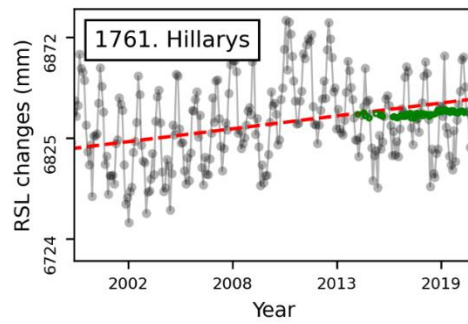
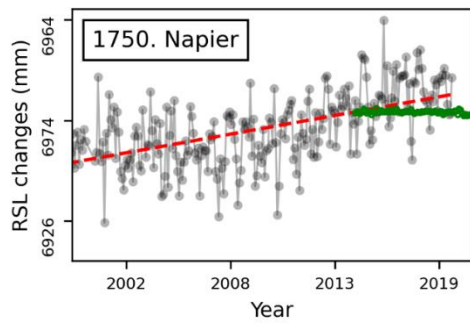
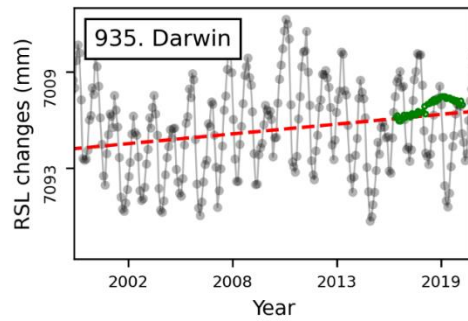
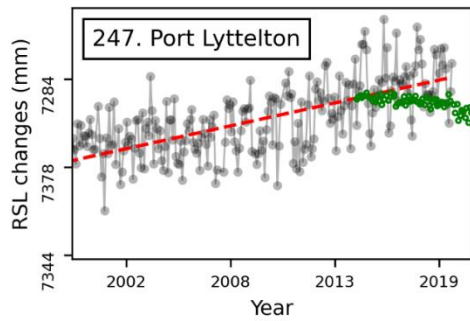
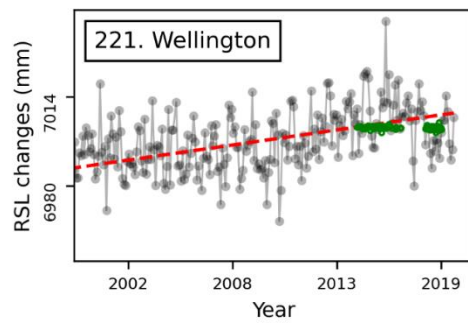
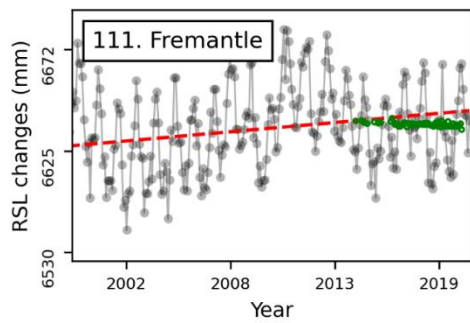
Europe

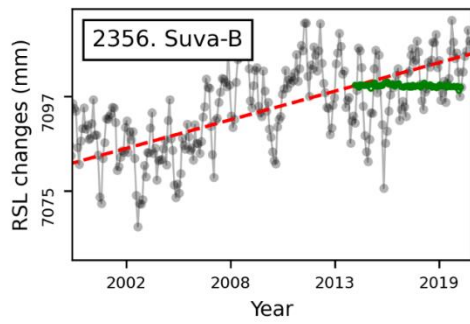




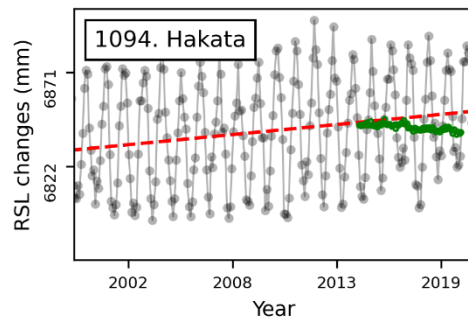
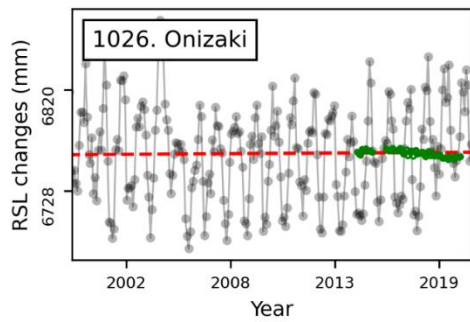
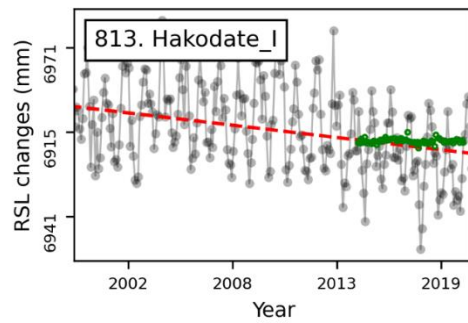
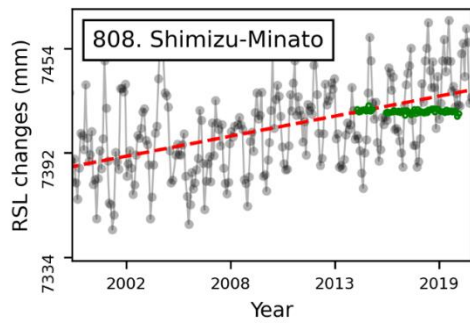
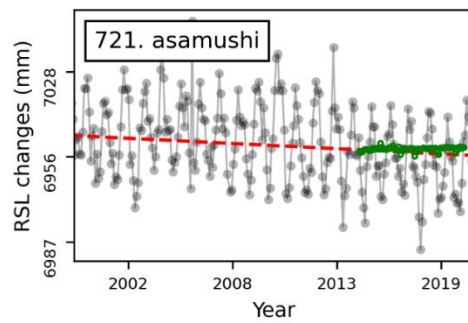
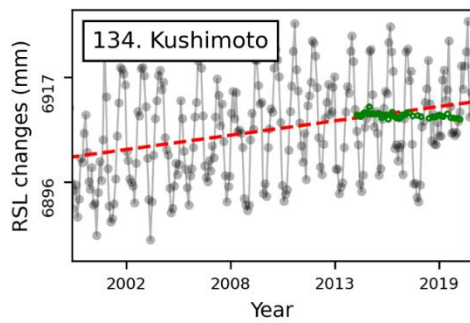


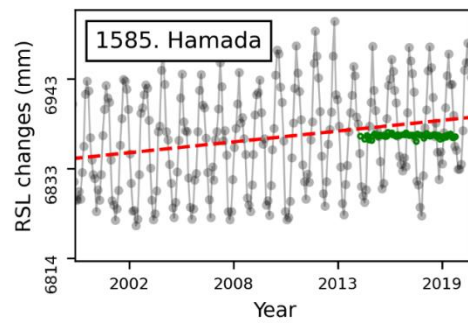
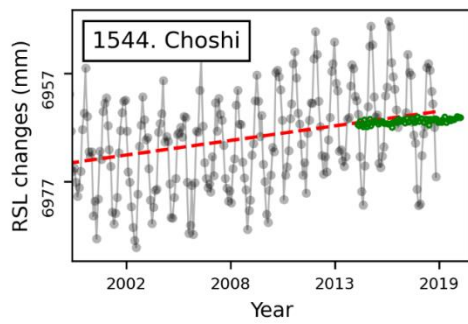
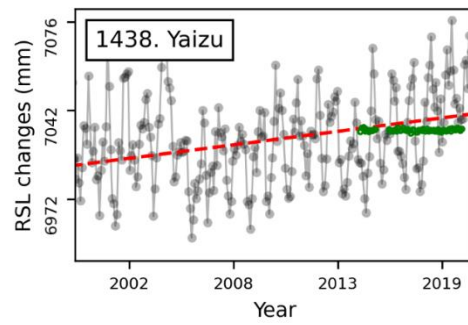
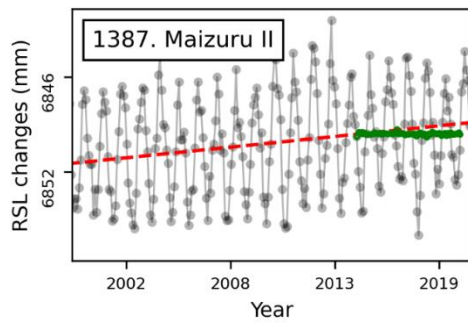
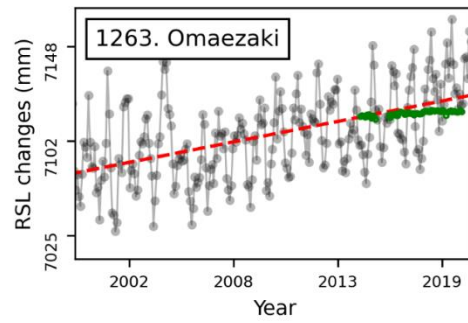
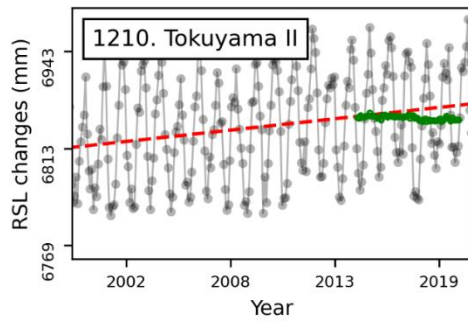
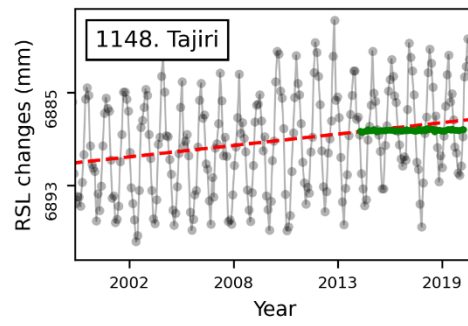
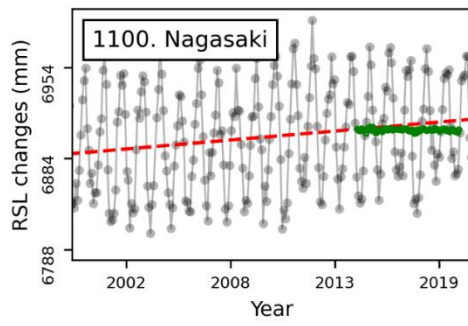
Australia



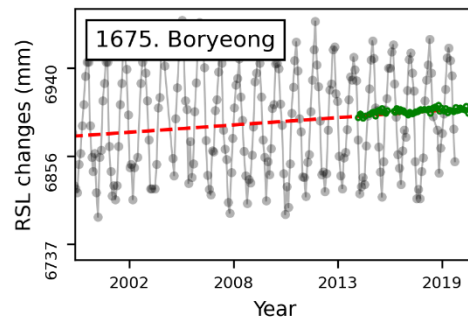
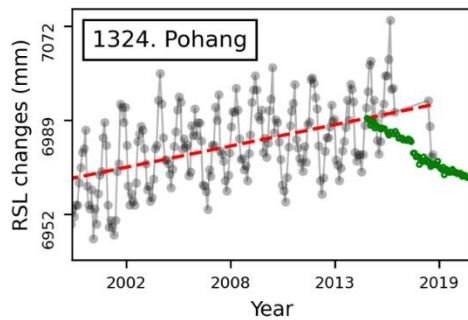
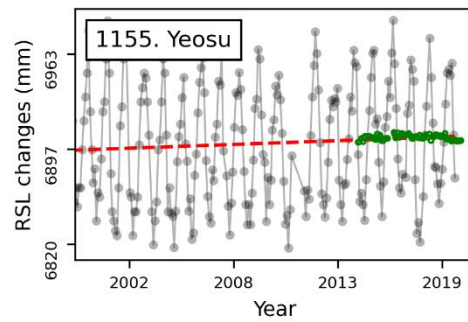
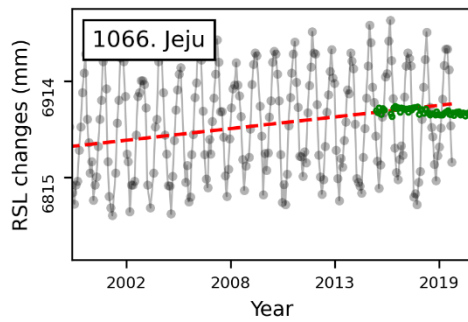
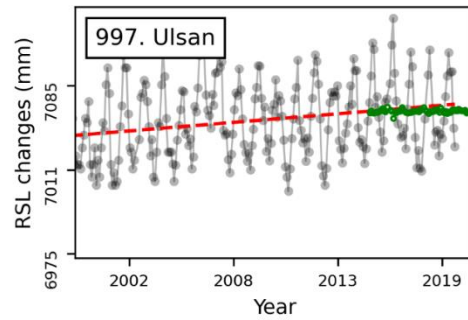
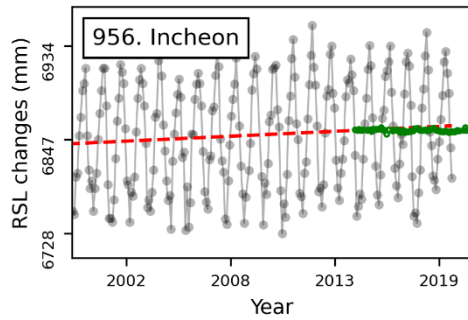
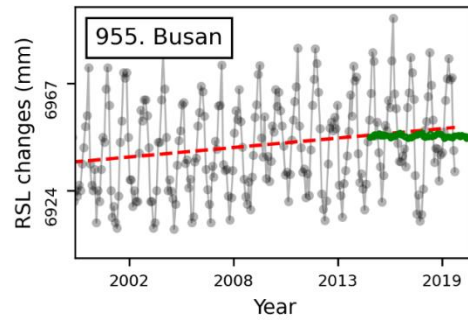
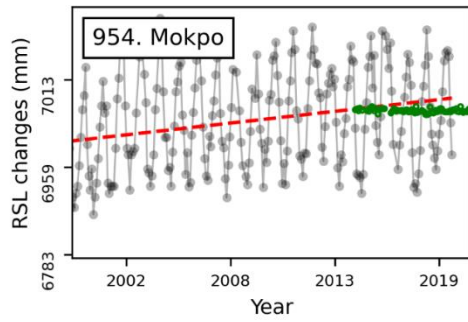


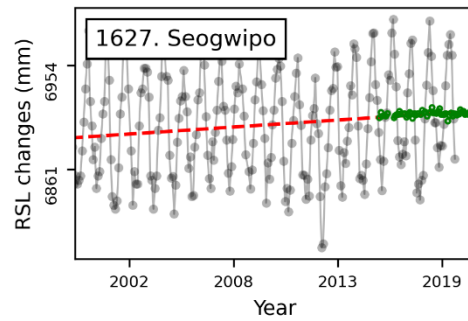
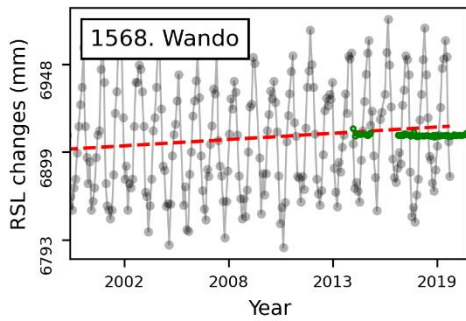
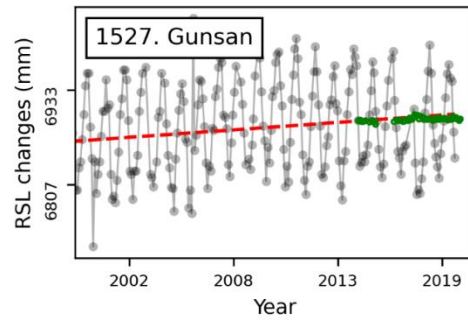
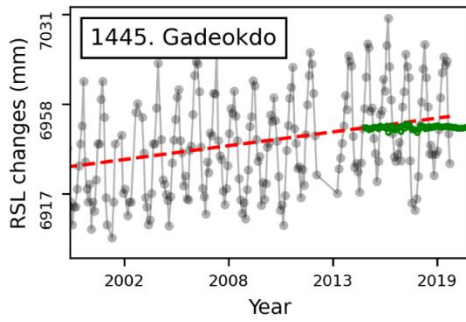
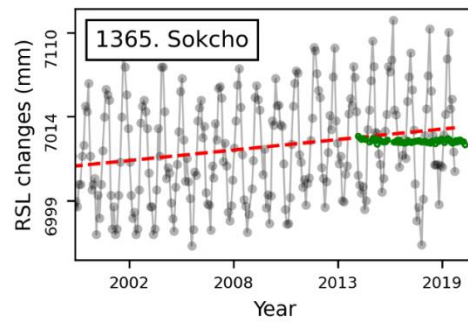
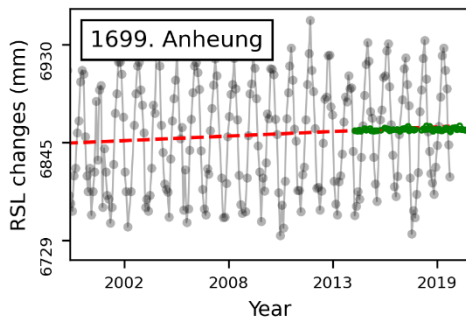
Japan



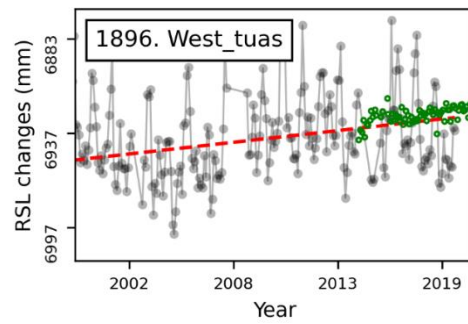
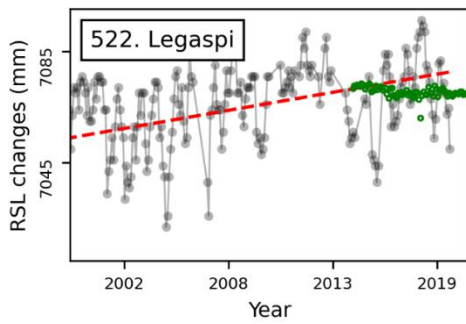


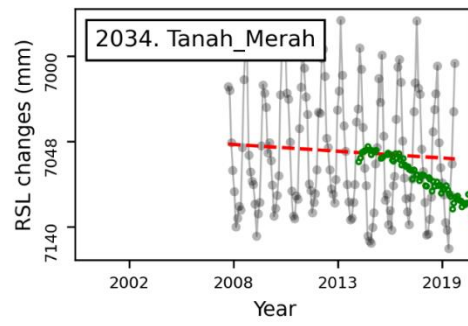
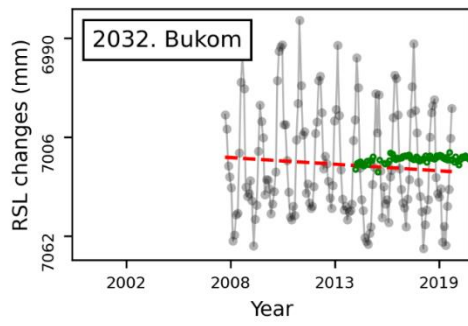
Korea





South Asia





Appendix – B

Table B1 InSAR VLM trend derived from Seq_InSAR for tide gauges from North America region

S.No	PSMSL ID	TG Name	Latitude	Longitude	InSAR VLM (mm/year)
1	10	San_Francisco	37.806339	-122.46602	-2.15
2	12	New_York	40.700625	-74.014316	nan
3	96	Halifax	44.666667	-63.583333	-0.2
4	127	Seattle	47.601666	-122.33833	3.4
5	158	San_Diego	32.717	-117.167	0.09
6	161	Galveston	29.31	-94.793	nan
7	166	Victoria	48.424167	-123.37083	-0.16
8	180	Atlantic_city	39.356279	-74.418204	-0.69
9	235	Boston	42.353333	-71.053333	1.48
10	245	Los_Angeles	33.72094	-118.27229	nan
11	246	Pensacola	30.403786	-87.211414	1.4
12	265	Astoria	46.207374	-123.76841	0.2
13	299	Sewell Point	36.946667	-76.33	1.69
14	311	Annapolis	38.983333	-76.48	-2.12
15	377	Santa Monica	34.007429	-118.49958	-1.56
16	385	Neah_Bay	48.367363	-124.61394	-0.91
17	399	Portsmouth	36.822	-76.293	1.15

18	497	Port Isabel	26.06	-97.215	-0.68
19	520	St.Petersburg	27.760597	-82.626848	0.66
20	526	Grand_isle	29.264916	-89.957593	nan
21	725	Freeport	28.948333	-95.308333	1.19
22	1106	Fort_Myers1	26.647	-81.87	1.8
23	1269	Charleston_II	43.344879	-124.32293	1.28
24	2297	USCG Freeport	28.9433333	-95.301667	2.6
25	1067	Anchorage	61.238333	-149.89	-0.18
26	2127	Port Angeles	48.125	-123.44	0.85
27	2328	New_canal	30.026667	-90.113333	nan
28	832	Palermo	-34.56667	-58.4	-3.12
29	256	La_jolla	32.866667	-117.25667	2.75
30	300	Hilo	19.730073	-155.05542	0.53
31	155	Honolulu	21.306667	-157.86667	-1.28

Table B2 InSAR VLM trend derived from Seq_InSAR for tide gauges from Europe region

S.No	PSMSL ID	TG Name	Latitude	Longitude	InSAR VLM (mm/year)
1	1	Brest	48.38285	-4.49484	-0.07
2	22	Rotterdam	51.9775	4.119	-1.1
3	41	Poti	42.16667	41.68333	-4.02

4	47	Stavanger	58.97088	5.730719	-2.74
5	82	Kobenhavn	55.68333	12.6	-0.83
6	154	Trieste	45.64736	13.7588	0.26
7	960	Alicante	38.33892	-0.48123	0.16
8	1239	Levkas	38.83457	20.71221	1.87
9	1811	Barcelona	41.34177	2.165676	-0.66
10	1832	Newport	51.55	-2.98744	-0.83
11	760	Dubrovnik	42.65708	18.06068	0.56
12	453	Le_harve	49.4819	0.106	0.27
13	168	Venezia	45.43108	12.33637	-0.41
14	78	Stockholm	59.32417	18.08167	0.1

Table B3 InSAR VLM trend derived from Seq_InSAR for tide gauges from East Asia region

S.No	PSMSL ID	TG Name	Latitude	Longitude	InSAR VLM (mm/year)
1	134	Kushimoto	33.4759	135.773	-1.28
2	635	Onahama	36.938	140.892	0.91
3	721	asamushi	40.8975	1.41E+02	0.48
4	722	Yokosuko	35.288	139.6514	nan
5	808	Shimizu- Minato	35.01167	138.5175	-0.62
6	813	Hakodate_I	41.7817	140.725	2.64

7	954	Mokpo	34.77972	126.3756	-0.52
8	955	Busan	35.09611	129.0356	-0.23
9	956	Incheon	37.45194	126.5922	1.53
10	997	Ulsan	35.50194	129.3872	0.36
11	1026	Onizaki	34.904	136.824	-3.61
12	1066	Jeju	33.5275	126.5431	-2.31
13	1148	Tajiri	35.5937	134.316	0.53
14	1155	Yeosu	34.74722	127.7656	0.45
15	1210	Tokuyama II	34.04083	131.8028	-2.11
16	1263	Omaezaki	34.60833	138.2222	3.14
17	1324	Pohang	36.04722	129.3839	-26.02
18	1345	Soma	37.8308	140.962	1.01
19	1346	Kamaisi	39.27333	141.8892	nan
20	1364	Ofunato	39.0198	141.753	3.90
21	1365	Sokcho	38.20722	128.5942	-0.55
22	1387	Maizuru II	35.47667	135.3869	-0.20
23	1438	Yaizu	34.8707	138.327	0.52
24	1446	Tongyeong	34.8275	128.4347	-1.31
25	1527	Gunsan	35.97556	126.5633	1.94
26	1544	Choshi	35.74444	140.8583	1.88
27	1585	Hamada	34.8973	132.066	-2.22
28	1699	Anheung	36.67361	126.1322	0.51

29	2258	Taeon	36.91306	126.2389	nan
30	1094	Hakata	33.61889	130.4078	-4.23
31	1100	Nagasaki	32.73512	129.8661	-1.54
32	1389	Toyama	36.762199	137.225	nan
33	1488	Nagoya	35.09139	136.8808	nan
34	1675	Boryeong	36.40639	126.4861	2.46
35	1627	Seogwipo	33.24	126.5617	-2.0
36	1568	Wando	34.31575	126.7594	-0.68
37	1445	Gadeokdo	35.02472	128.8108	nan

Table B4 InSAR VLM trend derived from Seq_InSAR for tide gauges from Australia region

S.No	PSMSL ID	TG Name	Latitude	Longitude	InSAR VLM (mm/yr)
1	111	Fremantle	-32.0558	115.7394	1.29
2	221	Wellington	-41.285	174.7794	0.9
3	247	Port Lyttelton	-43.6058	172.7222	4.4
4	474	Dieppe	49.92918	1.08444	-0.32
5	935	Darwin	-12.4718	130.8459	1.88
6	1750	Napier	-39.4757	176.9201	nan
7	1761	Hillarys	-31.8255	115.7386	0.84
8	2356	Suva-B	-18.1325	178.4275	-0.9

Bibliography

- Kawashima K, Aizawa K, Takahashi K (1984) Attenuation of peak ground motion and absolute acceleration response spectra. In: Proceedings of the 8th world conference on earthquake engineering. San Francisco, California, USA, 21–28 July, 1984, vol 2, pp 257–264.
- Ablain, M., A. Cazenave, G. Valladeau, and S. Guinehut. 2009. "A new assessment of the error budget of global mean sea level rate estimated by satellite altimetry over 1993–2008." *Ocean Sci.* 5 (2):193-201. doi: 10.5194/os-5-193-2009.
- Adebisi, Naheem, Abdul-Lateef Balogun, Teh Hee Min, and Abdulwaheed Tella. 2021. "Advances in estimating Sea Level Rise: A review of tide gauge, satellite altimetry and spatial data science approaches." *Ocean & Coastal Management* 208:105632. doi: <https://doi.org/10.1016/j.ocecoaman.2021.105632>.
- Agram, P. S., R. Jolivet, B. Riel, Y. N. Lin, M. Simons, E. Hetland, M. P. Doin, and C. Lasserre. 2013. "New Radar Interferometric Time Series Analysis Toolbox Released." *Eos, Transactions American Geophysical Union* 94 (7):69-70. doi: 10.1002/2013EO070001.
- Amelung, Falk, Devin L. Galloway, John W. Bell, Howard A. Zebker, and Randell J. Laczniaik. 1999. "Sensing the ups and downs of Las Vegas: InSAR reveals structural control of land subsidence and aquifer-system deformation." *Geology* 27 (6):483-486. doi: 10.1130/0091-7613(1999)027<0483:stuado>2.3.co;2.
- Amelung, Falk, Clive Oppenheimer, P. Segall, and H. Zebker. 2000. "Ground deformation near Gada ‘Ale Volcano, Afar, observed by radar interferometry." *Geophysical Research Letters* 27 (19):3093-3096. doi: <https://doi.org/10.1029/2000GL008497>.
- Bamler, Richard, and Philipp Hartl. 1998. "Synthetic aperture radar interferometry." *Inverse Problems* 14 (4):R1-R54. doi: 10.1088/0266-5611/14/4/001.
- Beckley, B. D., P. S. Callahan, D. W. Hancock III, G. T. Mitchum, and R. D. Ray. 2017. "On the ‘Cal-Mode’ Correction to TOPEX Satellite Altimetry and Its Effect on the Global Mean Sea Level Time Series." *Journal of Geophysical Research: Oceans* 122 (11):8371-8384. doi: <https://doi.org/10.1002/2017JC013090>.

- Berardino, P., G. Fornaro, R. Lanari, and E. Sansosti. 2002. "A new algorithm for surface deformation monitoring based on small baseline differential SAR interferograms." *Ieee Transactions on Geoscience and Remote Sensing* 40 (11):2375-2383. doi: 10.1109/Tgrs.2002.803792.
- Blackwell, Em, Manoochehr Shirzaei, Chandrakanta Ojha, and Susanna Werth. 2020. "Tracking California's sinking coast from space: Implications for relative sea-level rise." *Science Advances* 6 (31):eaba4551. doi: 10.1126/sciadv.aba4551.
- Blewitt, Geoff, Zuheir Altamimi, James Davis, Richard Gross, Chung-Yen Kuo, Frank G. Lemoine, Angelyn W. Moore, Ruth E. Neilan, Hans-Peter Plag, Markus Rothacher, C. K. Shum, Michael G. Sideris, Tilo Schöne, Paul Tregoning, and Susanna Zerbini. 2010. "Geodetic Observations and Global Reference Frame Contributions to Understanding Sea-Level Rise and Variability." 256-284. doi: 10.1002/9781444323276.ch9.
- Bouin, M. N., and G. Wöppelmann. 2010. "Land motion estimates from GPS at tide gauges: a geophysical evaluation." *Geophysical Journal International* 180 (1):193-209. doi: 10.1111/j.1365-246X.2009.04411.x.
- Bürgmann, Roland, Paul A. Rosen, and Eric J. Fielding. 2000. "Synthetic Aperture Radar Interferometry to Measure Earth's Surface Topography and Its Deformation." *Annual Review of Earth and Planetary Sciences* 28 (1):169-209. doi: 10.1146/annurev.earth.28.1.169.
- Cazenave, A., K. Dominh, F. Ponchaut, L. Soudarin, J. F. Cretaux, and C. Le Provost. 1999. "Sea level changes from Topex-Poseidon altimetry and tide gauges, and vertical crustal motions from DORIS." *Geophysical Research Letters* 26 (14):2077-2080. doi: 10.1029/1999gl900472.
- Cazenave, Anny, Hindumathi Palanisamy, and Michael Ablain. 2018. "Contemporary sea level changes from satellite altimetry: What have we learned? What are the new challenges?" *Advances in Space Research* 62 (7):1639-1653. doi: <https://doi.org/10.1016/j.asr.2018.07.017>.
- Chen, Curtis W., and Howard A. Zebker. 2001. "Two-dimensional phase unwrapping with use of statistical models for cost functions in nonlinear optimization."

- Journal of the Optical Society of America A* 18 (2):338-351. doi: 10.1364/JOSAA.18.000338.
- Church, John A, and Neil J White. 2006. "A 20th century acceleration in global sea-level rise." *Geophysical research letters* 33 (1).
- Church, John A., Peter U. Clark, Anny Cazenave, Jonathan M. Gregory, Svetlana Jevrejeva, Anders Levermann, Mark A. Merrifield, Glenn A. Milne, R. Steven Nerem, Patrick D. Nunn, Antony J. Payne, W. Tad Pfeffer, Detlef Stammer, and Alakkat S. Unnikrishnan. 2013. "Sea-Level Rise by 2100." *Science* 342 (6165):1445-1445. doi: 10.1126/science.342.6165.1445-a.
- Church, John A., and Neil J. White. 2011. "Sea-Level Rise from the Late 19th to the Early 21st Century." *Surveys in Geophysics* 32 (4):585-602. doi: 10.1007/s10712-011-9119-1.
- Cipollini, Paolo, Francisco M. Calafat, Svetlana Jevrejeva, Angelique Melet, and Pierre Prandi. 2017. "Monitoring Sea Level in the Coastal Zone with Satellite Altimetry and Tide Gauges." *Surveys in Geophysics* 38 (1):33-57. doi: 10.1007/s10712-016-9392-0.
- Colesanti, C., A. Ferretti, F. Novali, C. Prati, and F. Rocca. 2003. "SAR monitoring of progressive and seasonal ground deformation using the permanent scatterers technique." *IEEE Transactions on Geoscience and Remote Sensing* 41 (7):1685-1701. doi: 10.1109/TGRS.2003.813278.
- Ding, Xiao-li, Zhi-wei Li, Jian-jun Zhu, Guang-cai Feng, and Jiang-ping Long. 2008. "Atmospheric Effects on InSAR Measurements and Their Mitigation." *Sensors* 8 (9):5426-5448.
- Douglas, Bruce C. 1997. "Global sea rise: a redetermination." *Surveys in Geophysics* 18 (2-3):279-292.
- Douglas, Bruce C. 2001. "Chapter 3 Sea level change in the era of the recording tide gauge." In *International Geophysics*, edited by Bruce C. Douglas, Michael S. Kearney and Stephen P. Leatherman, 37-64. Academic Press.
- Farr, Tom G, Paul A Rosen, Edward Caro, Robert Crippen, Riley Duren, Scott Hensley, Michael Kobrick, Mimi Paller, Ernesto Rodriguez, and Ladislav Roth. 2007. "The shuttle radar topography mission." *Reviews of geophysics* 45 (2).

- Fattahi, H., P. Agram, and M. Simons. 2017. "A Network-Based Enhanced Spectral Diversity Approach for TOPS Time-Series Analysis." *Ieee Transactions on Geoscience and Remote Sensing* 55 (2):777-786. doi: 10.1109/Tgrs.2016.2614925.
- Ferretti, A., A. Fumagalli, F. Novali, C. Prati, F. Rocca, and A. Rucci. 2011. "A New Algorithm for Processing Interferometric Data-Stacks: SqueeSAR." *IEEE Transactions on Geoscience and Remote Sensing* 49 (9):3460-3470. doi: 10.1109/TGRS.2011.2124465.
- Ferretti, A., C. Prati, and F. Rocca. 2001. "Permanent scatterers in SAR interferometry." *Ieee Transactions on Geoscience and Remote Sensing* 39 (1):8-20. doi: Doi 10.1109/36.898661.
- Fielding, E. J., R. G. Blom, and R. M. Goldstein. 1998. "Rapid subsidence over oil fields measured by SAR interferometry." *Geophysical Research Letters* 25 (17):3215-3218. doi: Doi 10.1029/98gl52260.
- Frederikse, Thomas, Felix Landerer, Lambert Caron, Surendra Adhikari, David Parkes, Vincent W. Humphrey, Sönke Dangendorf, Peter Hogarth, Laure Zanna, Lijing Cheng, and Yun-Hao Wu. 2020. "The causes of sea-level rise since 1900." *Nature* 584 (7821):393-397. doi: 10.1038/s41586-020-2591-3.
- Galloway, D. L., K. W. Hudnut, S. E. Ingebritsen, S. P. Phillips, G. Peltzer, F. Rogez, and P. A. Rosen. 1998. "Detection of aquifer system compaction and land subsidence using interferometric synthetic aperture radar, Antelope Valley, Mojave Desert, California." *Water Resources Research* 34 (10):2573-2585. doi: <https://doi.org/10.1029/98WR01285>.
- Gatelli, F., A. Monti Guamieri, F. Parizzi, P. Pasquali, C. Prati, and F. Rocca. 1994. "The wavenumber shift in SAR interferometry." *IEEE Transactions on Geoscience and Remote Sensing* 32 (4):855-865. doi: 10.1109/36.298013.
- Gehrels, W. Roland, and Philip L. Woodworth. 2013. "When did modern rates of sea-level rise start?" *Global and Planetary Change* 100:263-277. doi: <https://doi.org/10.1016/j.gloplacha.2012.10.020>.
- Hamlington, Benjamin D., Alex S. Gardner, Erik Ivins, Jan T. M. Lenaerts, J. T. Reager, David S. Trossman, Edward D. Zaron, Surendra Adhikari, Anthony Arendt,

- Andy Aschwanden, Brian D. Beckley, David P. S. Bekaert, Geoffrey Blewitt, Lambert Caron, Don P. Chambers, Hrishikesh A. Chandanpurkar, Knut Christianson, Beata Csatho, Richard I. Cullather, Robert M. DeConto, John T. Fasullo, Thomas Frederikse, Jeffrey T. Freymueller, Daniel M. Gilford, Manuela Girotto, William C. Hammond, Regine Hock, Nicholas Holschuh, Robert E. Kopp, Felix Landerer, Eric Larour, Dimitris Menemenlis, Mark Merrifield, Jerry X. Mitrovica, R. Steven Nerem, Isabel J. Nias, Veronica Nieves, Sophie Nowicki, Kishore Pangaluru, Christopher G. Piecuch, Richard D. Ray, David R. Rounce, Nicole-Jeanne Schlegel, Hélène Seroussi, Manoochehr Shirzaei, William V. Sweet, Isabella Velicogna, Nadya Vinogradova, Thomas Wahl, David N. Wiese, and Michael J. Willis. 2020. "Understanding of Contemporary Regional Sea-Level Change and the Implications for the Future." *Reviews of Geophysics* 58 (3):e2019RG000672. doi: <https://doi.org/10.1029/2019RG000672>.
- Hanssen, Ramon F. 2001. *Radar interferometry: data interpretation and error analysis*. Vol. 2: Springer Science & Business Media.
- Holgate, Simon J., Andrew Matthews, Philip L. Woodworth, Lesley J. Rickards, Mark E. Tamisiea, Elizabeth Bradshaw, Peter R. Foden, Kathleen M. Gordon, Svetlana Jevrejeva, and Jeff Pugh. 2012. *New Data Systems and Products at the Permanent Service for Mean Sea Level*. Vol. 29: BIOONE.
- Holgate, Simon J., Andrew Matthews, Philip L. Woodworth, Lesley J. Rickards, Mark E. Tamisiea, Elizabeth Bradshaw, Peter R. Foden, Kathleen M. Gordon, Svetlana Jevrejeva, and Jeff Pugh. 2013. "New Data Systems and Products at the Permanent Service for Mean Sea Level." *Journal of Coastal Research*:493-504. doi: 10.2112/jcoastres-d-12-00175.1.
- Hooper, A., P. Segall, and H. Zebker. 2007. "Persistent scatterer interferometric synthetic aperture radar for crustal deformation analysis, with application to Volcán Alcedo, Galápagos." *Journal of Geophysical Research: Solid Earth* 112 (B7). doi: [doi:10.1029/2006JB004763](https://doi.org/10.1029/2006JB004763).
- Hooper, Andrew. 2008. "A multi-temporal InSAR method incorporating both persistent scatterer and small baseline approaches." *Geophysical Research Letters* 35 (16). doi: [10.1029/2008gl034654](https://doi.org/10.1029/2008gl034654).

- Hooper, Andrew, David Bekaert, Karsten Spaans, and Mahmut Arıkan. 2012. "Recent advances in SAR interferometry time series analysis for measuring crustal deformation." *Tectonophysics* 514-517:1-13. doi: <https://doi.org/10.1016/j.tecto.2011.10.013>.
- Hooper, Andrew, and Howard A Zebker. 2007. "Phase unwrapping in three dimensions with application to InSAR time series." *JOSA A* 24 (9):2737-2747.
- Hooper, Andrew, Howard Zebker, Paul Segall, and Bert Kampes. 2004. "A new method for measuring deformation on volcanoes and other natural terrains using InSAR persistent scatterers." *Geophysical Research Letters* 31 (23). doi: [doi:10.1029/2004GL021737](https://doi.org/10.1029/2004GL021737).
- Hooper, Andrew. 2009. "A Statistical-Cost Approach to Unwrapping the Phase of InSAR Time Series."
- Jevrejeva, S., A. Grinsted, J. C. Moore, and S. Holgate. 2006. "Nonlinear trends and multiyear cycles in sea level records." *Journal of Geophysical Research: Oceans* 111 (C9). doi: [10.1029/2005jc003229](https://doi.org/10.1029/2005jc003229).
- Jiang, Liming, and Hui Lin. 2010. "Integrated analysis of SAR interferometric and geological data for investigating long-term reclamation settlement of Chek Lap Kok Airport, Hong Kong." *Engineering Geology* 110 (3):77-92. doi: <https://doi.org/10.1016/j.enggeo.2009.11.005>.
- Jung, S. 2008. "Spatial variability in long-term changes of climate and oceanographic conditions in Korea." *Journal of environmental biology* 29 4:519-29.
- Karegar, Makan A., Timothy H. Dixon, and Rocco Malservisi. 2015. "A three-dimensional surface velocity field for the Mississippi Delta: Implications for coastal restoration and flood potential." *Geology* 43 (6):519-522. doi: [10.1130/g36598.1](https://doi.org/10.1130/g36598.1).
- Karegar, Makan A., Timothy H. Dixon, Rocco Malservisi, Jürgen Kusche, and Simon E. Engelhart. 2017. "Nuisance Flooding and Relative Sea-Level Rise: the Importance of Present-Day Land Motion." *Scientific Reports* 7 (1):11197. doi: [10.1038/s41598-017-11544-y](https://doi.org/10.1038/s41598-017-11544-y).

- Kuo, C. Y., C. K. Shum, A. Braun, and J. X. Mitrovica. 2004. "Vertical crustal motion determined by satellite altimetry and tide gauge data in Fennoscandia." *Geophysical Research Letters* 31 (1). doi: doi:10.1029/2003GL019106.
- Kuo, Chung-Yen, CK Shum, Alexander Braun, Kai-Chien Cheng, and Yuchan Yi. 2008. "Vertical motion determined using satellite altimetry and tide gauges." *Terr. Atmos.*
- Massonnet, Didier, Pierre Briole, and Alain Arnaud. 1995. "Deflation of Mount Etna monitored by spaceborne radar interferometry." *Nature* 375 (6532):567-570. doi: 10.1038/375567a0.
- Massonnet, Didier, and Kurt L. Feigl. 1998. "Radar interferometry and its application to changes in the Earth's surface." *Reviews of Geophysics* 36 (4):441-500. doi: 10.1029/97rg03139.
- Massonnet, Didier, Marc Rossi, Cesar Carmona, Frederic Adragna, Gilles Peltzer, Kurt Feigl, and Thierry Rabaute. 1993. "The displacement field of the Landers earthquake mapped by radar interferometry." *Nature* 364 (6433):138-142.
- Milly, PCD, Anny Cazenave, James S Famiglietti, Vivien Gornitz, Katia Laval, Dennis P Lettenmaier, Dork L Sahagian, John M Wahr, and Clark R Wilson. 2010. "Terrestrial water-storage contributions to sea-level rise and variability." *Understanding Sea-Level Rise and Variability*:226-255.
- Nerem, R. S., B. D. Beckley, J. T. Fasullo, B. D. Hamlington, D. Masters, and G. T. Mitchum. 2018. "Climate-change-driven accelerated sea-level rise detected in the altimeter era." *Proceedings of the National Academy of Sciences* 115 (9):2022-2025. doi: 10.1073/pnas.1717312115.
- Ngo-Duc, T., K. Laval, J. Polcher, A. Lombard, and A. Cazenave. 2005. "Effects of land water storage on global mean sea level over the past half century." *Geophysical Research Letters* 32 (9). doi: <https://doi.org/10.1029/2005GL022719>.
- Nicholls, Robert J., and Anny Cazenave. 2010. "Sea-Level Rise and Its Impact on Coastal Zones." *Science* 328 (5985):1517-1520. doi: 10.1126/science.1185782.
- Palanisamy Vadivel, Suresh Krishnan, Duk-jin Kim, Jungkyo Jung, Yang-Ki Cho, Ki-Jong Han, and Kwang-Young Jeong. 2019. "Sinking Tide Gauge Revealed by

- Space-borne InSAR: Implications for Sea Level Acceleration at Pohang, South Korea." *Remote Sensing* 11 (3):277.
- Palanisamy Vadivel, Suresh Krishnan, Duk-jin Kim, Jungkyo Jung, Yang-Ki Cho, and Ki-Jong Han. 2021. "Monitoring the Vertical Land Motion of Tide Gauges and Its Impact on Relative Sea Level Changes in Korean Peninsula Using Sequential SBAS-InSAR Time-Series Analysis." *Remote Sensing* 13 (1):18.
- Park, Jeong-Soo, Hyun-Suk Kang, Young Saeng Lee, and Maeng-Ki Kim. 2011. "Changes in the extreme daily rainfall in South Korea." *International Journal of Climatology* 31 (15):2290-2299. doi: doi:10.1002/joc.2236.
- Peltier, W. R., and A. M. Tushingham. 1991. "Influence of glacial isostatic adjustment on tide gauge measurements of secular sea level change." *Journal of Geophysical Research: Solid Earth* 96 (B4):6779-6796. doi: doi:10.1029/90JB02067.
- Peltier, WR. 2004. "Global glacial isostasy and the surface of the ice-age Earth: the ICE-5G (VM2) model and GRACE." *Annu. Rev. Earth Planet. Sci.* 32:111-149.
- Poitevin, Cyril, Guy Wöppelmann, Daniel Raucoules, Gonéri Le Cozannet, Marta Marcos, and Laurent Testut. 2019. "Vertical land motion and relative sea level changes along the coastline of Brest (France) from combined space-borne geodetic methods." *Remote Sensing of Environment* 222:275-285. doi: <https://doi.org/10.1016/j.rse.2018.12.035>.
- Pörtner, Hans-Otto, Debra C Roberts, Valérie Masson-Delmotte, Panmao Zhai, Melinda Tignor, Elvira Poloczanska, Katja Mintenbeck, M Nicolai, A Okem, and J Petzold. 2019. "IPCC special report on the ocean and cryosphere in a changing climate." *IPCC Intergovernmental Panel on Climate Change (IPCC)*.
- Raucoules, Daniel, Gonéri Le Cozannet, Guy Wöppelmann, Marcello de Michele, Médéric Gravelle, Arturo Daag, and Marta Marcos. 2013. "High nonlinear urban ground motion in Manila (Philippines) from 1993 to 2010 observed by DInSAR: Implications for sea-level measurement." *Remote Sensing of Environment* 139:386-397. doi: <https://doi.org/10.1016/j.rse.2013.08.021>.

- Ray, Richard D., and Bruce C. Douglas. 2011. "Experiments in reconstructing twentieth-century sea levels." *Progress in Oceanography* 91 (4):496-515. doi: <https://doi.org/10.1016/j.pocean.2011.07.021>.
- Reager, J. T., A. S. Gardner, J. S. Famiglietti, D. N. Wiese, A. Eicker, and M.-H. Lo. 2016. "A decade of sea level rise slowed by climate-driven hydrology." *Science* 351 (6274):699-703. doi: 10.1126/science.aad8386.
- Roemmich, Dean, and John Gilson. 2009. "The 2004–2008 mean and annual cycle of temperature, salinity, and steric height in the global ocean from the Argo Program." *Progress in Oceanography* 82 (2):81-100. doi: <https://doi.org/10.1016/j.pocean.2009.03.004>.
- Rosen, P. A., E. Gurrola, G. F. Sacco, and H. Zebker. 2012. "The InSAR scientific computing environment." EUSAR 2012; 9th European Conference on Synthetic Aperture Radar, 23-26 April 2012.
- Samieie-Esfahany, Sami, R. Hanssen, Karin van Thienen-Visser, and Annemarie Muntendam-Bos. 2009. "On the effect of horizontal deformation on InSAR subsidence estimates." Proceedings of the Fringe 2009 Workshop, Frascati, Italy.
- Santamaría Gómez, Álvaro. 2010. "Estimation des mouvements verticaux de l'écorce terrestre par GPS dans un repère géocentrique dans le cadre du projet TIGA." Observatoire de Paris.
- Santamaría-Gómez, A., M. Gravelle, X. Collilieux, M. Guichard, B. Martín Míguez, P. Tiphaneau, and G. Wöppelmann. 2012. "Mitigating the effects of vertical land motion in tide gauge records using a state-of-the-art GPS velocity field." *Global and Planetary Change* 98-99:6-17. doi: <https://doi.org/10.1016/j.gloplacha.2012.07.007>.
- Santamaría-Gómez, Alvaro, Médéric Gravelle, and Guy Wöppelmann. 2014. "Long-term vertical land motion from double-differenced tide gauge and satellite altimetry data." *Journal of Geodesy* 88 (3):207-222.
- Schumacher, M., M. A. King, J. Rougier, Z. Sha, S. A. Khan, and J. L. Bamber. 2018. "A new global GPS data set for testing and improving modelled GIA uplift rates." *Geophysical Journal International* 214 (3):2164-2176. doi: 10.1093/gji/ggy235.

- Takahashi, Hidenori, Shinji Sassa, Yoshiyuki Morikawa, Daiki Takano, and Kenji Maruyama. 2014. "Stability of caisson-type breakwater foundation under tsunami-induced seepage." *Soils and Foundations* 54 (4):789-805. doi: <https://doi.org/10.1016/j.sandf.2014.07.002>.
- Watkins, Michael M., David N. Wiese, Dah-Ning Yuan, Carmen Boening, and Felix W. Landerer. 2015. "Improved methods for observing Earth's time variable mass distribution with GRACE using spherical cap mascons." *Journal of Geophysical Research: Solid Earth* 120 (4):2648-2671. doi: <https://doi.org/10.1002/2014JB011547>.
- Watson, Phil J. 2019. "Updated Mean Sea-Level Analysis: South Korea." *Journal of Coastal Research* 35 (2):241-250, 10.
- Widlansky, Matthew J., Xiaoyu Long, and Fabian Schloesser. 2020. "Increase in sea level variability with ocean warming associated with the nonlinear thermal expansion of seawater." *Communications Earth & Environment* 1 (1):9. doi: 10.1038/s43247-020-0008-8.
- Wöppelmann, G., and M. Marcos. 2012. "Coastal sea level rise in southern Europe and the nonclimate contribution of vertical land motion." *Journal of Geophysical Research: Oceans* 117 (C1). doi: doi:10.1029/2011JC007469.
- Wöppelmann, G., B. Martin Miguez, M. N. Bouin, and Z. Altamimi. 2007. "Geocentric sea-level trend estimates from GPS analyses at relevant tide gauges world-wide." *Global and Planetary Change* 57 (3):396-406. doi: <https://doi.org/10.1016/j.gloplacha.2007.02.002>.
- Wöppelmann, Guy, and Marta Marcos. 2016. "Vertical land motion as a key to understanding sea level change and variability." *Reviews of Geophysics* 54 (1):64-92. doi: doi:10.1002/2015RG000502.
- Wouters, Bert, Alex S. Gardner, and Geir Moholdt. 2019. "Global Glacier Mass Loss During the GRACE Satellite Mission (2002-2016)." *Frontiers in Earth Science* 7:96.
- Wright, Tim J., Barry E. Parsons, and Zhong Lu. 2004. "Toward mapping surface deformation in three dimensions using InSAR." *Geophysical Research Letters* 31 (1). doi: <https://doi.org/10.1029/2003GL018827>.

- Yen, Jiun-Yee, Kun-Shan Chen, Chung-Pai Chang, and Sin Mei Ng. 2006. "Deformation and „deformation quiescence” prior to the Chi-Chi earthquake evidenced by DInSAR and groundwater records during 1995–2002 in Central Taiwan." *Earth, planets and space* 58 (7):805-813.
- Zebker, H. A., and J. Villasenor. 1992. "Decorrelation in interferometric radar echoes." *IEEE Transactions on Geoscience and Remote Sensing* 30 (5):950-959. doi: 10.1109/36.175330.